



AD-A121637

ATTAINMENT AND MIXING IN THRUST  
AUGMENTING EJECTORS

Interim Report

L. Bernal  
V. Sarohia

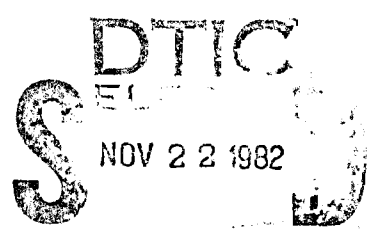
February 26, 1982

Prepared for

Air Force Flight Dynamics Laboratories,  
Air Force Office of Scientific Research,  
NASA Ames Research Center, and  
Naval Air Development Center

by

Jet Propulsion Laboratory  
California Institute of Technology  
Pasadena, California 91101



A

public release;  
unlimited.

82 11 22 030

11/22/82

UNCLASSIFIED

SECURITY CLASSIFICATION OF THIS PAGE (When Data Entered)

REPORT DOCUMENTATION PAGE		READ INSTRUCTIONS BEFORE COMPLETING FORM
1. REPORT NUMBER <b>AFOSR-TR- 82 - 1008</b>	2. GOVT ACCESSION NO. <b>AD-A121637</b>	3. RECIPIENT'S CATALOG NUMBER
4. TITLE (and Subtitle) ENTRAINMENT AND MIXING IN THRUST AUGMENTING EJECTORS		5. TYPE OF REPORT & PERIOD COVERED TECHNICAL
		6. PERFORMING ORG. REPORT NUMBER
7. AUTHOR(s) L BERNAL V SAROHIA		8. CONTRACT OR GRANT NUMBER(s) AFOSR-ISSA-81-00029
9. PERFORMING ORGANIZATION NAME AND ADDRESS JET PROPULSION LABORATORY CALIFORNIA INSTITUTE OF TECHNOLOGY 4800 OAK GROVE DRIVE PASADENA, CA 91109		10. PROGRAM ELEMENT, PROJECT, TASK AREA & WORK UNIT NUMBERS 61102F 2307/A1
11. CONTROLLING OFFICE NAME AND ADDRESS AIR FORCE OFFICE OF SCIENTIFIC RESEARCH/NA BOLLING AFB, DC 20332		12. REPORT DATE
		13. NUMBER OF PAGES 89
14. MONITORING AGENCY NAME & ADDRESS (if different from Controlling Office)		15. SECURITY CLASS. (of this report) UNCLASSIFIED
		15a. DECLASSIFICATION DOWNGRADING SCHEDULE
16. DISTRIBUTION STATEMENT (of this Report)  Approved for Public Release; Distribution Unlimited.		
17. DISTRIBUTION STATEMENT (of the abstract entered in Block 20, if different from Report)		
18. SUPPLEMENTARY NOTES		
19. KEY WORDS (Continue on reverse side if necessary and identify by block number) THRUST AUGMENTATION EJECTORS TURBULENT FLOW LASER DOPPLER VELOCIMETERS		
20. ABSTRACT (Continue on reverse side if necessary and identify by block number) Experiments have been performed with subsonic and underexpanded choked two-dimensional primary nozzle ejector flow system without diffusion to evaluate the role of entrainment and mixing in thrust augmentation. Two-component Laser Doppler velocity measurements (mean and fluctuating values), thrust measurements, ejector shroud surface pressure measurements and flow visualization were used to determine the evolution of the velocity profiles and their relationship to the ejector performance. The key findings of this research are: 1) Primary jet growth is significantly altered by the		

DD FORM 1473  
1 JAN 73

EDITION OF 1 NOV 65 IS OBSOLETE

UNCLASSIFIED

SECURITY CLASSIFICATION OF THIS PAGE (When Data Entered)

ejector shroud, 2) Primary jet turbulent characteristics when normalized with the local mean centerline velocity are in agreement with those for the free-jet. 3) In the neighborhood of the ejector shroud, the flow field can be classified into two regions, the potential flow region and the region close to the ejector exit which is dominated by the turbulent transport. 4) The pressure recovery is very sharp in the first region and is more gradual in the region close to the ejector exit. The investigation is continuing toward near-term objectives of obtaining measurements within diffused flow and with heated primary air.

UNCLASSIFIED

JPL-Publication D-66

AIR FORCE OFFICE OF SCIENTIFIC RESEARCH (AFSC)  
NOTICE OF TRANSMITTAL TO DTIC  
This technical report is approved and is  
approved for distribution under AFAR 190-12.  
Distribution is unlimited.  
MATTHEW J. MEYER  
Chief, Technical Information Division

ENTRAINMENT AND MIXING IN THRUST

AUGMENTING EJECTORS

Interim Report

L. Bernal

V. Sarohia

February 26, 1982

Prepared for

Air Force Flight Dynamics Laboratories,  
Air Force Office of Scientific Research,  
NASA Ames Research Center, and  
Naval Air Development Center

by

Jet Propulsion Laboratory  
California Institute of Technology  
Pasadena, California 91101

Approved For	/
NTIS	
DTIC	
UNCLASSIFIED	
DATE	
BY	
FILE	
SEARCHED	
SERIALIZED	
INDEXED	
FILED	
A	



## CONTENTS

<u>TITLE</u>	<u>PAGE</u>
Abstract -----	i
Contents -----	ii
List of Tables -----	iv
List of Figures -----	v
Nomenclature -----	viii
I. Introduction -----	1
II. Flow Facility and Instrumentation -----	5
2.1 Ejector Facility -----	5
2.1.1 Primary Nozzle -----	6
2.1.2 Ejector Shroud -----	7
2.2 Laser Doppler Velocimeter -----	8
2.2.1 Optical System -----	9
2.2.2 Particle Generator and Injector -----	11
2.2.3 Signal Processor and Data Acquisition -----	12
2.2.4 Operating Procedures -----	14
2.2.5 Data Processing -----	15
2.3 Other Instrumentation -----	19
III. Experimental Results -----	21
3.1 Primary Jet Characterization -----	21
3.2 Constant Area Ejector -----	23
3.2.1 Flow Visualization -----	24
3.2.2 Thrust and Surface Pressure Measurements -----	24
3.2.3 Mean Velocity Results -----	26
3.2.4 Turbulence Measurements -----	31

CONTENTS (Cont.)

<u>TITLE</u>	<u>PAGE</u>
IV. Discussion -----	34
V. Conclusions -----	37
VI. Acknowledgements -----	38
References -----	39
Tables -----	41
Figures -----	44

LIST OF TABLES

	<u>PAGE</u>
1. Dimensions of the flow facility. -----	41
2. Characteristics of the Laser Doppler Velocimeter focal volume. -----	42
3. Comparison of surface pressure measurements with thrust measurements. -----	43
4. Center-line velocity angle in the optical frame of reference. -----	43

## LIST OF FIGURES

	<u>PAGE</u>
1. Ejector facility. -----	44
2. Diagram hardware components of ejector facility. -----	45
3. Primary nozzle components. -----	46
4. Primary nozzle elements position. Dimensions in cm. -----	47
5. Ejector shroud geometry showing the location of surface pressure tabs. Dimensions in cm. -----	48
6. Primary and secondary flow injectors location. Dimensions in cm. -----	49
7. Laser Doppler Velocimeter. -----	50
8. LDV location in relation to the test section. -----	51
9. Transmitting optics components. -----	52
10. Collecting optics components. -----	53
11. Focal volume formation schematic. -----	54
12. Spray bar geometry. Dimensions in cm. -----	55
13. Typical frequency histograms. -----	56
14. Velocity transformation between the optical and physical frames of reference. -----	57
15. Thrust balance schematic. Dimensions in cm. -----	58
16. Ejector coordinate system and locations at which velocity profiles were obtained. -----	59
17. Shadowgraph picture free-jet. $M_{ex} = 0.5$ . -----	60
18. Normalized jet width as a function of downstream distance. -----	61
19. Center-line velocity decay with downstream distance. -----	62
20. Center-line velocity decay comparison with collected data on reference 21. $\Delta$ present results, (-) reference 21. -----	63
21. Shadowgraph picture of ejector flow. $M_{ex} = 0.5$ . -----	64
22. Ejector thrust augmentation ratio, $T_e/T_0$ , as a function of primary jet pressure ratio. -----	65

LIST OF FIGURES (Cont.)

	<u>PAGE</u>
23. Ejector shroud surface pressure coefficient at $M_{ex} = 0.3$ and $0.5$ . $x_1 = 12.7$ cm (see Figure 16). -----	66
24. Ejector shroud surface pressure coefficient at $M_{ex} = 0.75$ and $1.0$ (critical conditions). $x_1 = 12.7$ cm (see Figure 16). -----	67
25. Ejector shroud surface pressure coefficient at $p_0/p_S = 2.0$ and $2.9$ (under expanded primary jet). $x_1 = 12.7$ cm (see Figure 16). -----	68
26. Mean $\bar{u}$ velocity profiles inside the ejector shroud at $M_{ex} = 0.3$ . -----	69
27. Mean $\bar{u}$ velocity profiles inside the ejector shroud at $M_{ex} = 0.5$ . -----	70
28. Mean $\bar{u}$ velocity profiles inside the ejector shroud at $M_{ex} = 0.75$ . -----	71
29. Mean $\bar{u}$ velocity profiles inside the ejector shroud at $M_{ex} = 1.0$ (critical conditions). -----	72
30. Mean $\bar{u}$ velocity profiles entrance region at $M_{ex} = 0.5$ . -----	73
31. Mean $\bar{u}$ velocity profiles inside the ejector shroud at $M_{ex} = 0.5$ . Single component LDV configuration. -----	74
32. Ejector centerline velocity decay. -----	75
33. Downstream variation of the velocity at $y = 4.0$ cm. <u>Open</u> symbols measured velocity. Closed symbols $\bar{u} = U_j \sqrt{-C_p}$ . $x_1 = 12.7$ cm (see Figure 16). -----	76
34. Mean $\bar{v}$ velocity profiles inside the ejector shroud at $M_{ex} = 0.3$ . -----	77
35. Mean $\bar{v}$ velocity profiles inside the ejector shroud at $M_{ex} = 0.5$ . -----	78
36. Mean $\bar{v}$ velocity profiles inside the ejector shroud at $M_{ex} = 0.75$ . -----	79
37. Mean $\bar{v}$ velocity profiles inside the ejector shroud at $M_{ex} = 1.0$ (critical conditions). -----	80
38. Mean $\bar{v}$ velocity profiles entrance region at $M_{ex} = 0.5$ . -----	81
39. Downstream variation of mass flow ratios. $x_1 = 12.7$ cm (see Figure 16). -----	82

LIST OF FIGURES (Cont.)

	<u>PAGE</u>
40. Momentum balance calculation. $x_1 = 12.7$ cm (see Figure 16). (a) Downstream evolution of the momentum flux. (b) Momentum conservation within the ejector shroud. -----	83
41. Mean kinetic energy flux evolution within the ejector shroud. $x_1 = 12.7$ cm (see Figure 16). -----	84
42. Normalized turbulent intensity profiles inside the ejector shroud, $u'$ component. -----	85
43. Normalized turbulent intensity profiles inside the ejector shroud. Single component LDV configuration. -----	86
44. Normalized turbulent intensity profiles inside the ejector shroud, $v'$ component. -----	87
45. Normalized $\overline{u'v'}$ velocity correlation inside the ejector shroud. -----	88
46. Downstream evolution of the turbulent kinetic energy (two components). $x_1 = 12.7$ cm (see Figure 16). -----	89

## NOMENCLATURE

A	Primary jet area
a	Speed of sound
$C_p$	$= \frac{p-p_s}{(1/2\rho u^2)_{ex}}$ . Surface pressure coefficient
$C_s$	Particle settling velocity
$D_e^{-2}$	Laser beam diameter
d	Focal volume diameter
$d_f$	Fringe spacing
f	Focal length
H	Ejector width
$H'$	System width
h	Primary jet width
$h_{eff}$	Primary jet effective width
K	$= 1/2(\bar{u}^2 + \bar{v}^2)$ . Mean kinetic energy, two components
k	$= 1/2(u'^2 + v'^2)$ . Turbulent kinetic energy, two components
L	Mixing chamber length
$L'$	Diffuser length
$l$	Focal volume length
M	Momentum flux per unit span
$M_{ex}$	Primary jet exit Mach number
$\dot{m}$	Mass flow rate per unit span
$\dot{m}_j$	Ideal primary jet mass flow rate
N	Data buffer size
$N_{fr}$	Number of fringes in the focal volume
n	Summation index
P	$= (p-p_s)H$

NOMENCLATURE (cont.)

p	Static pressure
p <sub>s</sub>	Ambient pressure
R	Nose radius
Re	Reynolds number
r	= H/h. Ejector area ratio
S	Facility span
T <sub>e</sub>	Ejector thrust
T <sub>0</sub>	Primary nozzle thrust
ΔT <sub>C</sub>	$= 2RS \int_0^\pi (p_s - p) \sin \theta \, d\theta$
ΔT <sub>M</sub>	= T <sub>E</sub> - T <sub>0</sub>
(t <sub>n</sub> ) <sub>G</sub> , (t <sub>n</sub> ) <sub>B</sub>	Burst duration, blue or green component
U <sub>G</sub> , U <sub>B</sub>	Velocity component measured by the green or blue beams
U <sub>j</sub>	Primary jet exit velocity
U	$= \sqrt{U_G^2 + U_B^2}$ . Modulus velocity vector
u	Velocity component in the x direction
u <sub>c</sub> (x)	Centerline velocity
u'	r.m.s. value of the u velocity component fluctuation
v	Velocity component in the y direction
v'	r.m.s. value of the v velocity component fluctuation
$\overline{u'v'}$	Velocity correlation
W	$= \sum_{n=1}^N \omega_n$

## NOMENCLATURE (cont.)

$X$	Ejector shroud downstream location
$x, y$	Coordinates
$x_1$	= 12.7 cm. Mixing chamber downstream location
$x_c$	Primary jet core length
$x_0$	Virtual origin location
$\alpha$	Beams crossing angle
$\beta$	Diffuser half angle
$\gamma$	Specific heat ratio
$\delta$	Half velocity width free jet
$\delta_v$	Free jet visual thickness
$\theta$	Angular distance along the nose
$\kappa$	Doppler constant
$\Lambda$	Ejector aspect ratio
$\mu$	Air viscosity
$\phi$	Optical to physical frame of reference angle
$\rho$	Density
$\tau_s$	Particle lag time
$(\omega_n)_G, (\omega_n)_B, (\omega_n)_X$	Weighting factors
<b>Superscripts</b>	
$i$	Indicates different weighting factors
—	Mean value
<b>Subscripts</b>	
0	Stagnation conditions
ex	Primary jet exit conditions
s	Ambient static conditions

## I. INTRODUCTION

The jet thrust augmentation of an ejector system is governed by certain fluid mechanics phenomena associated with the entrainment of surrounding atmospheric air by the primary jet flow and subsequent mixing of this entrained fluid with the primary jet. Previous research has provided considerable insight into the operation of ejectors(1,2,3). These studies have shown that the ejector thrust augmentation results from the low pressure on the shroud entrance region caused by entrainment of secondary fluid. Pressure recovery is achieved by turbulent mixing between the primary jet and the secondary stream. The use of a diffuser further enhances thrust augmentation by reduction of the entrance pressure. Ultimately, these flow processes result in a pressure distribution on the shroud and primary nozzle surfaces. The integrated effect of the pressure forces over these surfaces gives a positive contribution to the system thrust. The fundamental processes that relate entrainment, mixing and diffusion with the pressure distribution on the ejector shroud and primary nozzle surfaces are as yet not adequately understood and are some of the main objectives of the present research.

Large scale testing and aircraft development programs which incorporate thrust augmenting ejectors have identified a number of problem areas which must be solved to achieve full implementation of the ejector concept in V/STOL applications(4,5). Among them, the requirement of high augmentation within the limited volume available in high performance aircraft results in insufficient mixing and in flow separation. Although ejector geometry is the primary design variable, from a fluid mechanical point of view it is valuable to relate these problems to the shroud surface pressure distribution and turbulent characteristics of the primary jet. Thus flow separation results from the inability of the boundary layer on the shroud surface to manage a large

adverse pressure gradient. It can be prevented using suitable boundary layer control devices(6). In order to determine the need of these devices and to optimize their design, more quantitative information is necessary on the flow processes near the shroud surfaces.

For a given geometrical configuration insufficient mixing results in flow non-uniformities at the exit plane of the ejector and consequently in performance losses. Since the velocity distribution at the entrance section of the ejector is not uniform, it is important to quantify the combined effects of pressure gradient and turbulent structure on the downstream evolution of the velocity distribution. Qualitatively, the effect of adverse pressure gradient tends to increase flow non-uniformities while the effect of turbulent mixing is to reduce them(1). Consistent with this qualitative argument is the increased performance found with hypermixing nozzles(6,7) and pulsatile primary jets(8).

An important aspect of thrust augmenting ejector operation is the influence on performance of primary flow total pressure and temperature. There is an extensive literature on the effects of pressure ratio across the primary nozzle on ejector performance at ambient total temperature(2). In contrast, there is scarce information on the effect of primary flow total temperature. This information is limited to overall system performance and ejector shroud surface pressure distribution. There is no information however on the effect of these parameters on the turbulent structure within the ejector.

A number of mathematical models have been used to investigate ejector flows. One-dimensional analysis is useful in evaluating performance trends associated with changes in the geometrical configuration(9,10) and thermodynamic parameters of the ejector system(11). The effect of the efficiency of individual elements on overall system performance has also been investi-

gated using one-dimensional analysis(6,11). Other models include phenomenological models(12-15) and finite difference models(16,17). The latter provide great flexibility in analyzing complex inlet geometries. The development of mixing is incorporated through a suitable turbulence model. In order to evaluate the accuracy of these models, detailed measurements of the ejector flow field including measurements of the turbulent quantities are needed(3).

An experimental research program was initiated by the JPL Experimental Fluid Dynamics Group to investigate the fluid dynamics of thrust augmenting ejectors. The objectives of this research are:

(A) To determine the role of entrained fluid and its mixing with the primary jet on the shroud surface pressure distribution and on ejector performance.

(B) To measure the evolution of the various profiles and determine the effect of the confining shroud surfaces on their evolution.

(C) To determine the effect of primary flow total pressure and temperature on the flow characteristics within the ejector and on its thrust performance.

(D) To provide basic data to support analytical research.

The emphasis in this investigation is on the basic fluid dynamics phenomena which influence the thrust augmentation performance of an ejector. The ejector configuration chosen consists of a primary two-dimensional jet discharging into a rectangular ejector shroud. Simple shroud geometries are being used in order to minimize instrumentation difficulties. They are a constant area ejector and a constant area mixing chamber followed by a diffuser. Measurements are being made of the system thrust, shroud surface pressure distribution, mean velocity field and turbulent stresses field.

The velocity measurements are being obtained using a two-component Laser Doppler Velocimeter. This technique is used because of the following reasons:

1) It has been used successfully to measure the velocity field in flows with large temperature gradients(18); 2) it does not require calibration; 3) the technique is non-intrusive and 4) it can measure the velocity in reverse flow regions if these regions are present. Hot Wire Anemometry, the only available alternative, has never been used successfully in non-uniform temperature flow fields. Probe calibration is required for velocity magnitude and direction; probe interference at the shroud can significantly influence the results of the measurements there and does not give direction discrimination in reverse flow regions. However, Laser Doppler Velocimetry requires the flow to be seeded with particles. Thus proper seeding devices must be built into the flow facility and the effect of particle concentration and size on measurement accuracy needs to be evaluated.

This interim report includes preliminary results obtained in a constant area ejector with ambient primary flow stagnation temperature and a maximum primary nozzle pressure ratio of 3.0. The effort to obtain measurements on the ejector with diffuser and heated primary flow is continuing. The report is organized as follows. In Section II the flow facility and instrumentation are described. A significant part of this section is devoted to the Laser Doppler Velocimeter. In it a detailed description of the system, data acquisition and data processing techniques is presented. The results of the measurements are described in Section III. They include measurements of the ejector configuration and free primary jet as well. When possible, the results of different measurements are compared against each other to verify their accuracy. Furthermore, the measured velocity has been used to evaluate mass, momentum and kinetic energy fluxes through the ejector in order to obtain additional insight into the performance characteristics of thrust augmenting ejectors. The results are discussed in Section IV and summarized in Section V.

## II. FLOW FACILITY AND INSTRUMENTATION

To acquire detailed and systematic ejector flow field measurements, the facility shown in figure 1 was designed and built. Some of the design goals of this facility included adequate control and reproducibility of the primary nozzle flow as well as flexibility to position the ejector shroud relative to the primary nozzle. Particular emphasis was given to the compatibility of the flow system with the Laser Doppler Velocimeter and the thrust balance. Therefore a system approach, in which the instrumentation played an important role as discussed below, was taken in the design of the facility.

### 2.1 Ejector Facility

A two-dimensional configuration was designed and tested in the ejector facility. The test apparatus consists of a two-dimensional jet discharging into the symmetrically located ejector shrouds. A maximum pressure ratio across the primary flow nozzle as high as  $P_0/P_S = 4.0$  can be obtained. The span of the primary jet is 50.8 cm and the width  $h$  is 0.762 cm, which gives an aspect ratio of 66.7. The maximum expected primary jet mass flow rate is 4.2 kg/sec, with the corresponding Reynolds number based on the jet width  $5.2 \times 10^6$ . There are no restrictions in the ejector shroud geometry other than those imposed by the primary jet dimensions, as discussed later in this section. The geometrical parameters of the final configuration used in the present research are summarized in Table 1.

The various hardware elements of the facility are shown in figure 2. The ejector system is mounted on a thrust balance with the span directed vertically upwards. This configuration was used for better spatial resolution of the Laser Doppler Velocimeter. The primary jet nozzle is attached to the balance with two horizontal plates limiting the flow in the spanwise direction. These plates are also used to support the ejector shroud.

Pressurized air at ambient temperature was provided by a compressor plant. The plant can deliver 4.5 kg/sec. of dry air at  $3 \times 10^6$  pascals, which exceeds the requirements of the ejector facility.

### 2.1.1 Primary Nozzle

In addition to the parameters specified earlier, namely a maximum operating pressure four times the ambient pressure and the exit area 0.762 cm x 50.8 cm, the primary flow nozzle was designed to allow direct thrust measurements. It also incorporates appropriate turbulence-reducing elements and seeding elements for Laser Doppler Velocimetry and flow visualization.

The various hardware components that form the primary nozzle are shown in figure 3. The nozzle consists of a stagnation section and a 20:1 contraction section. The stagnation section is rectangular in cross-section, 15 x 50.8 cm, with a total length of 37 cm. Pressurized air enters this section through two perforated tubes directed along the span, perpendicular to the system thrust as shown in figure 4. Four flexible tubes 5 cm in diameter are used to couple to the air supply so that not only a direct thrust measurement can be made but also any possible contribution of the inflow momentum to the measurement is avoided.

Several turbulence-reducing elements are used to minimize the primary jet turbulence level below 1 percent as indicated in figure 4. A 50 percent open area perforated plate with 3.2 mm diameter holes and 3.2 mm thick is located 7.6 cm downstream of the feed tubes. It is followed by a 80-mesh stainless steel screen 5 cm from the plate and a honeycomb element (1.6 cm cell size, 15 cm long) located 5 cm downstream of the screen. A second screen of identical dimensions is positioned 1 cm from the honeycomb.

The 20:1 contraction section follows immediately after the second screen. It has a straight section, 60° included angle, and a circular arc section as

indicated in figure 4. The contraction is two-dimensional, i.e. no area reduction in the span direction. Two pressure taps located on the center line at the entrance and exit area, respectively, were used to monitor the operating point of the system. In order to minimize any effects on the induced flow, the outer part of the nozzle was carefully machined at a 30° angle as shown in figure 4.

Two seeding locations are available in the primary flow system for Laser Doppler Anemometry and flow visualization. One is located upstream of the stagnation section in the air supply line; it was used primarily for flow visualization. The other, two spray bars of the type described in Section 2.2.2, is located 2.5 cm downstream of the first screen. The spray bars were used for the velocity measurements.

#### 2.1.2 Ejector Shroud

Important parameters of the ejector are the shroud area ratio  $r = H/h$  and the shroud aspect ratio  $\Lambda = S/H$  (see Table 1). The fixed primary jet geometry limits these parameters to values satisfying the equation

$$\frac{S}{h} = 66.67 = r\Lambda \quad (1)$$

where  $S$  is the span of the facility,  $h$  the primary jet width and  $H$  the ejector shroud spacing.

Experiments were conducted with an area ratio  $r = 16.7$ ,  $\Lambda = 4$ . The flow was found highly unsteady within the ejector with flow separation on at least one ejector shroud surface. For this reason a smaller value  $r = 13.3$ , with  $\Lambda=5$  was used in the measurements. A brief description of the flow field encountered in the larger area ratio ejector configuration will be presented in Section III.

A constant area ejector was tested first. The geometry is shown in

figure 5. The constant area length is 30.5 cm which normalized with the shroud spacing gives  $L/H = 3$ . A 5.1 cm diameter bell-mouth nose at the entrance of the mixing region was used to provide adequate flow characteristics of the secondary flow. In the final configuration tested, the ejector shroud was located 10.2 cm from the primary jet exit which gives a normalized value  $X/H = 1$ .

One ejector shroud surface was instrumented with surface pressure taps along the mid-span. The taps are spaced  $30^\circ$  apart along the nose and 1.3 cm in the straight section as shown in figure 5.

The ejector shroud surfaces were attached to the top and bottom walls with a clamping device that allows continuous adjustment of their position. This technique was found useful for alignment purposes. Alignment was achieved by positioning the ejector shroud parallel to the jet exit edge and the centerline defined by the jet maximum velocity.

Seeding of the secondary flow for the Laser Doppler Velocimeter was implemented with six spray bars described in 2.2.2. They were positioned along the span supported by the top and bottom walls at the locations indicated in figure 6. No attempt was made to remove the wake of the spray bars since any technique used will negatively affect the spray characteristics. This aspect will be discussed further in Section 2.2.2.

## 2.2 Laser Doppler Velocimeter

The velocity field in the ejector was measured with a two-component two-color Laser Doppler Velocimeter (LDV). The accuracy of the velocity measurements obtained with a LDV system is influenced by all its optical elements and by the particle size and distribution(19). Therefore an iterative process was needed to determine the optimum configuration for this application. A

picture of the system in its final configuration is shown in figure 7. It is a forward scatter configuration and the processor was operated in single-burst mode. Two atomizers were used to produce the particles needed for the measurements. The LDV processor operated with a minicomputer system which was also used for processing the results. A description of the various elements and data processing follows.

### 2.2.1 Optical System

A forward scatter configuration was used in these experiments with the transmitting and receiving optics located at either side of the facility as shown in figure 8. The transmitting optics components are presented schematically in figure 9. A two watt argon-ion laser is used as the light source. Past a collimating lens, a color separator provides two lines of the laser, the 514 nm green line and 488 nm blue line. Each beam is split into a pair of equal intensity beams by a polarization rotator and a beam splitter. The focal volume is formed by focussing the four parallel beams by a single 598 mm focal length lens. The collimator is used to minimize the lateral extent of the focal volume.

The receiving optics components are shown schematically in figure 10. The scattered light from the particles is collected by a 761 mm focal length lens. A dichroic mirror is used for color separation, with a focussing lens used to focus the scattered light of each of the two colors into a pin-hole (250  $\mu\text{m}$ ) and photomultiplier tube assembly.

The physical arrangement of the LDV optics relative to the facility is shown in figure 8. The transmitting and receiving optics are mounted on an optical table with their optical axes parallel to the flow direction. A first-surface flat mirror is used to rotate the beam 90°. Consequently the focal

volume has its longitudinal axis along the span of the facility. A second mirror is used to deflect the scattered light into the collecting optics.

The component of the velocity vector measured by the LDV and the Doppler constant, the conversion factor from frequency to velocity, is determined by the transmitting optics. The configuration used is shown in figure 11. The green beams pair enters the test section in a plane forming an angle of  $+45^\circ$  with the downstream direction, while the blue beams plane forms an angle of  $-45^\circ$ . Therefore, there is no need for frequency bias elements with the corresponding increase in the signal to noise ratio. The Doppler constant which is related to the fringe spacing within the focal volume is given by the equation

$$\kappa_D = \frac{\lambda}{2 \sin \frac{\alpha}{2}} \quad (2)$$

where  $\lambda$  is the light wavelength and  $\alpha$  the angle at which the beams cross in the focal volume. An angle  $\alpha = 4.72^\circ$  was used which gives Doppler constants for the green and blue components  $\kappa_{DG} = 6.24 \text{ (m/sec) (MHz)}^{-1}$  and  $\kappa_{DB} = 5.92 \text{ (m/sec) (MHz)}^{-1}$  respectively. The geometrical characteristics of the focal volume are summarized in Table 2.

The focal volume can be moved within the facility by means of remotely operated stepping motors. Motion on a fixed span plane was obtained by corresponding motion of the optical table. Motion along the span resulted from the displacement of the focussing lens and receiving optics along their optical axis. The table position was controlled with a resolution better than  $100 \mu\text{m}$ .

A minimum distance from the focal volume to the ejector shroud wall of 1 cm can be obtained with the two-component LDV configuration described above.

At shorter distances two beams are interrupted by the shroud as they enter the test section, thus preventing the formation of the focal volume. Measurements were made at shorter distances operating the LDV in a single component configuration. In this case the green beams were positioned on a plane parallel to the shroud wall, therefore only the downstream component of the velocity was measured. A minimum distance to the ejector wall of 0.25 cm can be obtained in this configuration.

### 2.2.2 Particle Generator and Injector

In order to measure the velocity with a Laser Doppler Velocimeter the air flow must be seeded with particles. The objective of the seeding device is to provide a spatially uniform concentration of particles, their size small enough to follow the flow while providing sufficient scattered light for an adequate signal to noise ratio. Propylene Glycol was used in these experiments, the particle diameter was  $2 \mu\text{m}$  which gives a terminal settling velocity  $C_s = 1.36 \times 10^{-2} \text{ cm/sec}$  (reference 20). The transient or lag time required for the particle to follow sharp changes in velocity is  $\tau_s = 14 \mu\text{sec}$ .

Both the primary and induced flows were seeded. Two particle generators were used. A commercial unit was used for the primary flow. It was found that the Propylene Glycol particles at the high concentration required at the exit of the generator increase in size presumably by collision among themselves. To prevent large particles from entering the primary flow, a size discriminator was included prior to and as close as possible to the primary flow spray bars.

A different system was used for the induced flow. A particle generator was designed and built. It incorporates the particle generator and the size discriminator in the same unit. The resulting aerosol is introduced into the induced flow by six spray bars as described earlier.

The spray bars of the primary and induced flows are similar in construction. They were made from 0.95 cm stainless steel tube with 0.64 cm diameter perforations spaced 2.54 cm apart as shown in figure 12. This configuration was obtained after testing of different diameter perforations. Small perforations resulted in excessive loss of particles by collisions with the wall. This design resulted in no loss of particles while providing uniform seeding across the span of the facility.

The resulting seeded flow was found to have adequate particle size and controllable concentration. However, no attempt was made to measure the particle concentration and size distribution directly. The particle concentration was adjusted using the data rate of the processors as reference.

### 2.2.3 Signal Processor and Data Acquisition

The measurement of the velocity can only be obtained after suitable processing of the photomultiplier tubes output as the scattering particles move across the focal volume. Two counter processors were used, one for each velocity component. They were operated in the single-burst mode, i.e. only one particle is present in the focal volume when the measurement is made. In addition, the system is operated in coincidence mode in which the output of the processors is tested for coincidence in time so that the two components of the velocity vector as determined by the optical setup are measured on the same particle. In the single component configuration used in measurements near the shroud, only one processor was needed.

The signal processing is accomplished in four stages: analog processing, burst processing, coincidence test and transfer to the computer. The analog processing involves suitable filtering and amplification of the signal for optimum signal to noise ratio. Both high pass and low pass filters are used.

The low pass filter is used primarily for pedestal removal and low frequency noise removal; low frequency noise is introduced by imperfections of the optical system. The cut-off values used varied from 300 kHz to 1 MHz depending on the flow velocity. The low pass filter is used for removal of high frequency noise. Cut-off values from 2 MHz to 100 MHz were used depending on flow velocity. The output of the filter is processed by an amplifier. In the present experiments however, the gain was set at unity, thus no amplification was needed for adequate operation of the system. Typical signal to noise ratio past the amplification stage was in excess of 100.

The burst processing encompasses the required electronics for the actual measurement of the particle velocity. A level detector determines the presence of a burst. Measurements are made of the total number of cycles in each burst, i.e. the number of fringes crossed by the particle, and its total time duration. The resolution of the time measurement is 1 nsec. Only bursts with more than 16 cycles are used for processing. The output of the burst processor is in digital form. It feeds into the computer interface that incorporates the coincidence test between the two processors. The coincidence test consists of the initiation of a time window after completion of processing by one of the processors. If data from the other processor is not received before the end of the window the data is discharged, otherwise coincidence is attained and the data from both processors is transferred to the computer. A time window of 17  $\mu$ sec was used in all the experiments.

A minicomputer was used to acquire and store the data. A computer program was developed for data acquisition using the LDV system. This computer program accomplishes two tasks. It generates a header which contains information relevant to the conditions of the experiment and LDV setup. It also acquires a buffer of 4016 words of data. This buffer size corresponds to

a total of 1004 velocity measurements in two-component measurements, since two words are generated for each component when a particle is found in the focal volume. The same program was used in single component measurements. In this case the buffer size corresponds to 2008 velocity measurements.

#### 2.2.4 Operating Procedures

Prior to every experimental run with the LDV system, a variety of tests was conducted to verify adequate operation of the system, e.g. the transmitting optics alignment and overlapping of the green and blue focal volumes. The fringes within the focal volume were also inspected to prevent distortions and intensity nonuniformities. The alignment of the receiving optics was verified with the facility in operation. Adjustment of the location of the pin-hole and photomultiplier assembly was often necessary for maximum data acquisition rate at the operating conditions of the atomizers.

After the high-pass and low-pass filters were set to their predetermined values, the gain of the amplifier stage was adjusted for optimum signal to noise ratio. If at this point the data rate was found below 100 or above 1000 particles/sec, the atomizers were adjusted to correct this condition. Coincidence between bursts occurring on the blue and green channels was also checked and the coincidence window varied if necessary.

After these tests were completed, actual measurements were initiated. The measurements reported here involved traverses across the flow at different downstream locations. The focal volume was moved in increments of 0.51 cm across the flow and 7.6 cm in the downstream direction, the measurements being made with the focal volume stationary. A 4016 word buffer was obtained at every point. The data was stored temporarily on disk. At the end of the test run, all the data was transferred to a magnetic tape for permanent storage and

processing at a later time. The size of the data buffer, 4016 words, combines with the data rate to give a total sample time between 1 and 10 sec. This sample time was considered adequate to properly characterize mean turbulent quantities.

#### 2.2.5 Data Processing

The velocity data generated by the data acquisition programs was processed using the minicomputer system. Processing involved several steps, e.g. error detection, computation of flow characteristics in the frame of reference of the optics, transformation of those quantities to the physical frame of reference, and the computation of integral quantities in the physical reference frame.

There are two conditions that can lead to a significant error in the measurement. The first condition arises due to transmission line noise, a spurious data word can be included in the stream of data as it is transferred to the computer. Because catastrophic effects can result from this condition, the data processing programs verify that the data is in the right order. If an error is detected the data point is discarded. The second error condition results from the occasional data points which have very large or small frequency. They are due to very large particles that do not follow the flow and to transient electronic noise not completely eliminated by the filters. A test is made to isolate these points in which each data point is compared with the running mean of previous data. If the modulus of the difference is larger than five standard deviations, the data point is not used in the processing. In a total of over 500,000 measurements, the total number of errors recorded due to these conditions was less than 10. At every measurement point, a frequency histogram was constructed for the blue and green channels. A typical

example is shown in figure 13. This histogram provided information about the proper operation of the system, i.e. filter setting, and the electronic noise.

The frequency information is utilized to calculate the flow velocity using the appropriate Doppler constant. The mean, second moment and cross-correlation between the two velocity components were evaluated using several weighting functions. The expressions used are

$$\overline{(U)}_{G,B}^{(i)} = \frac{1}{W_{G,B}^{(i)}} \sum_{n=1}^N (\omega_n)_{G,B}^{(i)} (U_n)_{G,B} \quad (3)$$

$$\overline{(U^2)}_{G,B}^{(i)} = \frac{1}{W_{G,B}^{(i)}} \sum_{n=1}^N (\omega_n)_{G,B}^{(i)} (U_n)_{G,B}^2 \quad (4)$$

$$\overline{(U_G U_B)}^{(i)} = \frac{1}{W_X^{(i)}} \sum_{n=1}^N (\omega_n)_X^{(i)} (U_n)_G (U_n)_B \quad (5)$$

with

$$W_{G,B,X}^{(i)} = \sum_{n=1}^N (\omega_n)_{G,B,X}^{(i)} \quad (6)$$

where  $(\omega)_{G,B,X}^{(i)}$  are the weighting factors and N the total number of data. The subscripts G, B refer to the velocity measured by the green and blue beams respectively, and the subscript X applies to the cross-correlation calculations. The superscript i indicates the type of weighting used. Three types of averaging were implemented: a straight forward averaging (i=1), independent velocity bias correction of the blue and green components (i=2), and the

velocity bias correction for simultaneous two component measurement ( $i=3$ ) (see reference 19). The weighting factors for each one of these cases are given by

$$(\omega_n)_G^{(1)} = (\omega_n)_B^{(1)} = (\omega_n)_X^{(1)} = 1 \quad (7)$$

$$(\omega_n)_G^{(2)} = (t_n)_G; (\omega_n)_B^{(2)} = (t_n)_B; (\omega_n)_X^{(2)} = \frac{(t_n)_B + (t_n)_G}{2} \quad (8)$$

$$(\omega_n)_G^{(3)} = (\omega_n)_B^{(3)} = (\omega_n)_X^{(3)} = \frac{1}{|U_n|} \quad (9)$$

with  $|U_n| = \sqrt{(U_n)_G^2 + (U_n)_B^2}$  and  $t_n$  the total burst time.

Of these three types of averaging, type (2) does not have any "a priori" justification and was used for comparison purposes only. Type (3), on the other hand, represents the correct velocity bias correction provided that the concentration of particles is spatially uniform. This condition is *not necessarily* satisfied in the present experiments since the primary and induced flows may have different particle concentrations.

A simple transformation relates the mean values and correlation of the measured velocity components with those in the x and y directions. This transformation is illustrated in figure 14. The equations relating the mean and the correlations of the various velocity components are

$$\bar{u} = \bar{U}_G \cos \phi - \bar{U}_B \sin \phi \quad (10)$$

$$\bar{v} = \bar{U}_G \sin \phi + \bar{U}_B \cos \phi \quad (11)$$

$$\overline{u^2} = \frac{\overline{U_G^2} + \overline{U_B^2}}{2} + \frac{\overline{U_G^2} - \overline{U_B^2}}{2} \cos 2\phi - \overline{U_G U_B} \sin 2\phi \quad (12)$$

$$\overline{v^2} = \frac{\overline{U_G^2} + \overline{U_B^2}}{2} - \frac{\overline{U_G^2} - \overline{U_B^2}}{2} \cos 2\phi + \overline{U_G U_B} \sin 2\phi \quad (13)$$

$$\overline{uv} = \frac{\overline{U_G^2} - \overline{U_B^2}}{2} \sin 2\phi + \overline{U_G U_B} \cos 2\phi \quad (14)$$

where  $\phi$  is the angle between the direction of the velocity component measured by the green beams and the downstream direction, positive in the counter-clockwise direction. The average bar indicates any of the three types of weighting described previously. From these quantities, the rms fluctuations of the  $u$  and  $v$  velocity components and their correlation can be calculated using the following relationships:

$$u' = \sqrt{\overline{u^2} - \bar{u}^2} \quad (15)$$

$$v' = \sqrt{\overline{v^2} - \bar{v}^2} \quad (16)$$

$$\overline{u'v'} = \overline{uv} - \bar{u} \bar{v} \quad (17)$$

The accuracy of the mean and the correlations of the measured  $u$  and  $v$  components of the velocity depend on a number of factors, e.g. particle concentration and spatial distribution, velocity bias(21), fringe bias(22). There is not a sufficiently general theory that allows evaluation of these effects. Existing theories based on spatially uniform concentrations of particles suggest that velocity bias effects on the mean and r.m.s. fluctuations of the measured velocity components,  $U_B$  and  $U_G$ , are small(19), 2 percent. The accuracy of these results was explored by computing the averaged values using weighting factors ( $i=1$ ) and ( $i=3$ ) described previously. Comparison among the mean  $\bar{u}$  results indicates that ( $i=3$ ) gives slightly lower values, typically

one-third of the local  $u'$  which amounts to 5 percent accuracy. The effect on  $u'$  is below 10 percent. The accuracy of  $\bar{v}$ ,  $v'$  and  $\overline{u'v'}$  are estimated as 20 percent. Only the results obtained with  $i=1$  will be presented in this report.

The flux per unit span of several relevant quantities across several downstream locations within the ejector was calculated. They are the mass flow rate

$$\dot{m} = \rho \int \bar{u} dy \quad (18)$$

the momentum flux

$$M = \rho \int [\bar{u}^2 + (u'^2 - v'^2)] dy \quad (19)$$

the mean kinetic energy flux

$$K = \rho \int [\bar{u} (\bar{u}^2 + \bar{v}^2)] dy \quad (20)$$

and the turbulent kinetic energy flux

$$k = \rho \int [\bar{u} (u'^2 + v'^2)] dy \quad (21)$$

The integrals were evaluated using Simpson's rule. The two velocity components were assumed to vary linearly from the nearest measurement point to the wall where a zero value was assumed. The error is estimated to be less than 10 percent.

### 2.3 Other Instrumentation

In addition to the velocity measurements, other measurements made in experiments conducted in the present investigation included surface pressure, direct thrust, and flow visualization. Surface pressure measurements were used to monitor the operation of the facility and to measure the static pressure distribution on the surface of the ejector shroud. Strain gauge pressure transducers were employed for these measurements. The optimum full-range values were used depending on the specific measurement since their accuracy is better than 0.1 percent of the full range value.

Direct thrust measurements of the ejector system were made using a thrust balance. A diagram of the thrust balance is shown in figure 15. A load-cell located as indicated in the figure is utilized for this measurement. A 2,000 Nw range transducer was required to measure ejector thrust at the high primary nozzle flow rates. The resolution of the measurement is 20 Nw.

Flow visualization using the shadowgraph technique was implemented with a spark source located 4 m from the top wall of the facility and the photographic plate positioned against the bottom wall. Changes in index of refraction were obtained by injecting small amounts of CO<sub>2</sub> (up to 10 percent of the mean flow) to the primary flow for low primary jet Mach numbers. For primary jet Mach number close to 1, injection of CO<sub>2</sub> was not required. The refraction effects caused by the expansion of the primary jet were sufficient to obtain good shadow effect.

### III. EXPERIMENTAL RESULTS

The experimental results on thrust, surface pressure and velocity measurements at various pressure ratios across the primary nozzle for both the primary jet and the ejector configurations are presented. Because the different quantities measured are mutually related through the fundamental conservation equations, a variety of tests were conducted which allowed verification of their consistency and accuracy. Throughout this report the coordinate system shown in figure 16 was used, the x-axis is directed downstream and the y-axis across the flow with the origin at the center of the primary jet on the mid-span plane.

#### 3.1 Primary Jet Characterization

The flow characteristics of the primary jet were explored with a pitot tube probe and shadowgraph flow visualization at various exit Mach numbers. The spanwise uniformity of the primary jet at the exit was measured with the pitot probe and found better than 0.5 percent in all cases. The free-jet characteristics for a  $M_{ex} = 0.5$  are summarized in figures 17-20.

Flow pictures at different pressure ratios up to  $p_0/p_s = 1.94$  were obtained. All the pictures showed similar features as indicated in figure 17 at  $p_0/p_s = 1.19$  ( $M_{ex} = 0.5$ ). The initial region is characterized by the presence of the potential core; its length  $x_c/h = 8$  is somewhat larger than those reported in other investigations(23,24). Further downstream the jet grows linearly with distance as expected from similarity(23-28).

A more precise measure of the jet growth can be obtained from pitot measurements. These results are shown in figure 18 where the normalized width of the jet  $\delta$ , defined as the distance between the points where the velocity is one-half the local centerline velocity, is plotted versus downstream distance.

It is found that after a region of slow growth rate, the jet width increases linearly with downstream distance. A least squares fit to the data for  $x/h > 10$  gives

$$\frac{\delta}{h} = 0.19 \frac{x - x_0}{h} \pm 0.19 \quad (22)$$

with  $x_0/h = 3.0$  where  $x_0$  is the distance to the virtual origin. This value can be compared with those obtained for the visual growth determined by the lines shown in figure 17. They give

$$\frac{\delta_v}{h} = 0.39 \frac{x - x_0}{h} \quad (23)$$

that is  $\delta_v = 2.0 \delta$ .

The decay of the centerline velocity is shown in figure 19. The velocity equals the jet velocity inside the core region and decays as  $x^{-1/2}$  further downstream. A core length of  $x_c/h = 8.5$  is obtained from these measurements, consistent with the value found from the pictures.

The expected self-similar velocity decay law is found to be

$$\frac{U_c}{U_j} = 2.68 \left( \frac{x - x_0}{h} \right)^{-1/2} \pm 0.005 \quad (24)$$

with the virtual origin located at the same distance downstream as for the growth rate.

Comparison of these data with available results is made in figure 20. The results collected in reference 24 and summarized by the continuous line in figure 20 cover Reynolds numbers up to  $Re_h = 3.4 \times 10^4$  (c.f.  $Re_h = 8.5 \times 10^4$  in these measurements). The self-similar growth rate and center-line velocity decay are found in agreement with the results of other investigations(23-28). The location of the virtual origin is also within the scatter of those measurements. The significant scatter among the results obtained by different investigators should be pointed out.

### 3.2 Constant Area Ejector

The configuration investigated in detail was chosen after some preliminary tests were conducted with constant area ejectors of different geometry, at moderate primary nozzle exit Mach numbers, from  $M_{ex} = 0.3$  to  $0.7$ . Tests were first conducted with an ejector of area ratio 16.7, nose radius of 3.8 cm and mixing chamber length of 30.5 cm. This shroud geometry had no thrust augmentation irrespective of its location relative to the primary nozzle. Flow visualization showed that within the range of primary nozzle Mach numbers and shroud locations tested, a large reverse flow region existed covering one shroud wall while the flow remained attached to the other wall. The particular shroud wall at which the flow remained attached appeared to depend on initial conditions at the start of the flow. However after the flow was established the wall at which the flow remained attached could be changed by externally inducing separation on that wall. The flow will then remain attached to the other wall even after the external disturbance was removed.

The area ratio was reduced to 13.3 while the length of the mixing chamber was maintained at 30.5 cm. Flow separation was not encountered for this area ratio with two nose radii of 3.8 cm and 5.1 cm. The thrust augmentation performance was found to improve as the shroud was moved downstream. A 10 percent increase in thrust augmentation occurred when the location of the shroud was changed from  $x = 5.1$  cm to 10.2 cm.

The geometrical parameters characterizing the final configuration are given in Table 1. The non-dimensional values are: the area ratio  $H/h = 13.3$ , the distance from the primary jet to the ejector shroud  $X/H = 1$ , mixing chamber length  $L/H = 3$ , nose radius of curvature  $R/H = 0.25$  and ejector aspect ratio  $S/H = 5$ . The primary nozzle pressure ratio was varied to achieve exit Mach numbers from 0.2 to 1.0 and underexpanded primary jet conditions.

### 3.2.1 Flow Visualization

A typical shadowgraph picture obtained at a pressure ratio  $p_0/p_s = 1.18$  ( $M_{ex} = 0.5$ ) is shown in figure 21. The general features revealed by this and other pictures are very similar to those of the free-jet (figure 17); in particular, the core length is not changed by the presence of the ejector shroud. A comparison can be made with the help of the visual growth lines of the free-jet, also drawn in figure 21. The growth rate is somewhat reduced in the presence of the ejector shroud as compared to the free-jet visual growth rate.

A second feature of interest found in the flow visualization study is the distance at which fluid from the primary nozzle first reaches the ejector shroud. This location is downstream of the region covered by the picture in figure 21 at  $x/H = 3$ .

### 3.2.2 Thrust and Surface Pressure Measurements

Measurements of the system thrust were made in order to determine the ejector thrust augmentation performance. The ejector thrust normalized with the measured primary nozzle thrust is plotted as a function of pressure ratio in figure 24. The measured values are of the order of 1.2, in agreement with previous experimental results compiled in reference 2. The variation of the thrust augmentation with pressure ratio (figure 22) shows a minimum at  $M_{ex} = 0.2$  and a maximum of 1.23 at  $M_{ex} = 1.0$ . At higher pressure ratios the thrust augmentation decreases uniformly.

Surface pressure measurements were made around the nose and along the mixing chamber at the mid-span section. These results are presented in figures 23 to 25 where the local  $C_p$  is plotted as a function of nose angle and downstream distance (see figure 5) for various pressure ratios. The local  $C_p$  is defined as

$$C_p = \frac{p - p_s}{\frac{1}{2} \rho_{ex} U_{ex}^2} \quad (25)$$

Therefore,  $C_p$  is negative in regions where the pressure is lower than ambient (i.e. suction).

The general features of the pressure distributions are a large suction around the nose, followed by a region of high adverse pressure gradient at the entrance of the mixing chamber. The pressure gradient decreases considerably in the middle section, to increase again towards the end of the mixing chamber. These features are similar to those encountered in axisymmetric constant area thrust augmenting ejectors(8).

The maximum value of the pressure coefficient (lowest pressure) is found on the nose,  $30^\circ$  from the entrance to the mixing chamber. This maximum value increases with pressure ratio from  $C_p = 0.053$  at  $p_0/p_s = 1.06$  ( $M_{ex} = 0.3$ ) to  $C_p = 0.065$  at  $p_0/p_s = 2.91$ . The pressure gradient in the entrance region of the mixing chamber increases with pressure ratio because of both an increase of the suction around the nose and a reduction of the distance along which the pressure increase occurs. Downstream of this point the measured pressure coefficients show less sensitivity to the pressure ratio.

In order to evaluate the relative contribution to the system thrust of pressure forces acting on the primary nozzle external surfaces and on the shroud walls, the thrust contribution by the shroud was calculated from the measured surface pressure distribution. This contribution,  $\Delta T_C$  is given by

$$\Delta T_C = 2RS \int_0^\pi (p_s - p) \sin\theta \, d\theta \quad (26)$$

where  $(p_s - p)$  is the local pressure differential,  $\theta$  is the angular location on the nose,  $R$  is the nose radius and  $S$  the span of the system. The

assumptions have been made that both shroud surfaces contribute equally to system thrust, skin friction can be neglected and the spanwise static pressure distribution is uniform.

The measure thrust increase  $\Delta T_M$  is

$$\Delta T_M = T_E - T_0 \quad (27)$$

The values of  $\Delta T_C$  and  $\Delta T_M$  are given in Table 3. The calculated values,  $\Delta T_C$ , are higher than the measured values,  $\Delta T_M$ , by 10 percent of the primary nozzle thrust. This result suggests a negative contribution to the system thrust due to the pressure forces acting on the primary nozzle external surfaces. Skin friction can also contribute to this result. However, the values of  $\Delta T_C$  obtained with equation (26) should be considered upper limits since the effect of spanwise non-uniformity of the pressure distribution is likely to reduce them.

### 3.2.3 Mean Velocity Results

Extensive velocity measurements were made in the ejector facility using the LDV system. Both  $u$  and  $v$  velocity components were measured on the mid-span plane at various primary jet pressure ratios inside the ejector shroud and, to a limited extent, at the entrance. Measurements were also made with the LDV operating in a single component configuration that allows positioning the focal volume 2.5 mm from the ejector shroud. Mean  $\bar{u}$  and  $\bar{v}$  velocity profiles were obtained at the downstream locations indicated in figure 16. These profiles were used to calculate the mass, momentum and kinetic energy fluxes inside the ejector.

The angle  $\phi$  between the physical frame of reference and the optical frame of reference was obtained for each profile from the condition of zero  $\bar{v}$  on the centerline. The values of  $\phi$  obtained under this assumption are given in Table 4.

The measured mean  $\bar{u}$  velocity profiles at primary nozzle pressure ratios 1.08, 1.19, 1.45 and 1.94 are presented in figures 26 to 29, respectively. The mean  $\bar{u}$  velocity profiles in the entrance region of the ejector shroud are given in figure 30 for a pressure ratio 1.19. These measurements were obtained with the LDV system operating in the standard two-component configuration. Measurements of  $\bar{u}$  inside the ejector at a pressure ratio of 1.19 were also obtained with the LDV operating in a single component configuration. They are presented in figure 31.

As expected, the velocity profiles broaden with downstream distance. Simultaneous with the spreading of the primary jet, the centerline velocity decreases with  $x$ . The centerline velocity decay is shown in figure 32 at several pressure ratios. Also plotted in this figure are the free jet results presented in figure 19. The measurements indicate a 10 percent increase of the normalized centerline velocity at the downstream end of the ejector above the measured velocity without the shroud. A small increase of the normalized centerline velocity with pressure ratio is apparent at the downstream end of the ejector.

The measured  $\bar{u}$  velocity component away from the centerline, say at  $y = \pm 4.1$  cm, in the entrance region (figure 30) is found to increase with downstream distance. Thus, the primary jet evolves in an accelerating coflowing stream. An important parameter that characterizes the evolution of the jet on a coflowing stream is the ratio of the coflowing stream velocity to the jet centerline velocity(29). This quantity varies from 0.06 at  $x = 2.5$  cm to 0.15 at  $x = 10.2$  cm. A velocity ratio of 0.29 is found inside the ejector at the entrance of the mixing chamber independent of pressure ratio. The results presented in reference 29 indicate that the coflowing stream will reduce the centerline velocity decay and the primary jet spreading rate.

The velocity variation with downstream distance at  $y = 4$  cm, inside the ejector, is shown in figure 33. The velocity decreases in the entrance of the ejector and increases further downstream. The minimum velocity is encountered at approximately  $x/H = 3$ . The reduction in the first part of the mixing chamber is a specific feature of thrust augmenting ejectors since velocity measurements in other configurations do not show this behavior(14,16). It is interesting to compare the velocity near the shroud surface with the values derived from the pressure on that surface, in the limit of incompressible irrotational flow is given by:

$$\bar{u} = U_j \sqrt{-C_p} \quad (28)$$

The calculated values of  $\bar{u}$  are also plotted in figure 33. Good agreement is found in the entrance region of the mixing chamber, up to  $x/H = 3$ . Downstream of this location the approximation is not accurate, turbulent transport of high momentum fluid towards the wall results in an increase of  $\bar{u}$  even though the pressure is also increasing.

Further insight into the velocity field near the shroud surface can be obtained from the measurements presented in figure 31. These measurements show a rapid change of the velocity profile near the wall in the entrance region of the mixing chamber. At  $x = 12.7$  cm the velocity increases as the wall is approached while at  $x = 20.3$  cm or higher, a reduction of the velocity is observed. This behavior suggests that there is a thin boundary layer on the shroud nose. Its thickness quickly increases in the large adverse pressure gradient at the entrance of the mixing chamber.

The measured mean value of the transverse velocity component,  $\bar{v}$ , inside the ejector, are shown in figures 34 to 37 for primary nozzle pressure ratios 1.08, 1.19, 1.49 and 1.94, respectively. The  $\bar{v}$  velocity profiles in the entrance of the ejector are given in figure 38. The general characteristics

of the profiles encountered in free-jets(26) are found here for  $x < 20.3$  cm. Namely, the velocity near the centerline is directed away from it, but far from it is directed towards the centerline. This second feature is associated with entrainment. An additional feature encountered in the ejector configuration is the increase of  $\bar{v}$  outside the primary jet with downstream distance observed in the entrance region (figure 38). The maximum absolute values of  $\bar{v}$  are found at  $x = 12.7$  cm inside the mixing chamber. The qualitative features of the  $\bar{v}$  velocity profiles change downstream of  $x = 20.3$  where the flow is directed away from the centerline throughout most of the cross-section. The implication of this result is that not only turbulent transport of momentum by shear stresses occurs, but also the high momentum near the centerline is being convected towards the wall in the second half of the ejector.

Of considerable interest is the downstream evolution of mass, momentum and kinetic energy fluxes through the ejector. In figure 39 the mass flow per unit span normalized with the ideal primary jet mass flow is plotted as a function of downstream distance within the ejector. The ideal mass flow was calculated using the equations

$$\dot{m}_j = \rho_0 a_0 A_{ex} M_{ex} \left( 1 + \frac{\gamma-1}{2} M_{ex}^2 \right)^{-\frac{\gamma+1}{2(\gamma-1)}} \quad (29)$$

$$M_{ex}^2 = \begin{cases} \frac{2}{\gamma-1} \left( \left( \frac{\rho_0}{\rho_s} \right)^{\frac{\gamma-1}{\gamma}} - 1 \right) & ; \frac{\rho_0}{\rho_s} < 1.893 \\ 1 & ; \frac{\rho_0}{\rho_s} > 1.893 \end{cases} \quad (30)$$

for a value of  $\gamma = 1.4$  and the measured total and ambient static pressures  $\rho_0$  and  $\rho_s$ , respectively.

If the flow is assumed perfectly two-dimensional the mass flow per unit span inside the ejector is constant, independent of downstream distance. The results shown in figure 39 for low pressure ratio ( $P_0/P_S < 1.19$ ) show 4 percent fluctuations with downstream distance too small to be significant because of experimental error (see Section 2.2.5). At high pressure ratio, a systematic increase of the measured mass flow with downstream distance is observed. Although there is some uncertainty in these results due to poor definition of the velocity profiles near the shroud surfaces, the measured increase of mass flow with downstream distance can result from the boundary layers on the top and bottom surfaces and corner flow effects which can result in significant spanwise non-uniformity of the velocity profile at the exit of the shroud. These calculations give a value for the mass flow ratio of the ejector of  $7.3 \pm 0.3$ . The mass flow ratio is defined here as the ratio of total mass flow to primary nozzle ideal flow.

The results of the momentum balance calculation are presented in figure 40 (a), (b). The momentum flux per unit span,  $M$ , normalized with the primary jet momentum per unit span is plotted in figure 40 (a) as a function of downstream distance. The momentum flux decreases within the ejector by as much as 40 percent of the primary jet momentum. Momentum conservation within the constant area section of the ejector requires the momentum flux reduction to be balanced by pressure forces, provided that skin friction and end-wall boundary layer effects are negligible. Therefore, the quantity  $M + P$  where  $P = (p - p_S)H$  should be constant independent of downstream location under those conditions. The computed values of  $M + P$  from the velocity profiles and surface pressure measurements normalized by the primary jet momentum are presented in figure 40 (b). The results at low pressure ratio support the approximations described earlier, but at high pressure ratios,  $P_0/P_S > 1.49$ , a

significant increase in  $M + P$  is observed. These calculations can also be compared with the results of the thrust measurements since the normalized momentum at the exit of the ejector shroud is the thrust augmentation ratio. The results of the calculation are significantly higher than the measured thrust efficiency which further indicates the importance of spanwise non-uniformity of the flow.

The calculated values of the mean kinetic energy flux are presented in figure 40. It has been demonstrated that kinetic energy dissipation is one of the essential features of ejector operation<sup>(30)</sup>. It is therefore not surprising that rather small amounts of kinetic energy are left at the exit of the ejector, 30 percent of the primary jet kinetic energy. The striking feature revealed by these measurements is that the dissipation occurs primarily in the entrance region of the ejector where more than 50 percent of the kinetic energy is dissipated. These calculations do not include the contribution to the mean kinetic energy flux of the spanwise velocity component.

#### 3.2.4 Turbulence Measurements

Turbulent fluctuations were measured inside the ejector at the same conditions and locations as the mean velocity. The measured quantities include the rms value,  $u'$  and  $v'$  components of the velocity fluctuations, and the velocity correlation  $\overline{u'v'}$ . The accuracy of these results depends on the particular parameter under consideration. For the rms fluctuation of the downstream velocity component the resultant accuracy is 10 percent after normalization. The accuracy of  $v'$  and  $\overline{u'v'}$  is 20 percent after normalization.

The measured rms values of the downstream velocity,  $u'$ , normalized with the local centerline velocity,  $u_c(x)$ , at several downstream positions and pressure ratios are given in figure 42. Pressure ratio within the range

covered does not significantly influence the profiles. The profiles have a local maximum on each side of the centerline. The value at the peaks is independent of downstream location  $u'/u_c = 0.25$ . The minimum value at the centerline is  $u'/u_c = 0.2$ . The distance between maxima increases with downstream distance for  $x < 35.6$  cm. The last two profiles do not show appreciable changes.

The measured  $u'/u_c$  using the single component LDV configuration at a pressure ratio of 1.19 ( $M_{ex} = 0.5$ ) are shown in figure 43. These profiles are in agreement with the results presented in figure 42. Near the wall, measurements show the development of a local maximum at  $x = 20.3$  cm which is not found further downstream.

The measured rms values of the transverse velocity fluctuation,  $v'$ , normalized with local centerline velocity are given in figure 44 for various downstream locations within the ejector and four pressure ratios. The variations with pressure ratio are within measurement error. In contrast with the  $u'$  results, these profiles show a single peak at the centerline. The maximum value  $v'/u_c = 0.18$  is slightly lower than that found for  $u'/u_c$  at the same location.

The measured velocity correlation,  $\overline{u'v'}$ , normalized with the local centerline velocity squared is plotted in figure 45. These profiles were obtained at the same locations and pressure ratios as the  $v'/u_c$  measurements. The scatter found with pressure ratio is within the measurements uncertainty.

A positive  $\overline{u'v'}$  velocity correlation indicates turbulent transport of downstream momentum in the positive  $y$ -direction. At the entrance of the ejector shroud, significant values of  $\overline{u'v'}$  are found only in the primary jet. They indicate transport of downstream momentum away from the jet. The low values found in the entrance region outside the primary jet are consistent

with the agreement found between the measured velocity and the calculated values from the surface pressure (see figure 33). Downstream of  $x = 27.9$  cm, non-negligible  $\overline{u'v'}$  correlation is measured near the wall. This indicates transfer of momentum to the wall region. In each profile, a maximum absolute value of  $\overline{u'v'}/u_c^2 = 0.03$  is found. Its location continually moves away from the centerline up to the last two downstream locations where no significant changes are observed.

Shown in figure 46 are the turbulent kinetic energy fluxes per unit span associated with the measured velocity components. The turbulent kinetic energy flux is approximately 10 percent that of the mean flow. These results indicate a uniform decrease of the turbulent kinetic energy within the ejector at low pressure ratios. At a pressure ratio of 1.94 an increase of the turbulent kinetic energy flux is observed in the first half of the mixing chamber.

#### IV. DISCUSSION

The discussion of these results will focus on two general areas selected because of their relevance to the design of a thrust augmenting ejector for aircraft applications. They are: modification of the two-dimensional jet characteristics introduced by the ejector shroud and shroud aerodynamics.

The development of the two-dimensional jet in the confined area provided by the shroud diminishes the spreading rate of the primary jet as shown by the flow visualization. The centerline velocity decay shown in figure 32 indicates that the decreased growth also occurs upstream of the region of the interaction between the turbulence and the wall ( $x/h \sim 40$ ). Possible causes for this reduction are the presence of the coflowing induced flow and the imposed pressure gradient. The presence of a coflowing stream has been shown to result in reduced growth rates of a two-dimensional jet(29). Although there is a limited region near the entrance where a favorable pressure gradient may be present, the pressure within the ejector increases downstream. The expected effect of such an adverse pressure gradient is to increase the jet growth rate. The measurements indicate that the presence of a coflowing stream dominates over the pressure gradient in the evolution of the jet.

The entrainment characteristics of the jet are also modified by the ejector shroud. In a two-dimensional free jet the entrainment velocity, i.e. the absolute value of  $v$  velocity component measured far away from the jet centerline, decreases with downstream distance. The presence of the ejector wall modifies the flow field in the entrance region ( $x < 10$  cm). The measured  $\bar{v}$  velocity component at  $y = \pm 4$  cm increases in absolute value with downstream distance as shown in figure 38.

The turbulent intensities and Reynolds stresses measured in the ejector configuration normalized with the centerline velocity are similar to those

measured in free jets(23,26). This result suggests that the underlying turbulent structure is not significantly modified by the presence of the shroud. However, the evolution of the  $u'$ ,  $v'$  and  $\overline{u'v'}$  profiles is strongly influenced by the presence of the shroud.

The basic mechanism that determines the pressure distribution on the shroud surface and therefore the thrust augmentation is what we refer to as ejector aerodynamics. There are two distinct regions in the ejector shroud: the entrance region and the interaction region. The flow field in the entrance region can be characterized as inviscid and incompressible flow. The pressure distribution can be approximately obtained using Bernoulli's equation as shown in figure 33. For the configuration investigated the pressure distribution shows a sharp peak around the nose followed by a rapid pressure rise and a relatively constant pressure region (figures 23 to 25). Because of the adverse pressure gradient, flow separation is likely to occur in this area.

The interaction region was defined as the region where the jet evolution is directly influenced by the ejector shroud. From the point of view of ejector aerodynamics this region is characterized by a steepening of the surface pressure gradient. Other features are an increase of the velocity near the wall (figure 33), non zero  $\overline{u'v'}$  velocity correlation near the wall (figure 45) and mixed fluid along the wall in the flow visualization pictures. Each one of these features allows an independent characterization of the origin of this region which varies between  $x/H = 2.75$  to  $3.5$  depending on the particular feature used. The fundamental process in this section is the turbulent transport of momentum into the wall region.

The measured mass flow through the ejector gives a mass flow ratio between the total and primary flows of approximately 7. The momentum flux

calculation gives a thrust augmentation in the range 1.3 to 1.4. Comparison of these values with thrust measurements suggests that the neglected end walls momentum deficit has a significant negative contribution to the ejector performance. Furthermore these results suggest that significant pressure gradients occur at the entrance section, where the local wall pressure can not be assumed constant throughout the cross-section. The degree of mixing can be characterized for the purpose of ejector performance by the parameter

$$\eta = \frac{\int \rho u^2 dA}{\int \rho \langle u \rangle^2 dA} \quad (31)$$

$$\langle u \rangle = \frac{1}{\rho A} \int \rho u dA$$

This parameter was calculated from the measured data. It varies from a value of 1.5 at the entrance to 1.2 at the exit of the ejector. Pressure ratio did not significantly influence these results. The exit values can be compared with the values found with hypermixing nozzles  $\eta = 1.01-1.03$ (7). These exit values, as well as those presented in reference 7, are based on a single velocity profile. Spanwise non-uniformities can significantly alter these results. These effects will be further studied and will be presented in the final report of this effort.

## V. CONCLUSIONS

1. The primary jet growth rate is significantly reduced in the ejector configuration as a result of the coflowing induced flow. Associated with this phenomena, the centerline velocity decay is reduced by 10 percent at the ejector exit.

2. The values of normalized turbulent properties are in agreement with those of a free-jet. This result suggests that the underlying turbulent structure is not modified by the presence of the shroud.

3. The observed phenomena in the neighborhood of the ejector shroud can be used to identify two distinct regions.

(a) The entrance region. It covers approximately the first half of the ejector shroud. The flow field around this area is irrotational flow except for the boundary layer near the wall. Turbulent transport is confined to the jet which does not interact with the ejector walls.

(b) The interaction region. This region extends across the second half of the ejector shroud. It is characterized by the interaction between the walls and the jet. Turbulent transport towards the wall is the most significant feature of this region.

4. The surface pressure distribution on the ejector shroud shows a large suction around the nose. The pressure recovery occurs in both regions with steepest gradient in the entrance region.

5. The effects of pressure ratio on the characteristics of ejector flow in the configuration studied are not significant.

## VI. ACKNOWLEDGEMENTS

This report presents the results of one phase of research carried out at the Jet Propulsion Laboratory, California Institute of Technology, Contract NAS7-100, Task Orders RD-182/Amendment 94, RD-182/Amendment 117, RD-182/Amendment 138, and RD-65/Amendment 369, jointly funded respectively by the Air Force Flight Dynamics Laboratory (AFFDL MIPR No. FY 14568000005), the Naval Air Development Center (MIPR No. N62269/80/MP/00034), the Air Force Office of Scientific Research (AFOSR-ISSA-81-00029), and the NASA-Ames Research Center (505-42-71-03-69). The authors extend their gratitude to Dr. K. Nagaraja, Dr. K. Green, Dr. J. Wilson, and Mr. D. Koenig for many technical suggestions throughout the program.

We extend our appreciation to Miss P. Logan for her help in acquisition and analysis of the experimental data taken with the Laser Doppler Velocimeter. The assistance of Mr. Stan Kikkert for design, fabrication, and the assembly of the experimental setup is greatly appreciated.

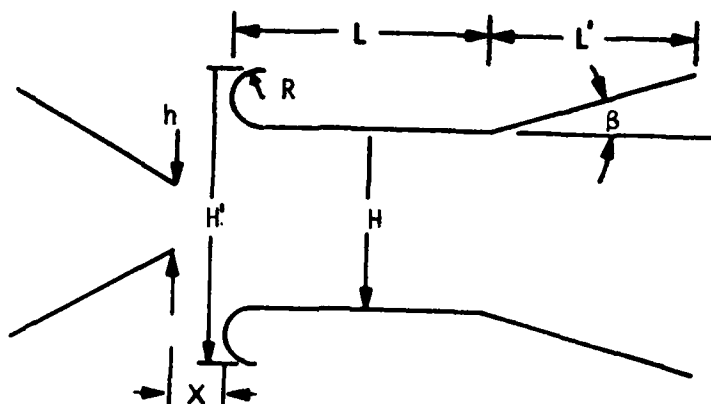
## REFERENCES

1. Viets, H. (1975) "Thrust Augmenting Ejectors" ARL 75-0224.
2. Porter, J. L. and Squyers, R. A. (1981) "A Summary/Overview of Ejector Augmentor Theory and Performance" Vols. I, II. Vought Corporation, ATC Report R-91100-9CR-47.
3. Quinn, B. (1981) "Thrust Augmenting Ejectors: A Review of the Application of Jet Mechanics to V/STOL Aircraft Propulsion" AGARD-CPP-308.
4. Green, K. A. and Cyrus, J. D. (1977) "Thrust Augmenting Ejector Technology for Navy Aircraft". AIAA paper 77-1239.
5. Whittle, D. C. and Koenig, D. G. (1980) "Large Scale Model Tests of a New Technology V/STOL Concept". AIAA paper 80-0233.
6. Quinn, B. (1973) "Compact Ejector Thrust Augmentation" J. Aircraft, vol. 10, pp. 481-486.
7. Bevilaqua, P. M. (1974) "Evaluation of Hypermixing for Thrust Augmenting Ejectors" J. of Aircraft, vol. 11, pp. 348-354.
8. Sarohia, V., Bernal, L. and Bui, T. (1981) "Entrainment and Thrust Augmentation in Pulsatile Ejector Flows" JPL Publication 81-36.
9. Von Karman, T. (1949) "Theoretical Remarks on Thrust Augmentation" Reissner Anniversary Volume, Contributions to Applied Mechanics.
10. Nagaraja, K. S. (1981) "Some Ejector Characteristics" AIAA paper 81-1679.
11. Nagaraja, K. S., Hammond, D. L. and Graetch, J. E. (1973) "One-Dimensional Compressible Ejector Flows". AIAA paper 73-1184.
12. Hill, P. G. (1965) "Turbulent Jets in Ducted Streams" J. F. M., vol. 22, pp. 161-186.
13. Hill, P. G. (1967) "Incompressible Jet Mixing in Converging-Diverging Axisymmetric Ducts" J. of Basic Engineering, March 1967, pp. 210-220.
14. Hickman, K. E., Hill, P. G. and Gilbert, G. B. (1972) "Analysis and Testing of High Entrainment Single-Nozzle Jet Pumps with Variable-Area Mixing Tubes". NASA CR-2067.
15. Bevilaqua, P. M. (1978) "Lifting Surface Theory for Thrust-Augmenting Ejectors". AIAA Journal, vol. 16, pp. 475-481.
16. Gilbert, G. B. and Hill, P. G. (1973) "Analysis and Testing of Two-Dimensional Slot Nozzle Ejectors with Variable Area Mixing Sections". NASA CR-2251.

#### REFERENCES (cont.)

17. Mefferd, L. A. and Bevilaqua, P. M. (1978) "Computer-Aided Design Study of Hypermixing Nozzles" NR 78H-91.
18. Chigier, N.A., Ungut, A. and Yule, A.J. (1978) "Particle Size and Velocity Measurement in Flames by Laser Anemometer", 17th International Symposium on Combustion, University of Leeds.
19. Drain, L. E. (1980) "The Laser Doppler Technique" John Wiley & Sons, London.
20. Friedlander, S. K. (1977) "Smoke, Dust and Haze. Fundamentals of Aerosol Behavior" John Wiley & Sons, New York.
21. McLaughlin, D.K. and Tiederman, W.G. (1973) "Biasing Correction for Individual Realization of Laser Anemometer Measurements in Turbulent Flows", The Physics of Fluids, Vol. 16, pp. 2082-2088.
22. Dimotakis, P.E. (1976) "Single Scattering Particle Laser Doppler Measurements of Turbulence" AGARD CP-193.
23. Van Der Hegge Zijnen, B. G. (1958) "Measurements of the Velocity Distribution in a Plane Turbulent Jet of Air" Appl. Sci. Res. Sec. A., vol. 7, pp. 256-276.
24. Harsha, P. T. (1971) "Free Turbulent Mixing: A Critical Evaluation of Theory and Experiment". AEDC TR-71-36.
25. Bradbury, L. J. S. (1965) "The Structure of a Self-Preserving Turbulent Plane Jet". J. F. M., vol. 23, pp. 31-64.
26. Gutmark, E. and Wagnanski, I. (1976) "The Planar Turbulent Jet" J. F. M., vol. 73, pp. 465-495.
27. Hussain, A. K. M. F. and Clark, A. R. (1977) "Upstream Influence on the Near Field of a Plane Turbulent Jet". The Physics of Fluids, vol. 20, pp. 1416-1426.
28. Kotsovinos, N. E. (1976) "A Note on the Spreading Rate and Virtual Origin of a Plane Turbulent Jet" J. F. M., vol. 77, pp. 305-311.
29. Bradbury, L. J. S. and Riley, J. (1967) "The Spread of a Turbulent Plane Jet Issuing into a Parallel Moving Airstream" J. F. M., vol. 27, pp. 381-394.
30. Viets, H. (1977) "Thrust Augmenting Ejector Analogy" J. of Aircraft, vol. 14, pp. 409-411.

Table 1. Dimensions of the Ejector System



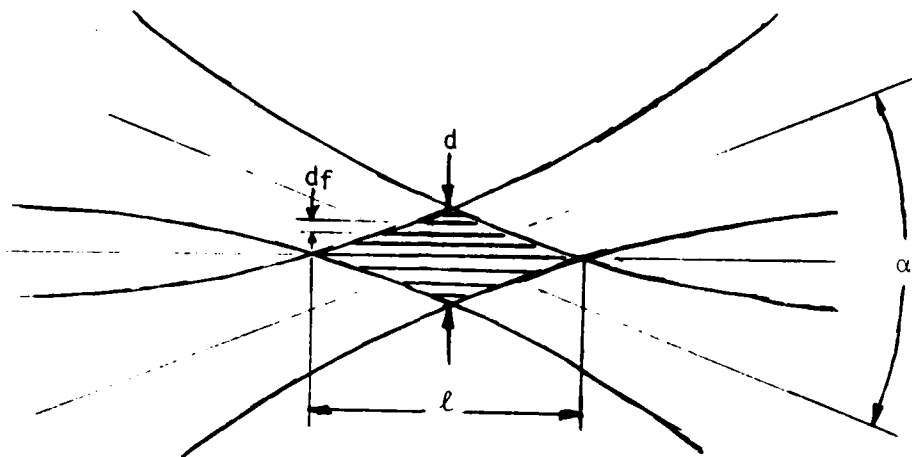
Physical Dimensions

Span,  $S = 50.8$  cm  
 Primary jet width,  $h = 0.762$  cm  
 Ejector width,  $H = 10.2$  cm  
 System width,  $H' = 20.3$  cm  
 Mixing chamber length,  $L = 30.5$  cm  
 Diffuser length,  $L' = 20.3$  cm  
 Diffuser angle,  $\beta = 5^\circ$   
 Nose radius,  $R = 2.5$  cm

Normalized Parameters

Primary jet aspect ratio,  $S/h = 66.7$   
 Mixing chamber aspect ratio,  $S/H = 5.0$   
 Ejector area ratio,  $H/h = 13.3$   
 Diffuser area ratio, 1.35  
 Mixing chamber length ratio,  $L/H = 3.0$   
 Normalized nose radius,  $R/H = 0.25$   
 Normalized system length:  
 Constant area ejector, 4.3  
 Constant area mixing chamber and  
 diffuser, 6.3

Table 2. Laser Doppler Velocimeter Focal Volume Characteristics



Lens focal length,  $f = 598 \text{ mm}$

Beams crossing angle,  $\alpha = 4.72^\circ$

Beams diameter,  $D_{e-2} = 1.3 \text{ mm}$

Focal volume length\*,  $l = 7.3 \text{ mm}$

Focal volume width\*,  $d = 0.3 \text{ mm}$

Fringe spacing\*,  $d_f = 6.1 \mu\text{m}$

Number of fringes,  $N_{fr} = 48$

\*These parameters vary by 5% for the blue and green focal volumes. The mean value is given.

Table 3. Comparison of Surface Pressure Measurements With Thrust Measurements

M	P <sub>0</sub> /P <sub>S</sub>	T <sub>0</sub> (Nw)	ΔT <sub>C</sub> <sup>(*)</sup> (Nw)	ΔT <sub>M</sub> (Nw)
0.3	1.06	39.1	10.3	7.8
0.5	1.18	113.3	28.1	23.0
0.75	1.45	263.2	64.6	58.0
1	1.94	506.7	122.5	116.5
	2	548.9	129.3	119.2
	3	1028.4	197.9	190.0

$$(*)\Delta T = 2RS \int_0^{\pi} (p_S - p) \sin \theta \, d\theta$$

Table 4. Centerline Velocity Angle in the Optical Frame of Reference

x(cm)	M <sub>ex</sub> = 0.3	M <sub>ex</sub> = 0.5	M <sub>ex</sub> = 0.75	M <sub>ex</sub> = 1
2.5	--	45.09	--	--
5.1	--	45.09	--	--
7.6	--	44.70	--	--
10.2	--	45.01	--	--
12.7	46.52	45.69	44.81	44.10
20.3	46.96	44.38	43.74	44.28
27.9	46.94	44.18	44.77	45.03
35.6	47.03	45.10	45.87	45.37
43.2	45.33	45.29	46.06	45.50

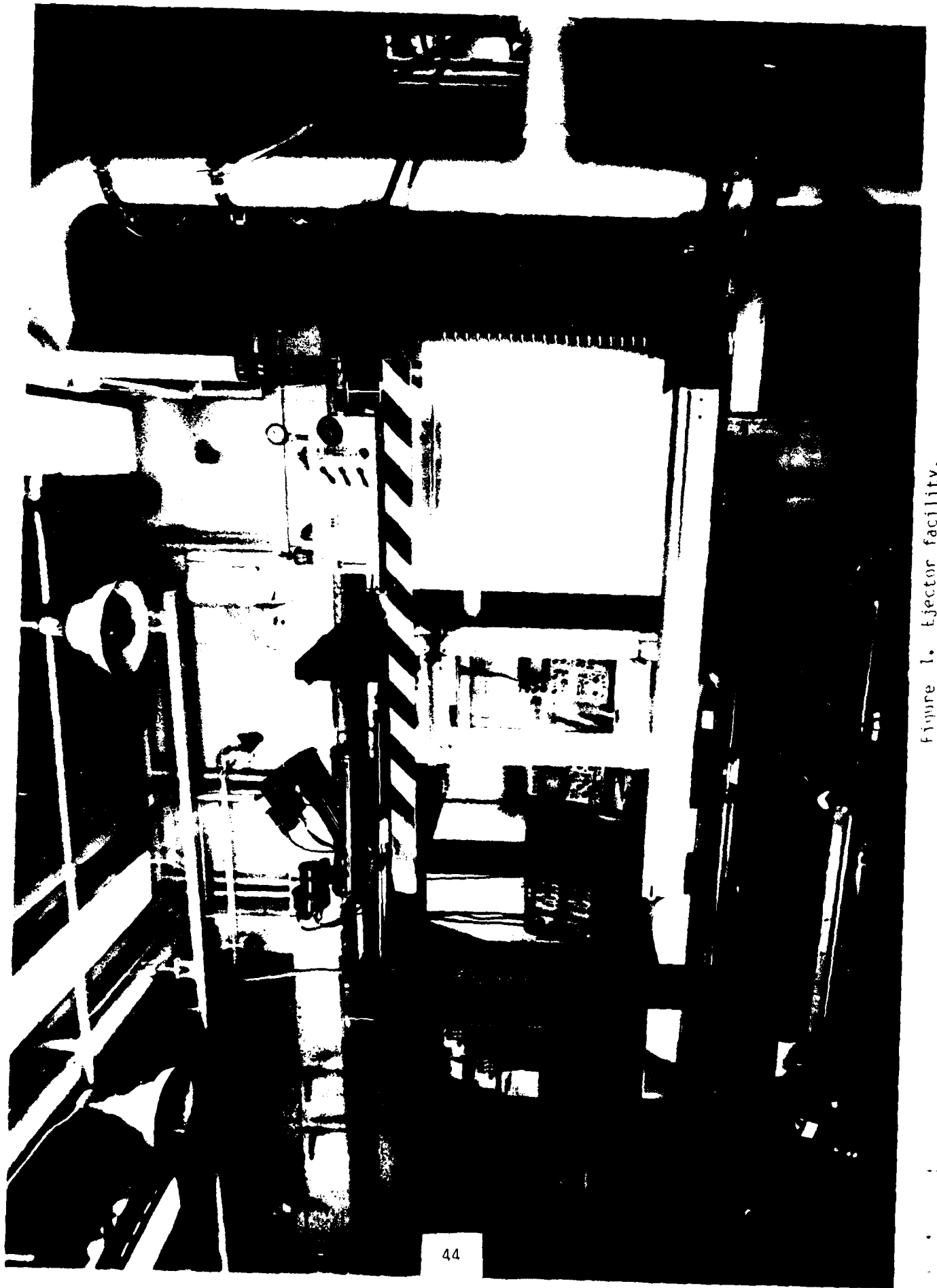


Figure 1. Ejector facility.

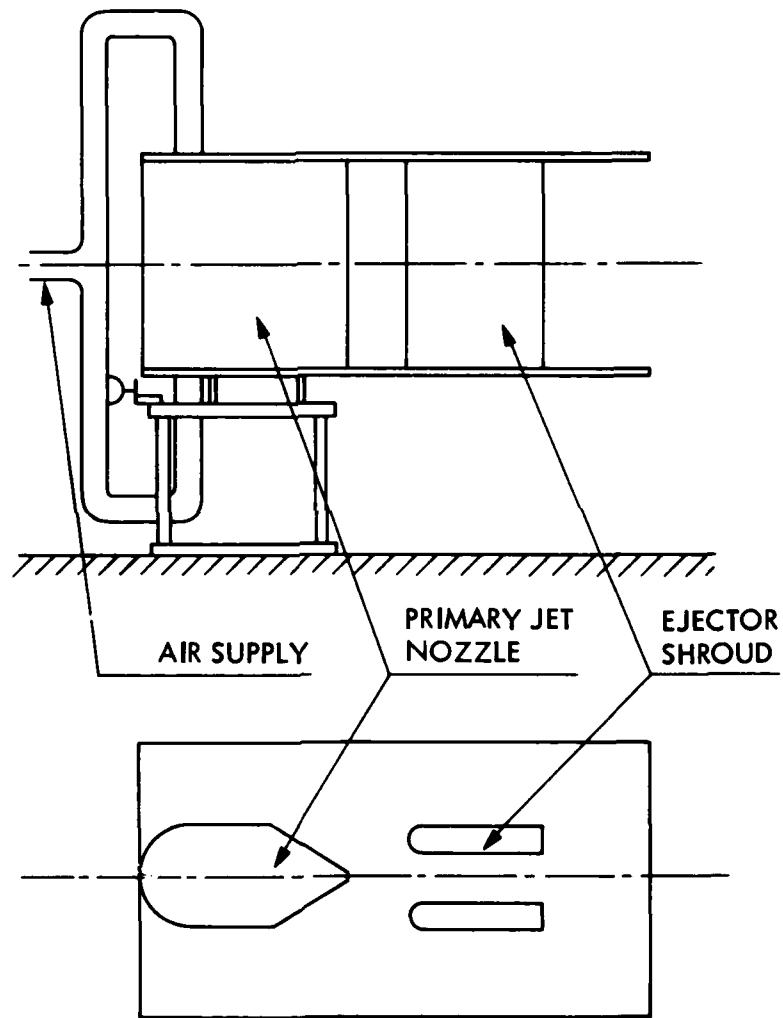


Figure 2. Diagram hardware components of ejector facility.

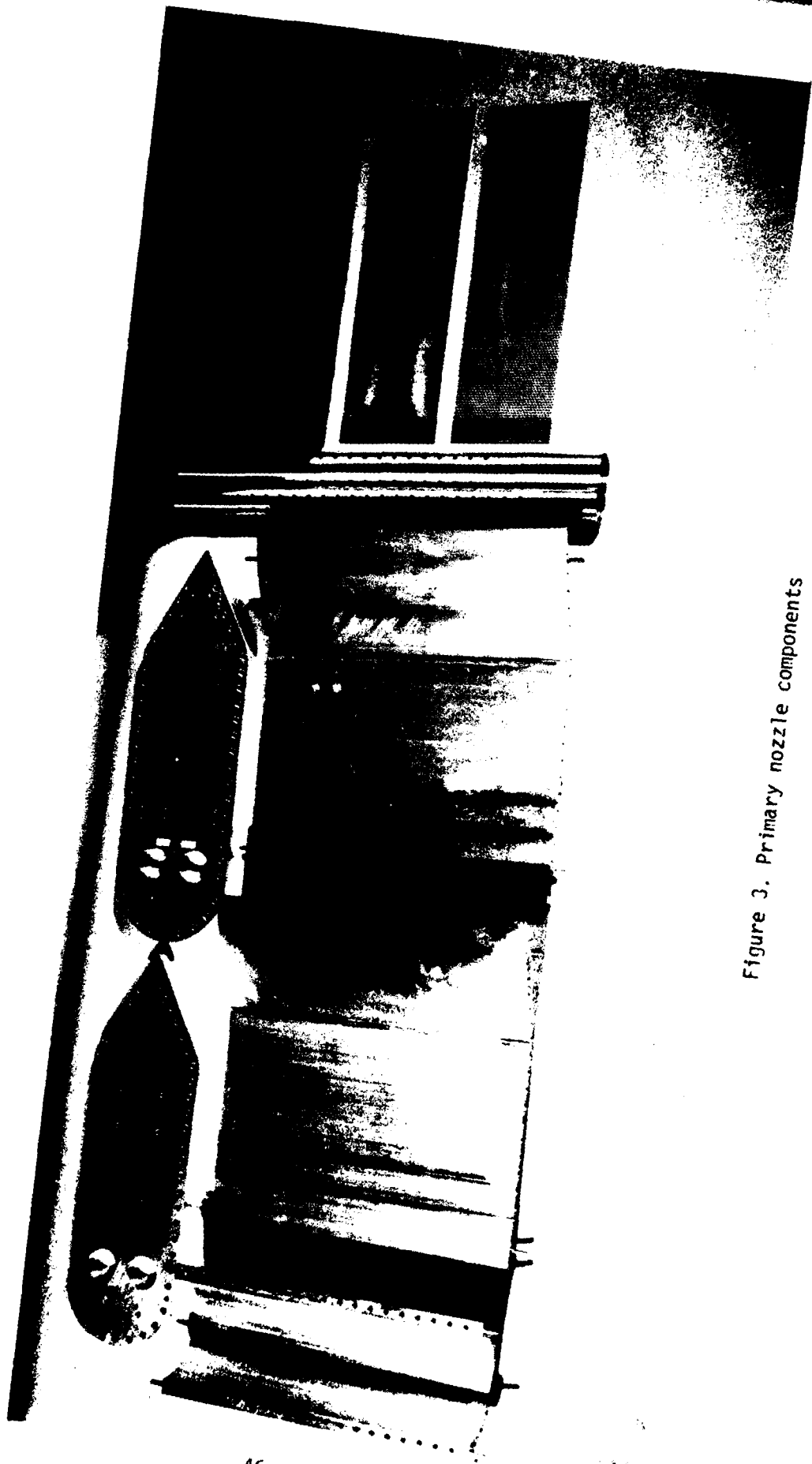


Figure 3. Primary nozzle components

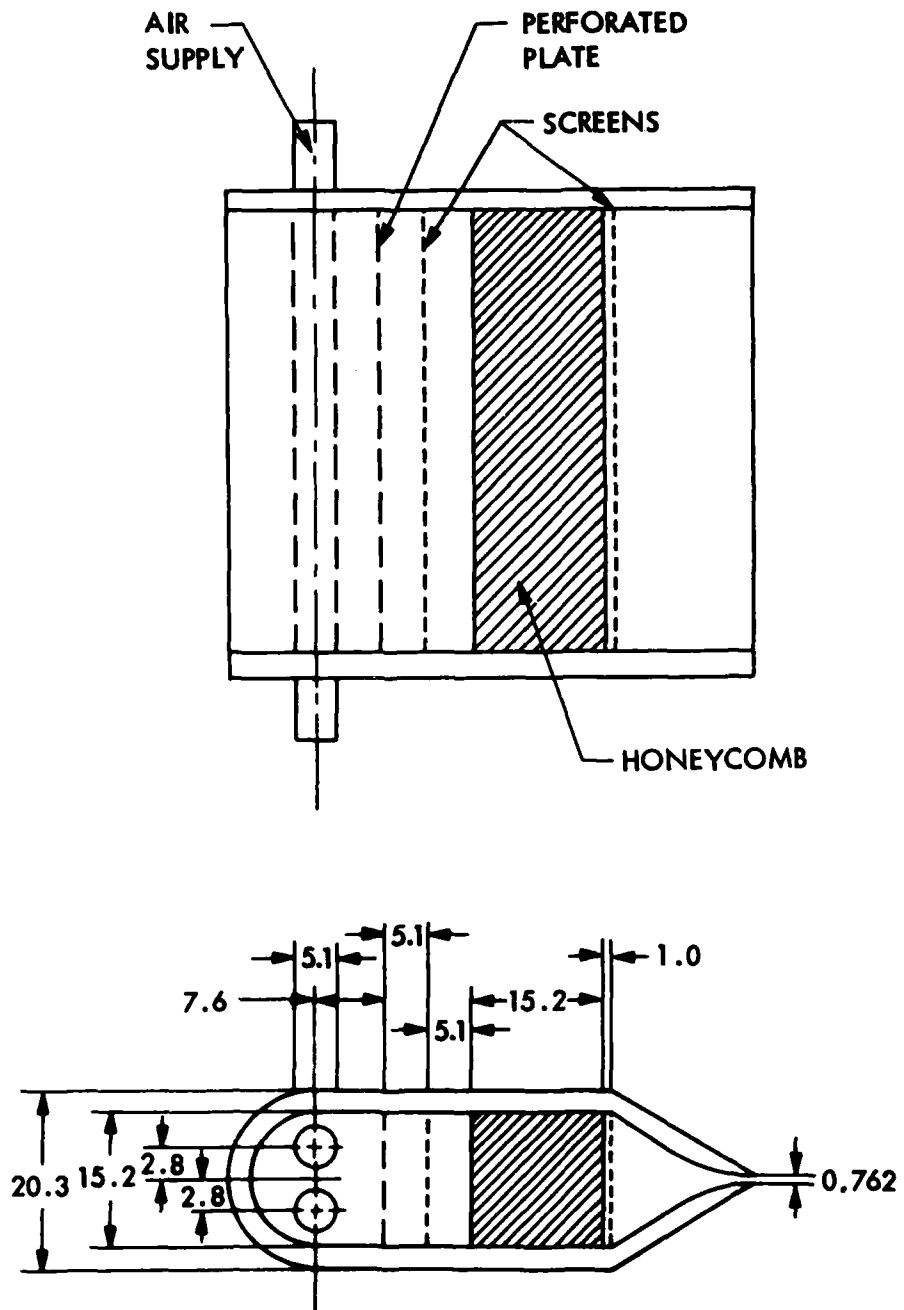


Figure 4. Primary nozzle elements position. Dimensions in cm.

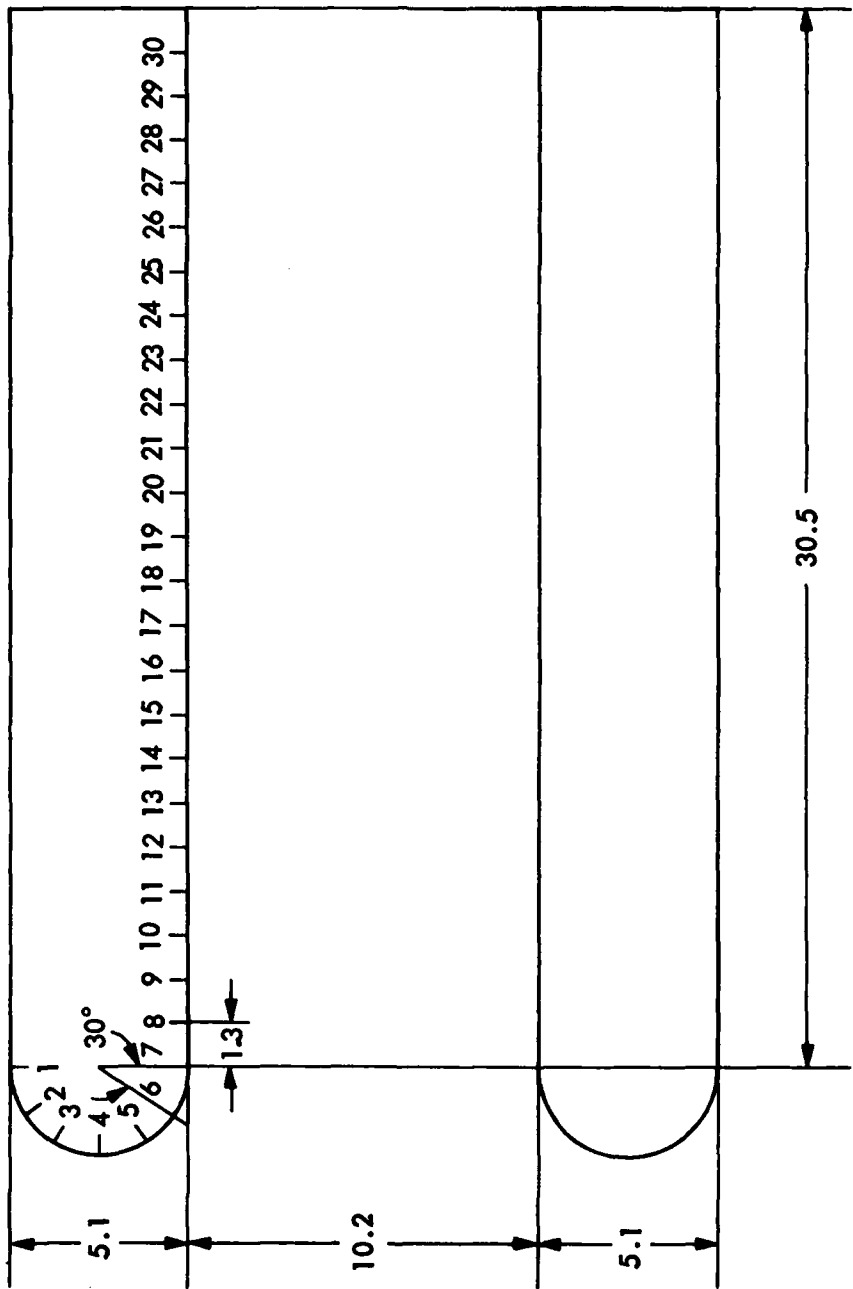


Figure 5. Ejector shroud geometry showing the location of surface pressure tabs. Dimensions in cm.

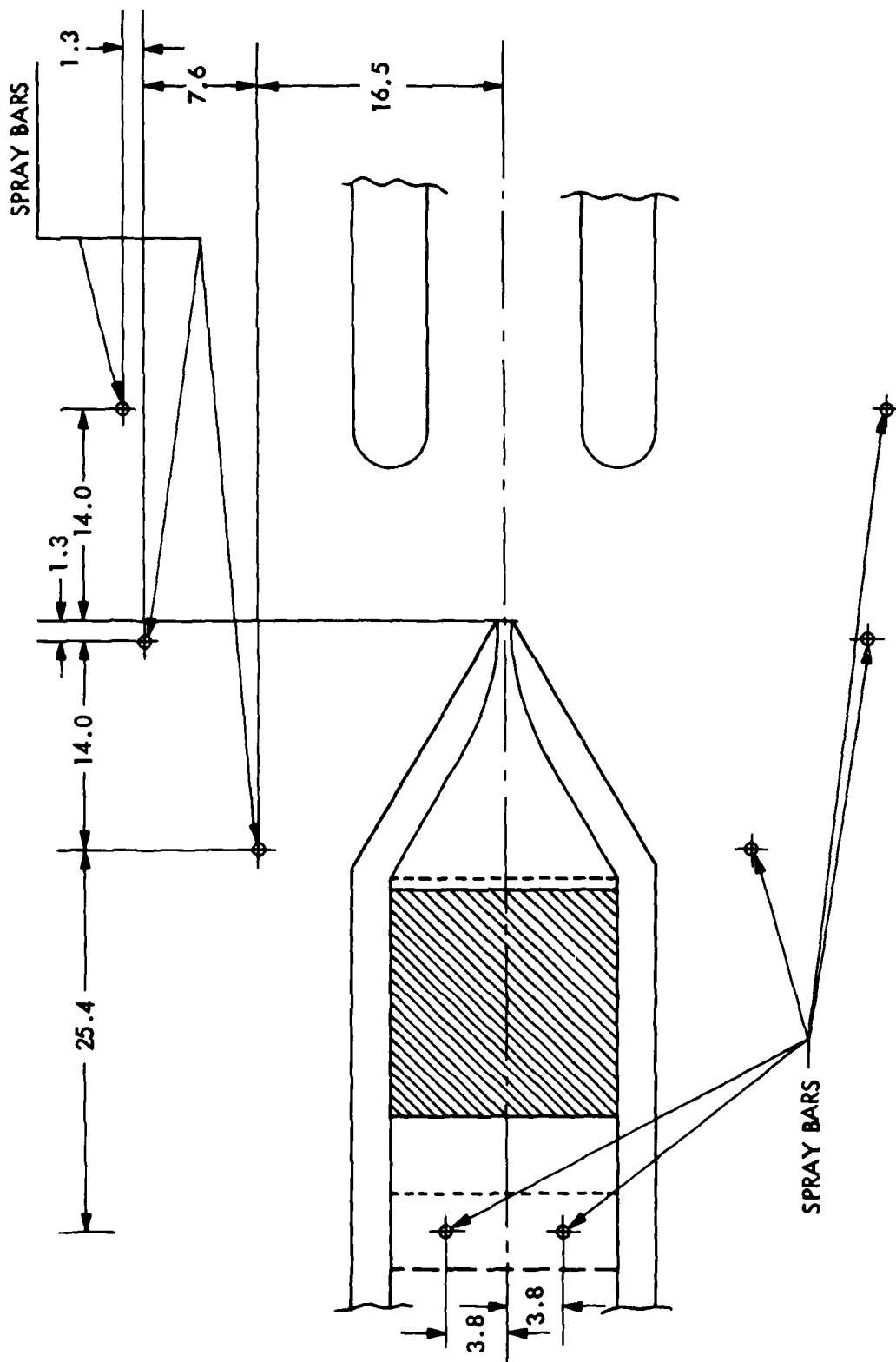


Figure 6. Primary and secondary flow injectors location. Dimensions in cm.

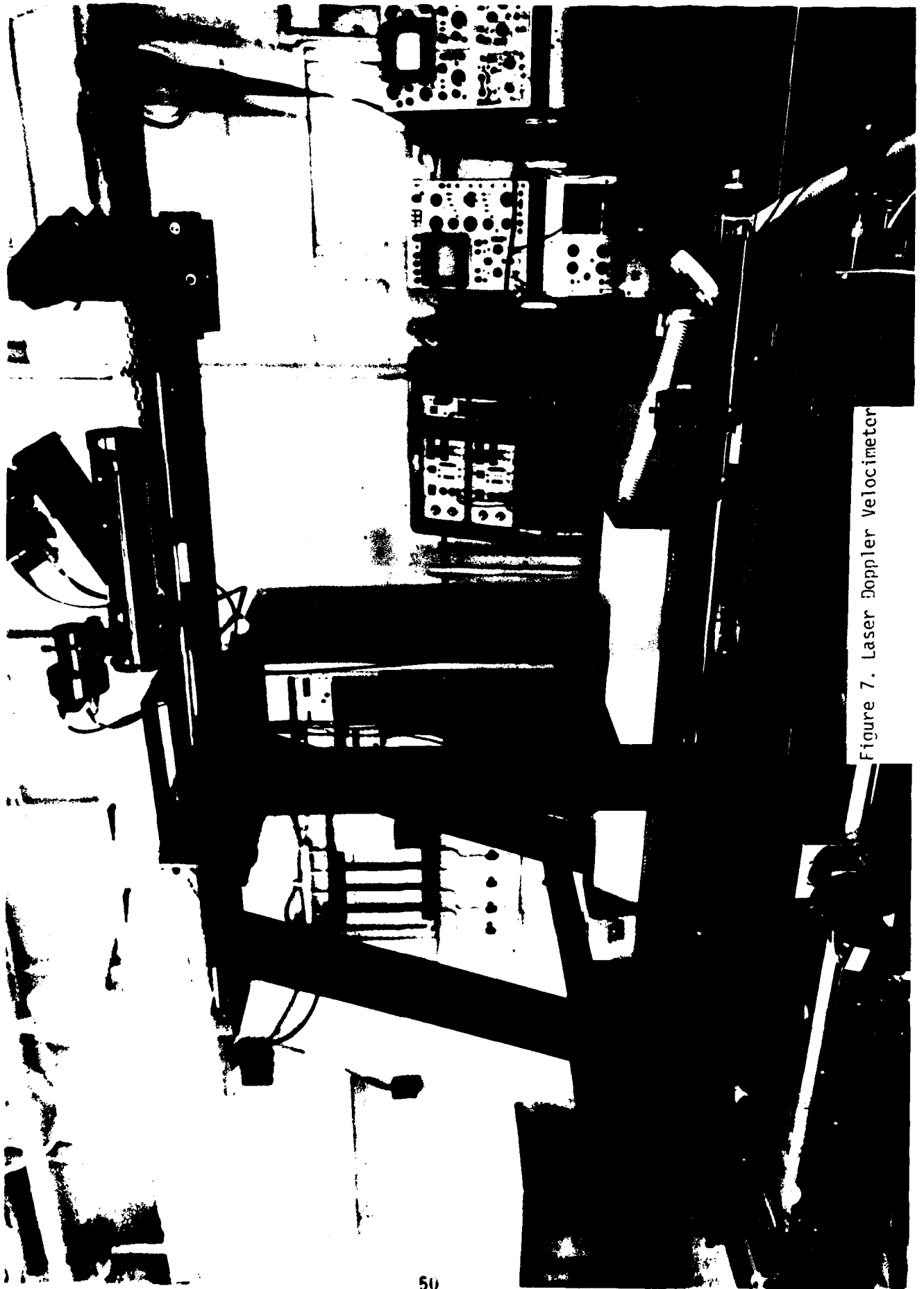


Figure 7. Laser Doppler Velocimeter

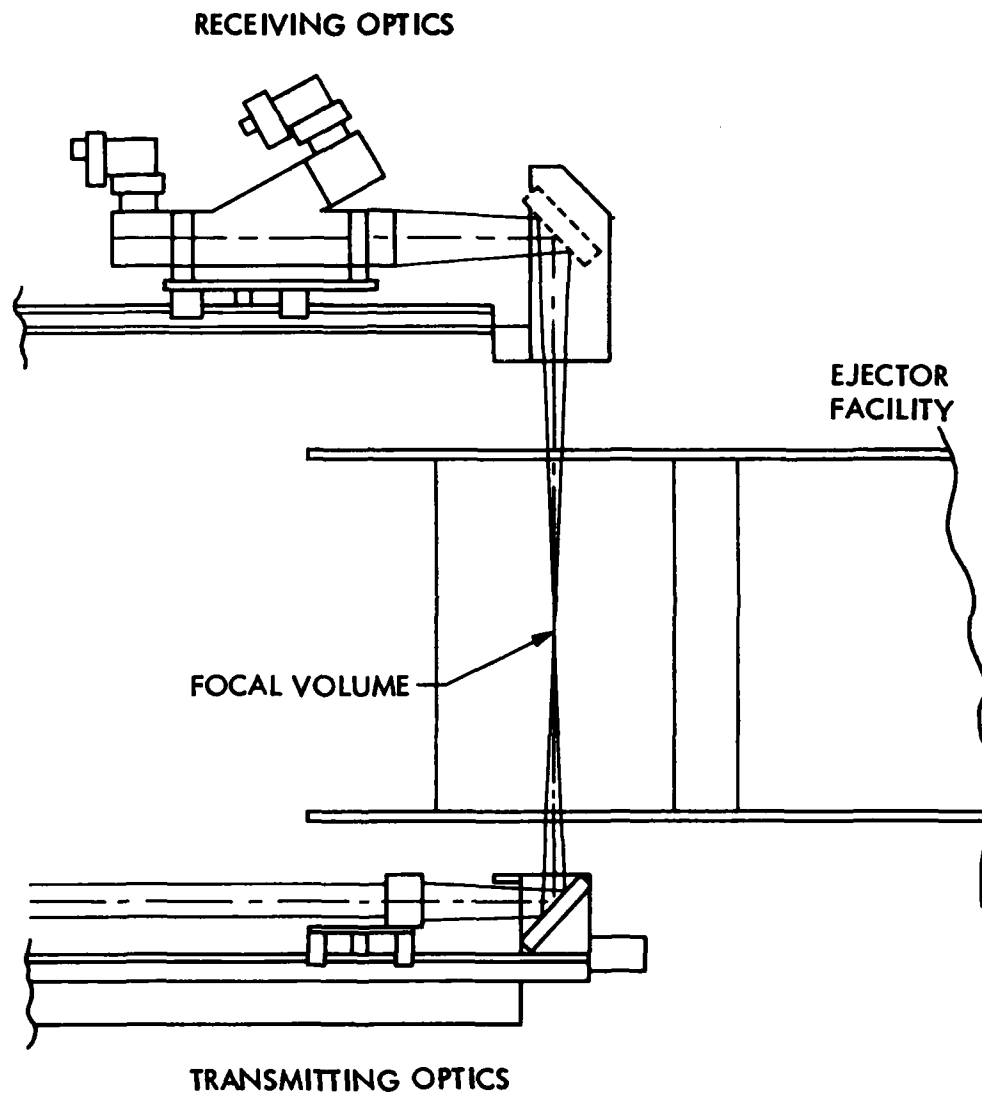


Figure 8. LDV location in relation to the test section.

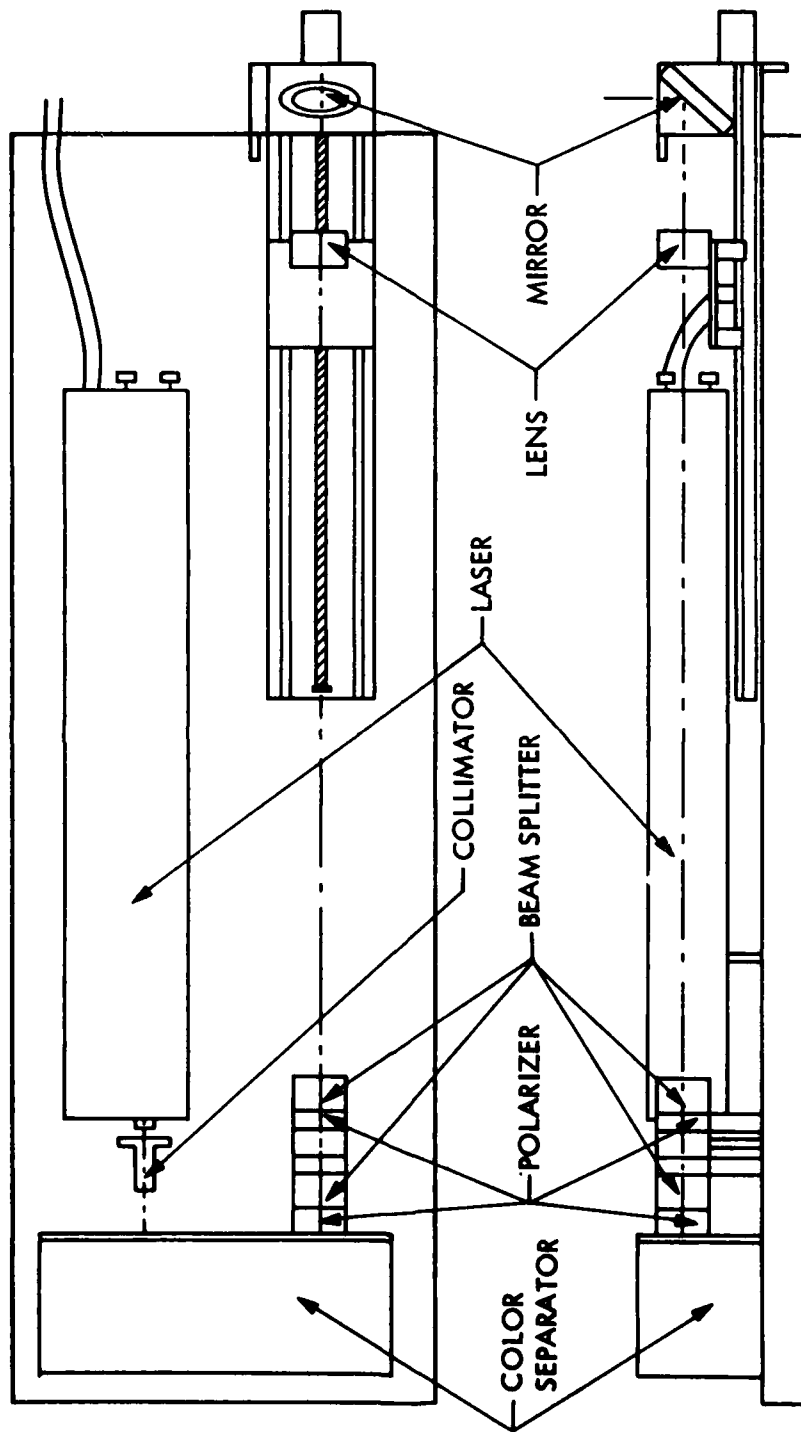


Figure 9. Transmitting optics components.

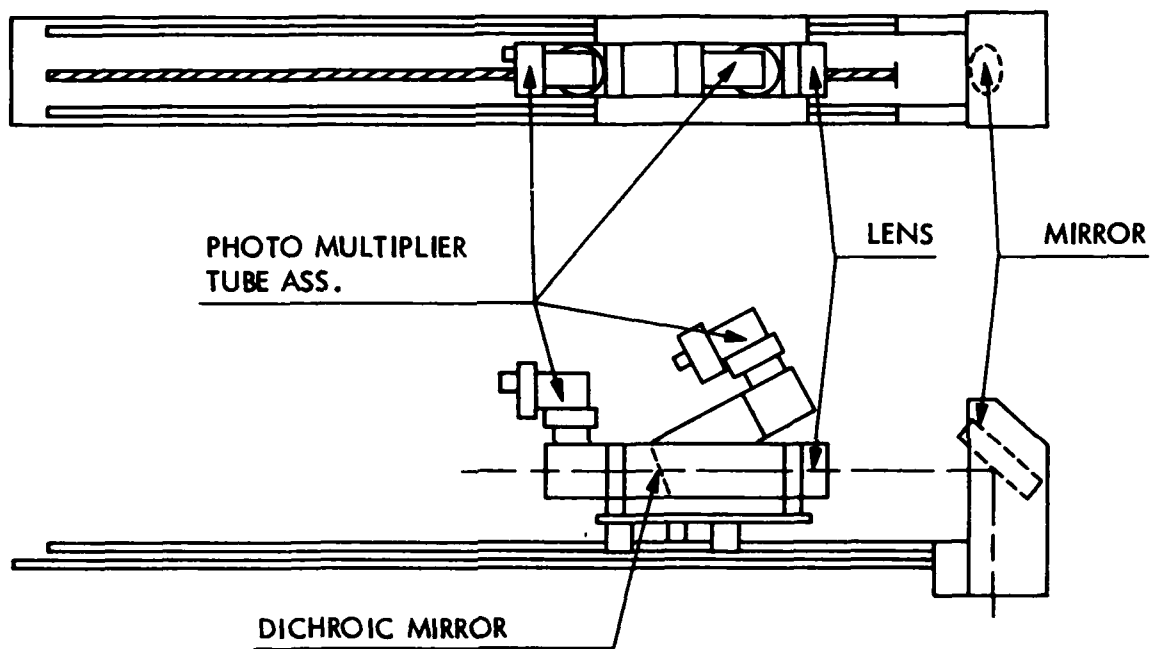


Figure 10. Collecting optics components.

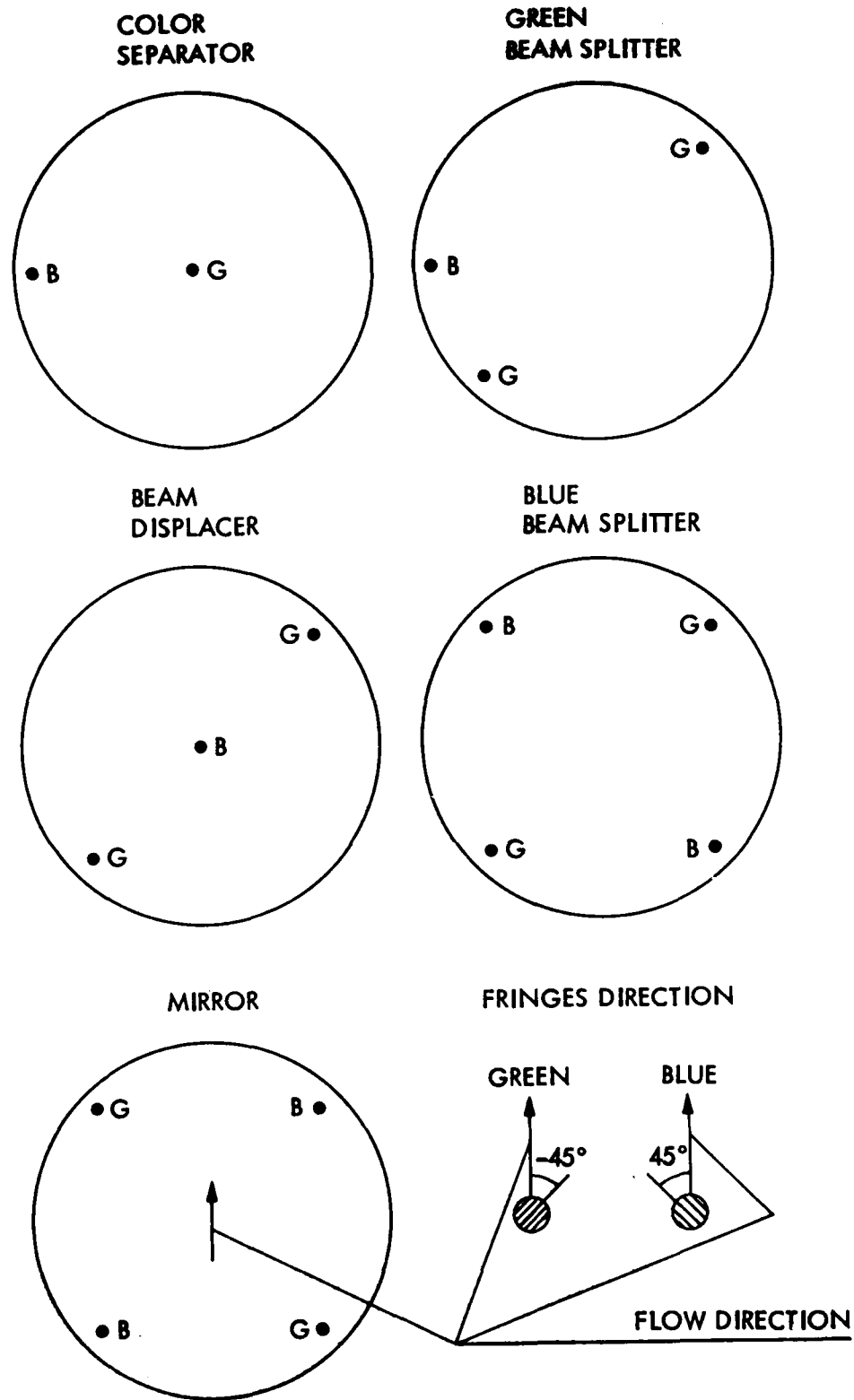


Figure 11. Focal volume formation schematic.

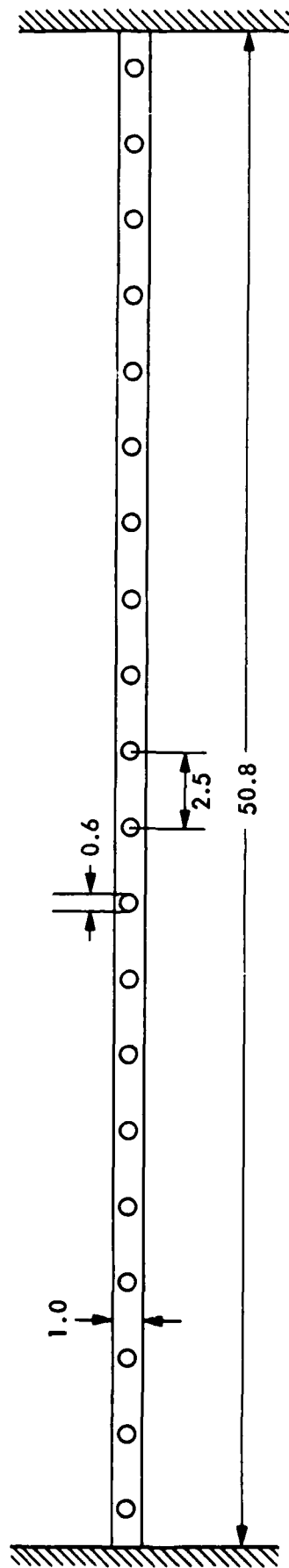


Figure 12. Spray bar geometry. Dimensions in cm.

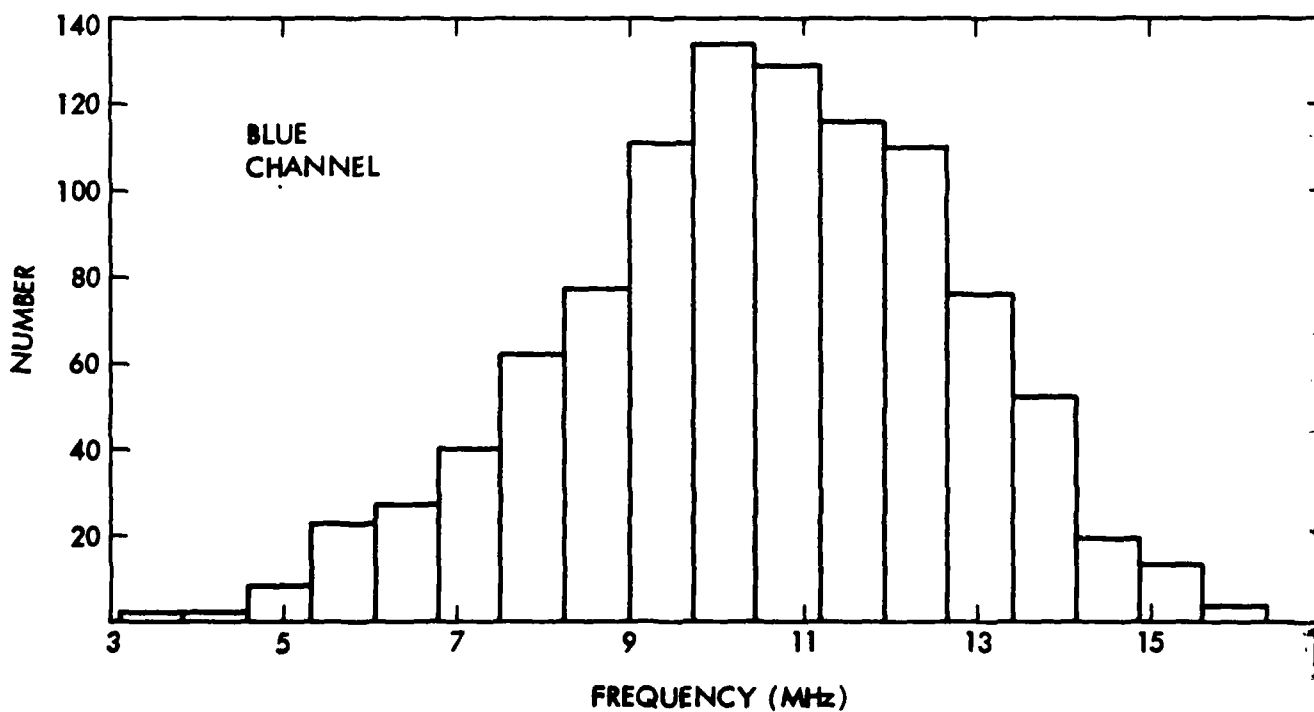
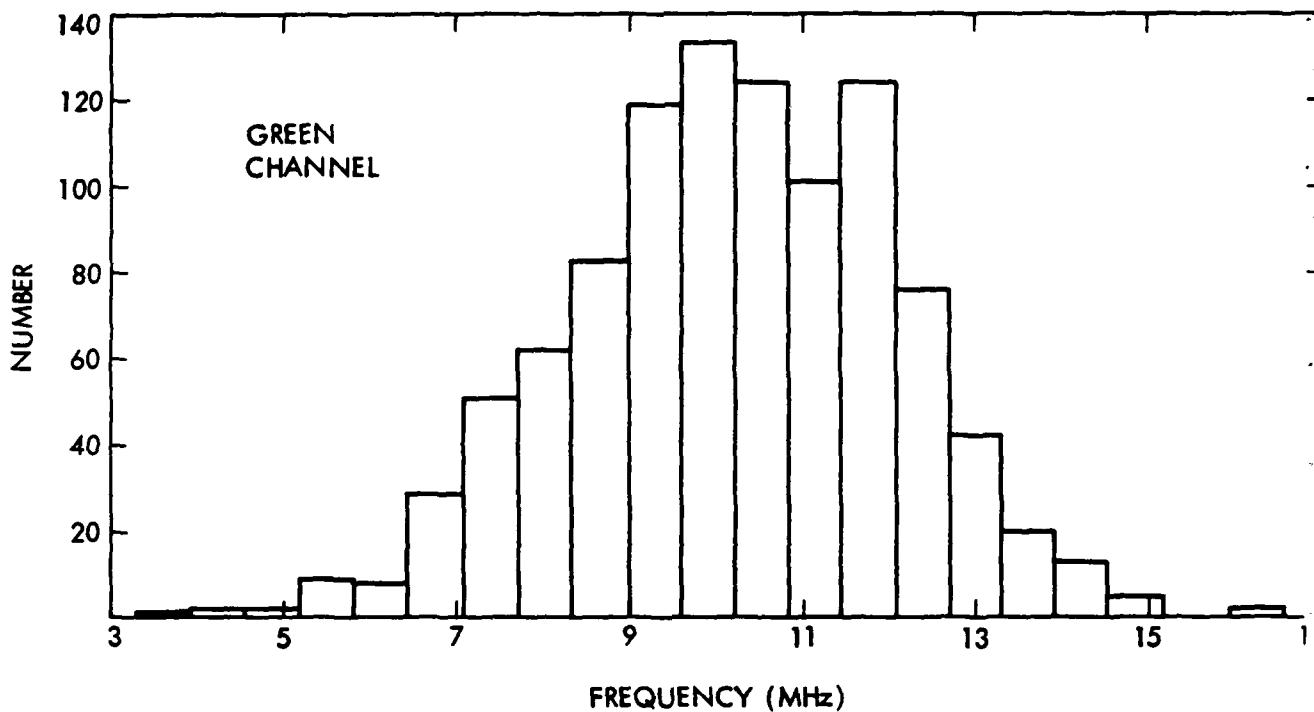


Figure 13. Typical frequency histograms.

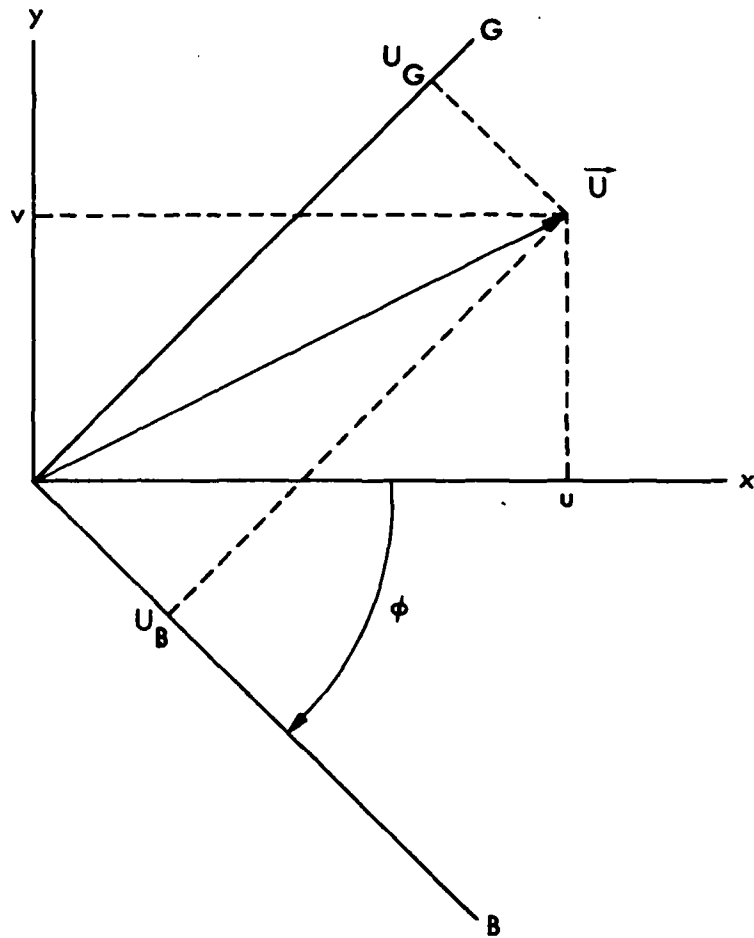


Figure 14. Velocity transformation between the optical and physical frames of reference.

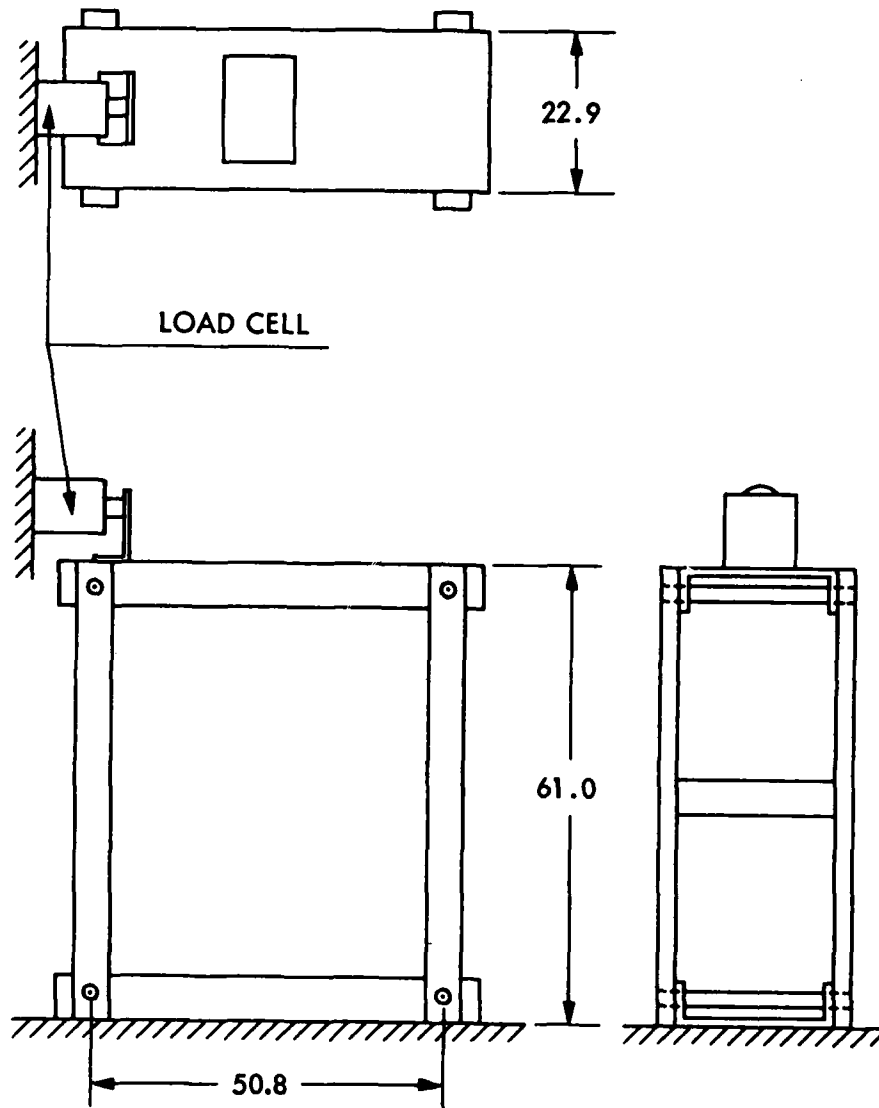


Figure 15. Thrust balance schematic. Dimensions in cm.

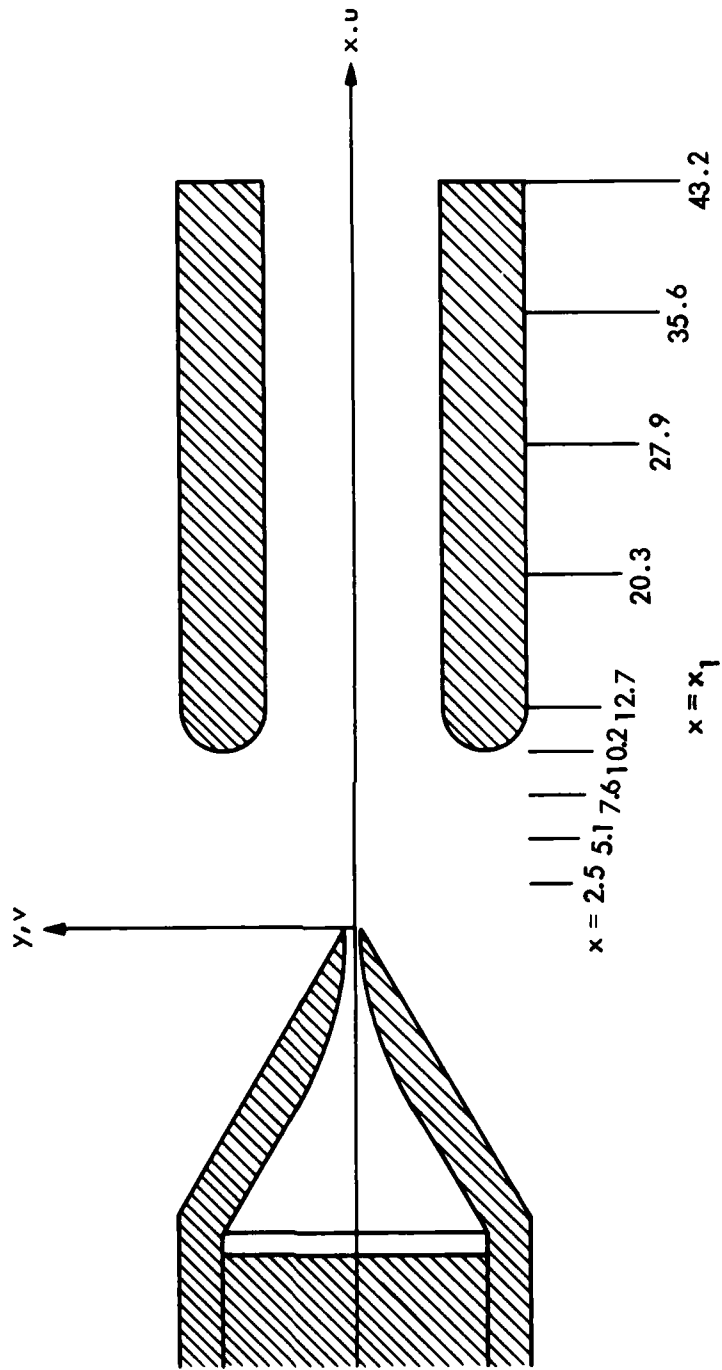


Figure 16. Ejector coordinate system and locations at which velocity profiles were obtained.

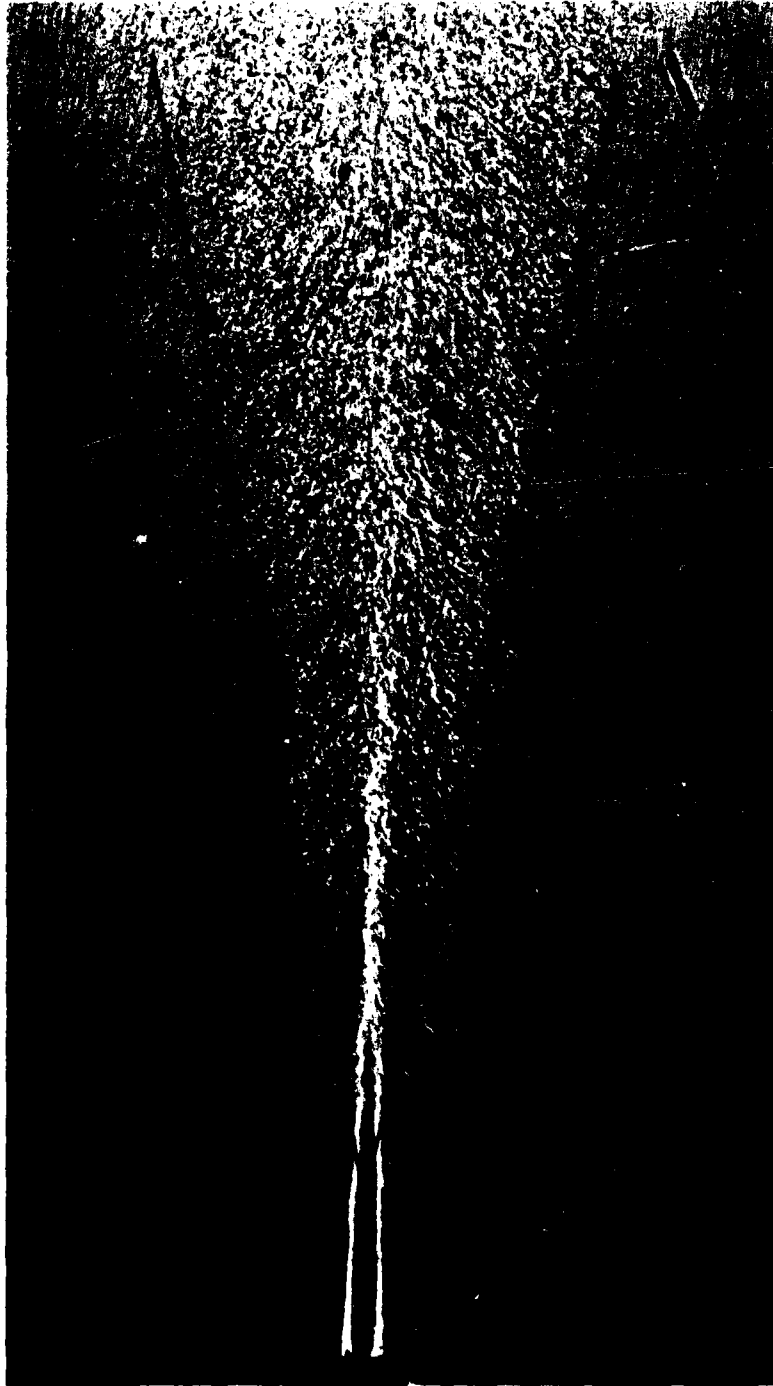


Figure 17. Shadowgraph picture free-jet  $M_{ex} = 0.5$

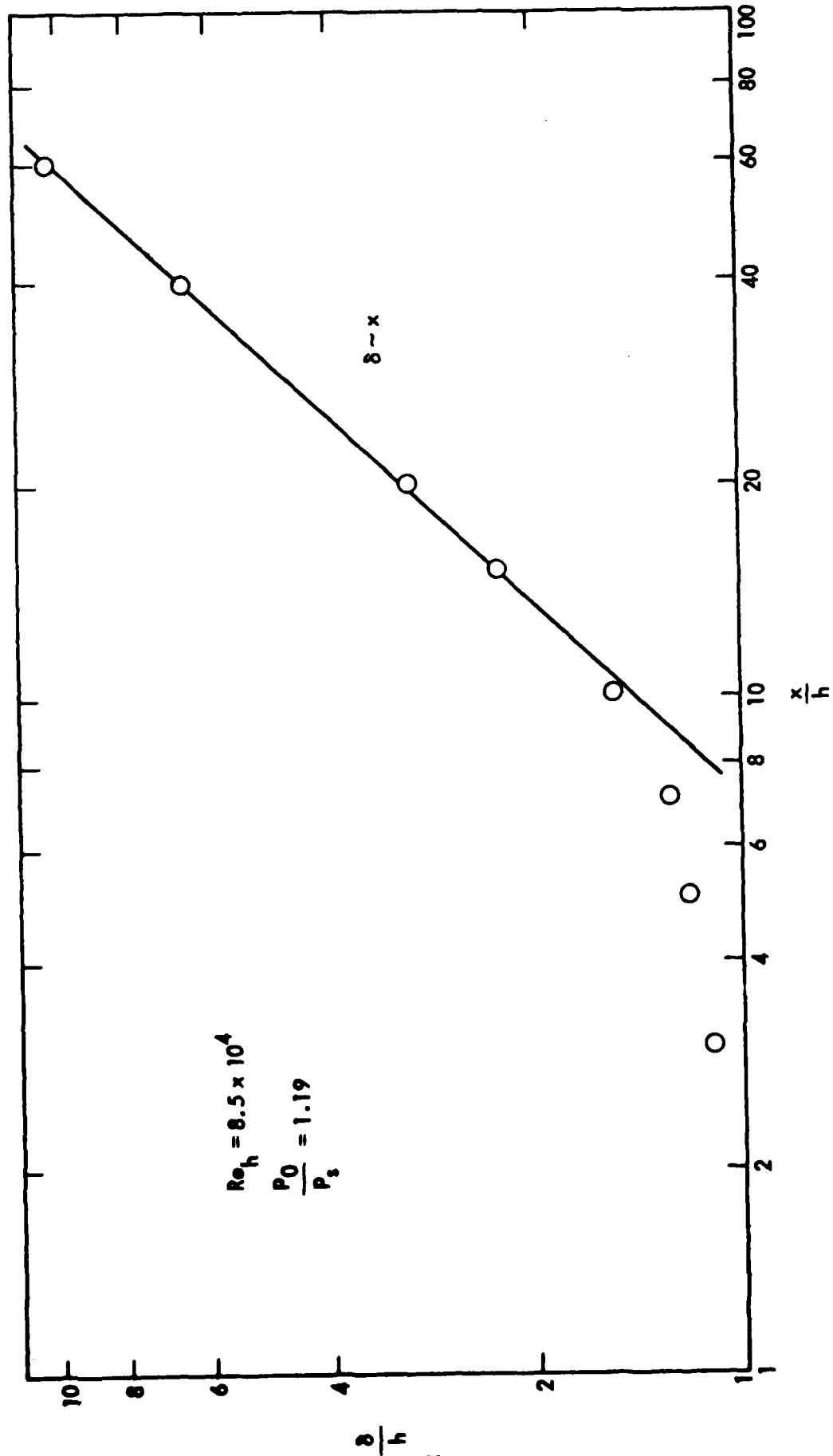


Figure 18. Normalized jet width as a function of downstream distance.

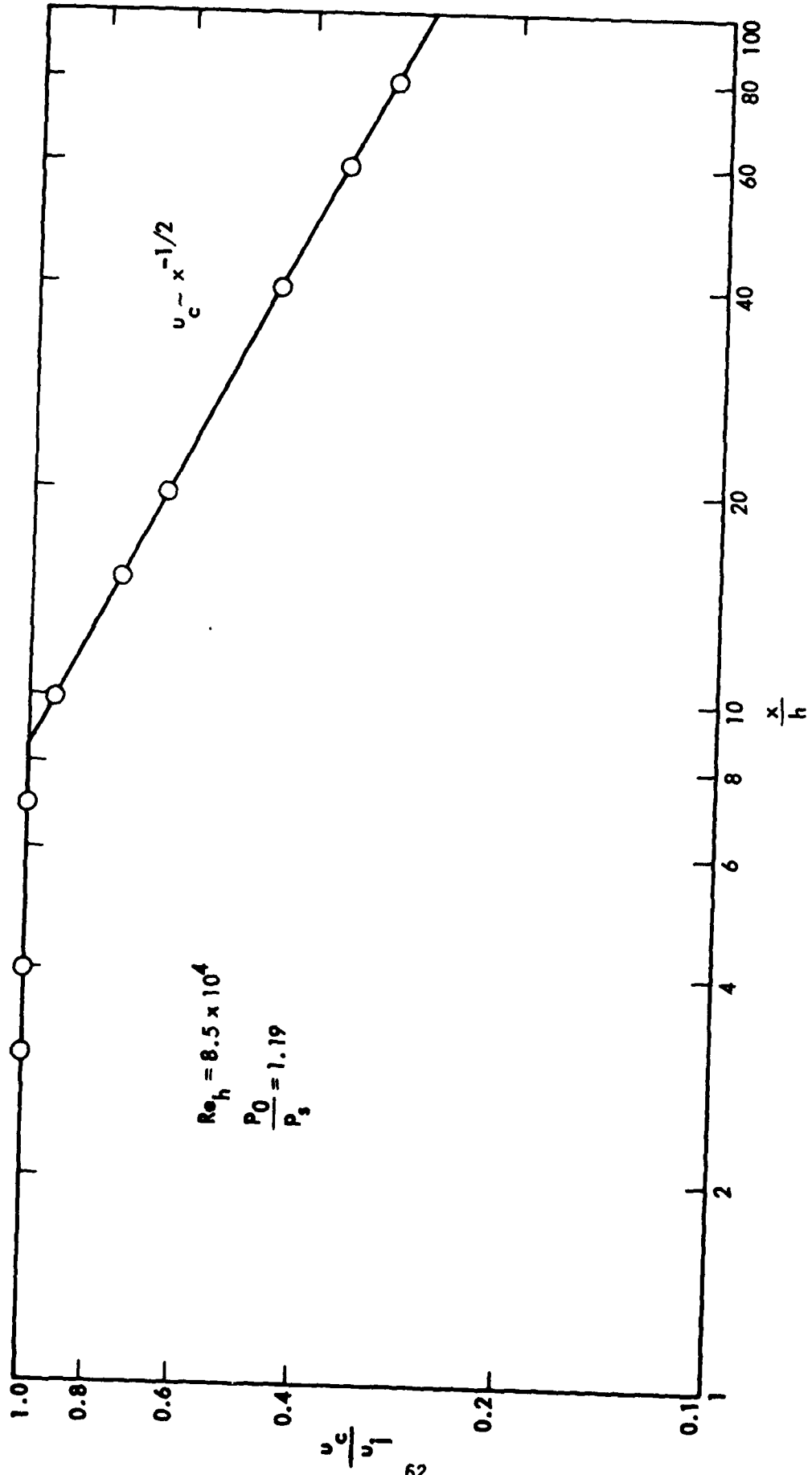


Figure 19. Center-line velocity decay with downstream distance.

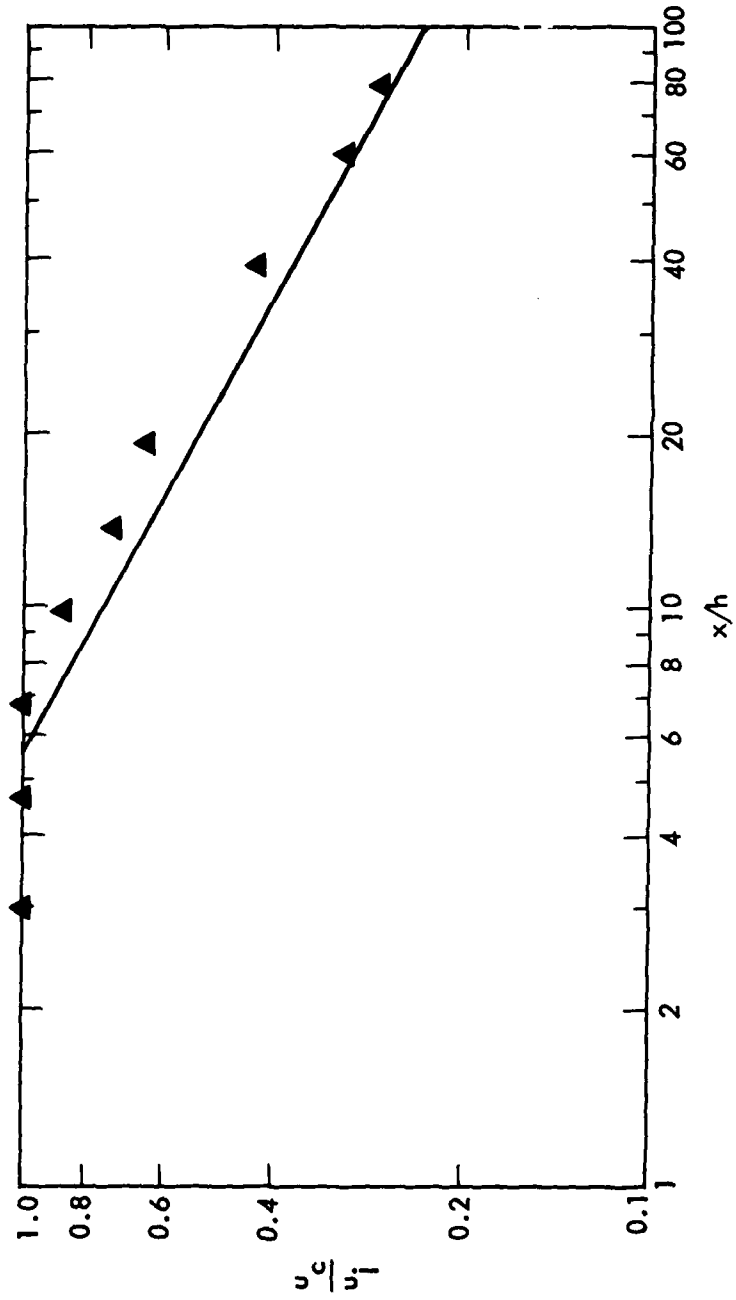


Figure 20. Center-line velocity decay comparison with collected data on reference 21. Δ present results, (-) reference 21.



Figure 21. Shadowgraph picture of ejector flow,  $M_{ex} = 0.5$

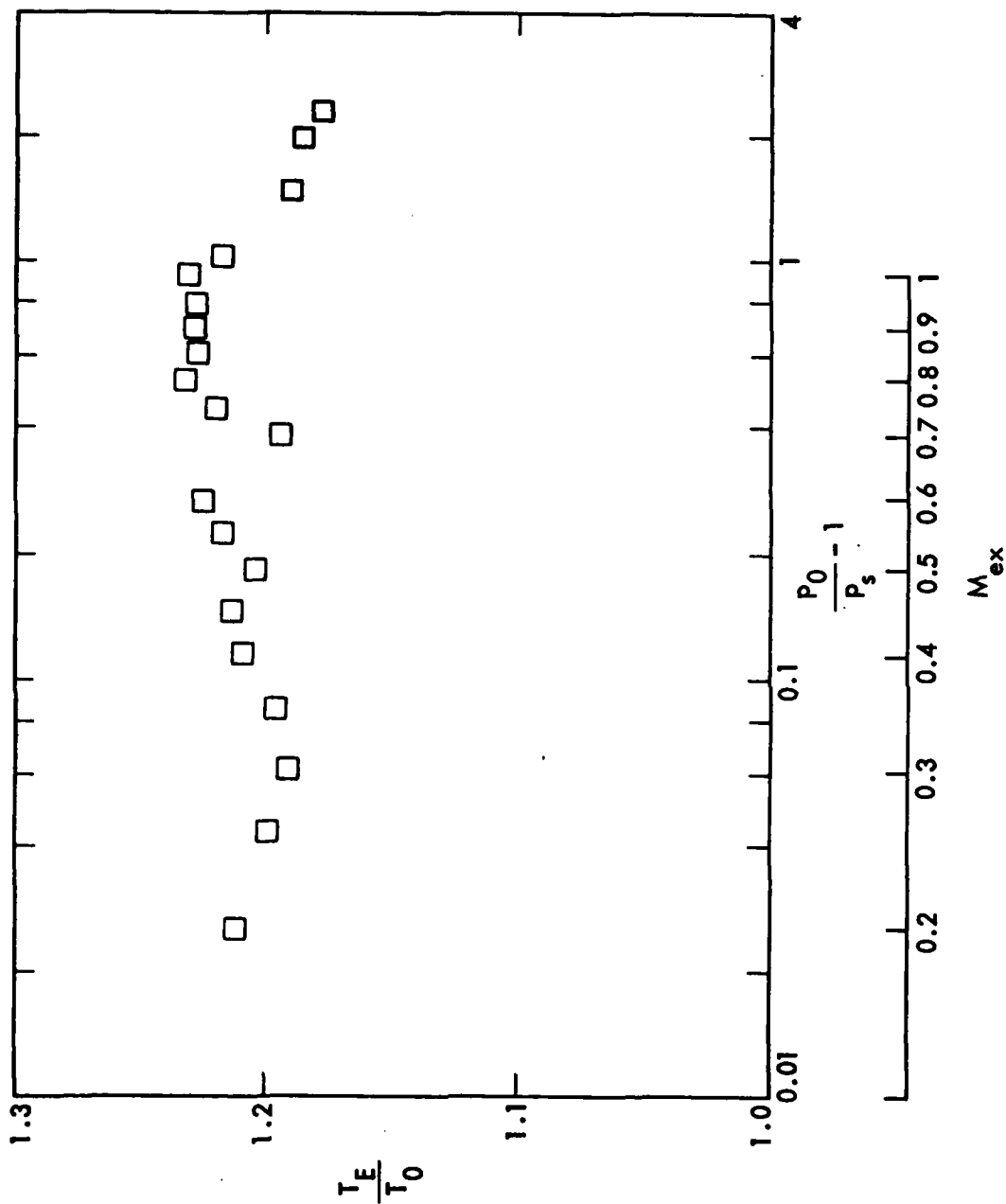


Figure 22. Ejector thrust augmentation ratio,  $T_e/T_0$ , as a function of primary jet pressure ratio.

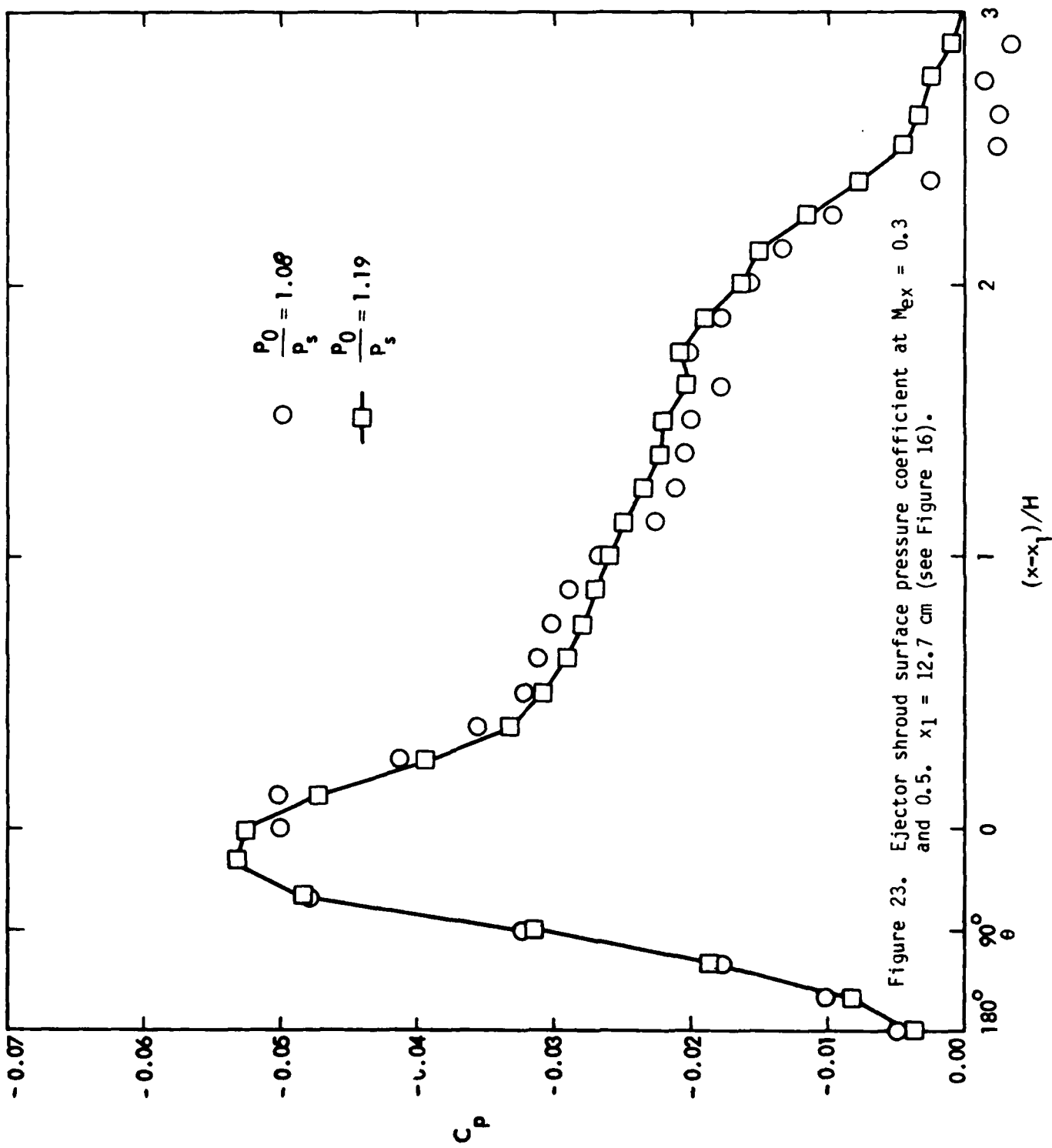


Figure 23. Ejector shroud surface pressure coefficient at  $M_{ex} = 0.3$  and 0.5.  $x_1 = 12.7$  cm (see Figure 16).

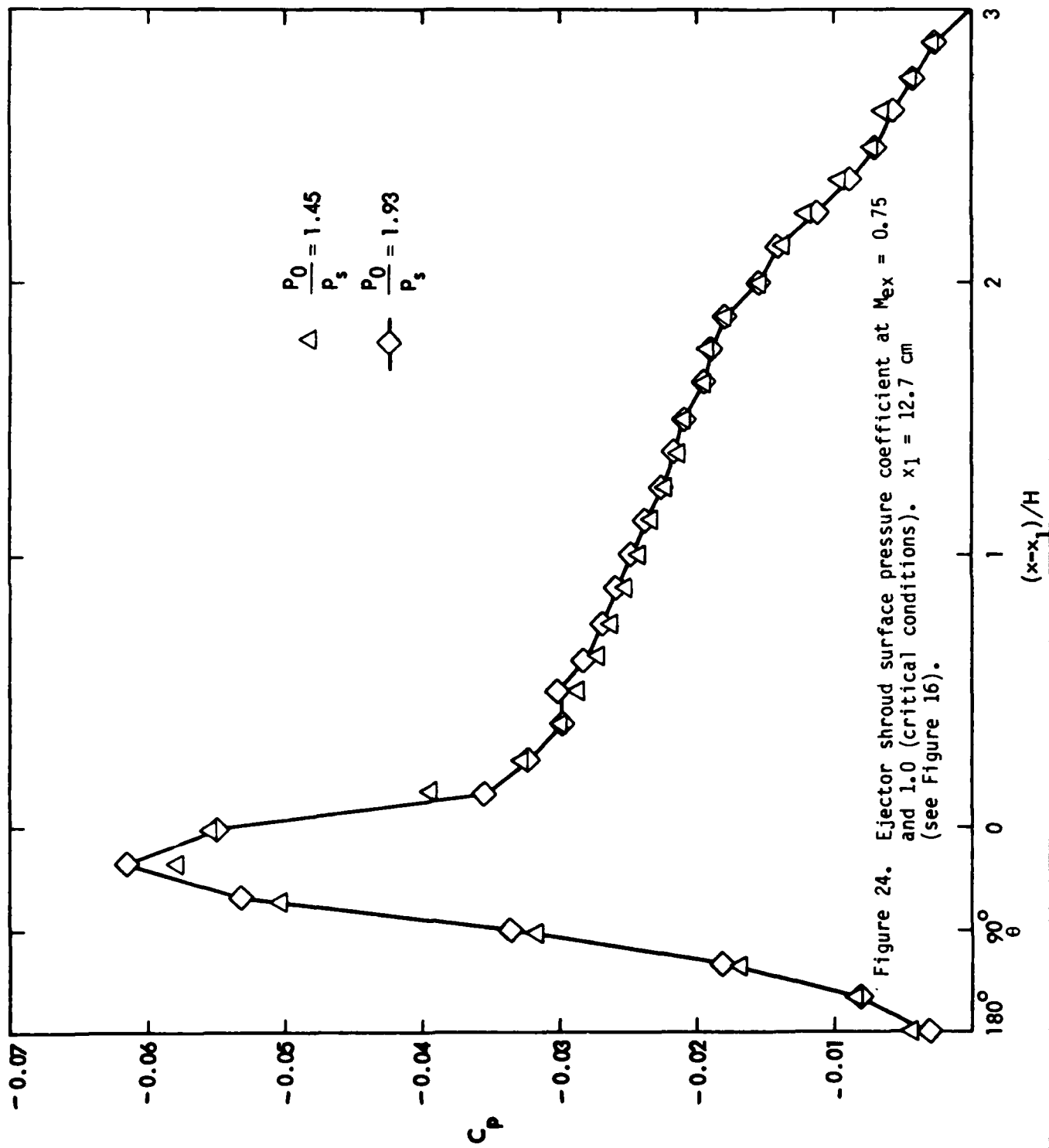


Figure 24. Ejector shroud surface pressure coefficient at  $M_{ex} = 0.75$  and 1.0 (critical conditions).  $x_1 = 12.7$  cm (see Figure 16).

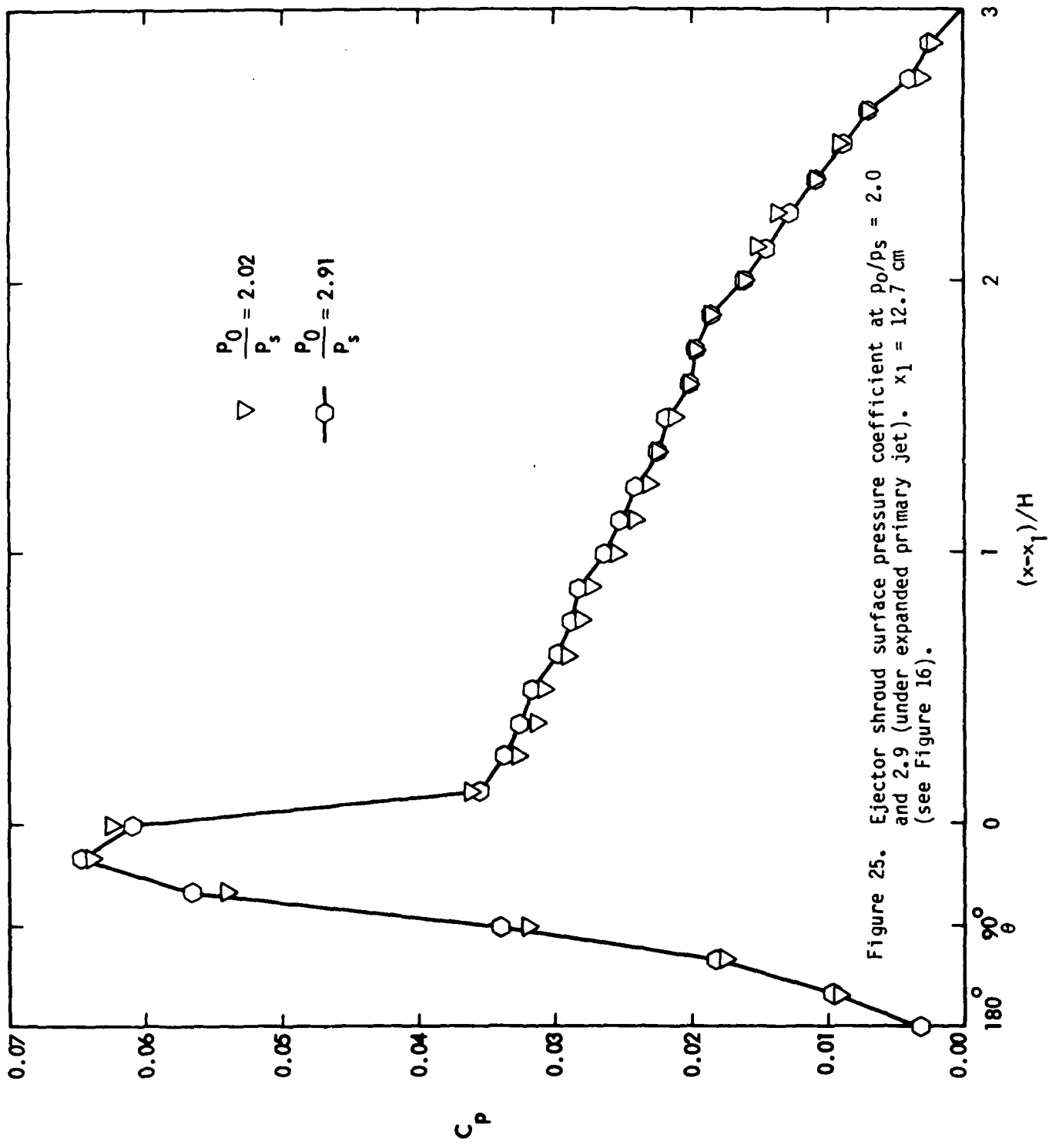


Figure 25. Ejector shroud surface pressure coefficient at  $p_0/p_s = 2.0$  and 2.9 (under expanded primary jet).  $x_1 = 12.7$  cm (see Figure 16).

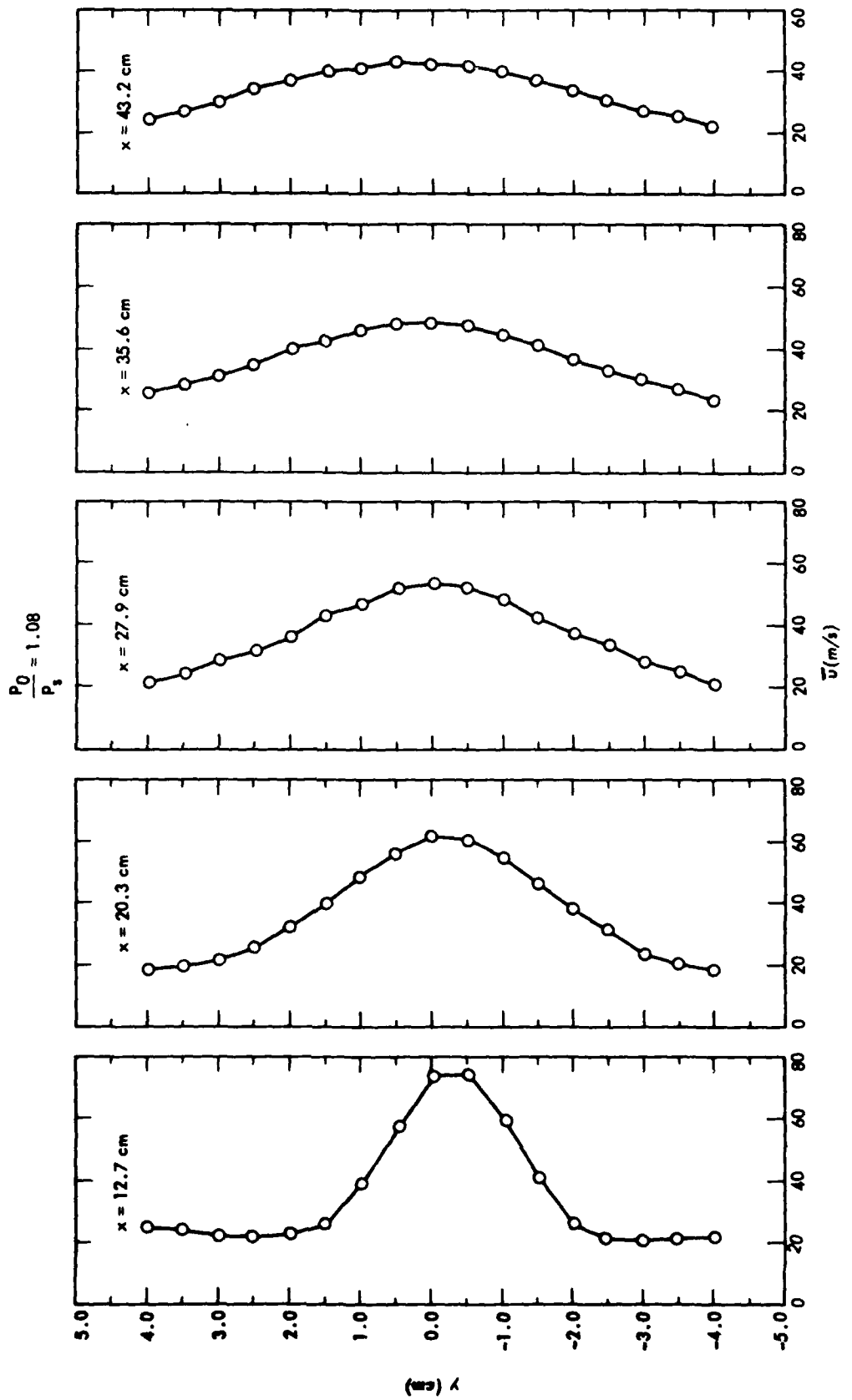


Figure 26. Mean  $\bar{u}$  velocity profiles inside the ejector shroud at  $M_{ex} = 0.3$ .

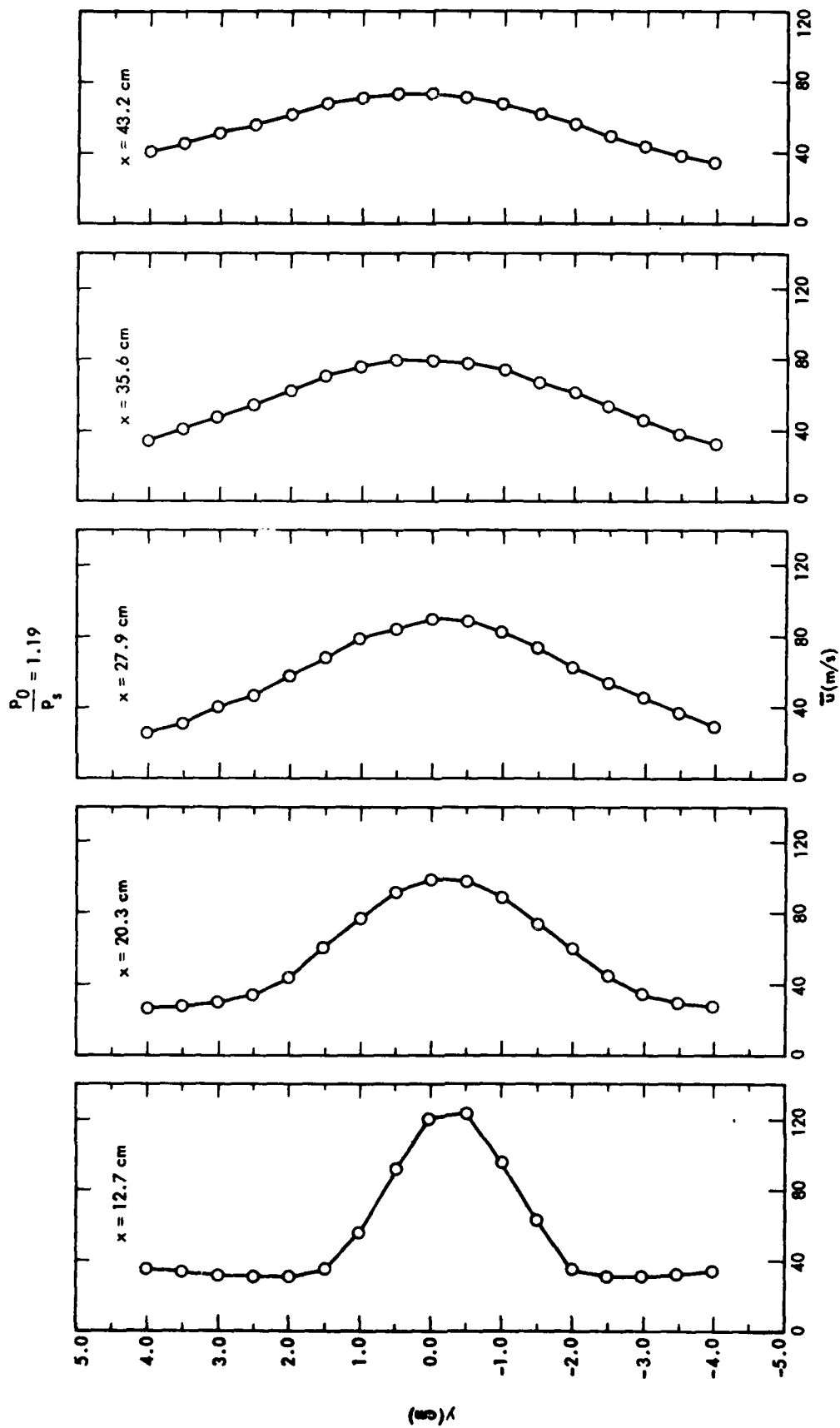


Figure 27. Mean  $\bar{u}$  velocity profiles inside the ejector shroud at  $M_{ex} = 0.5$ .

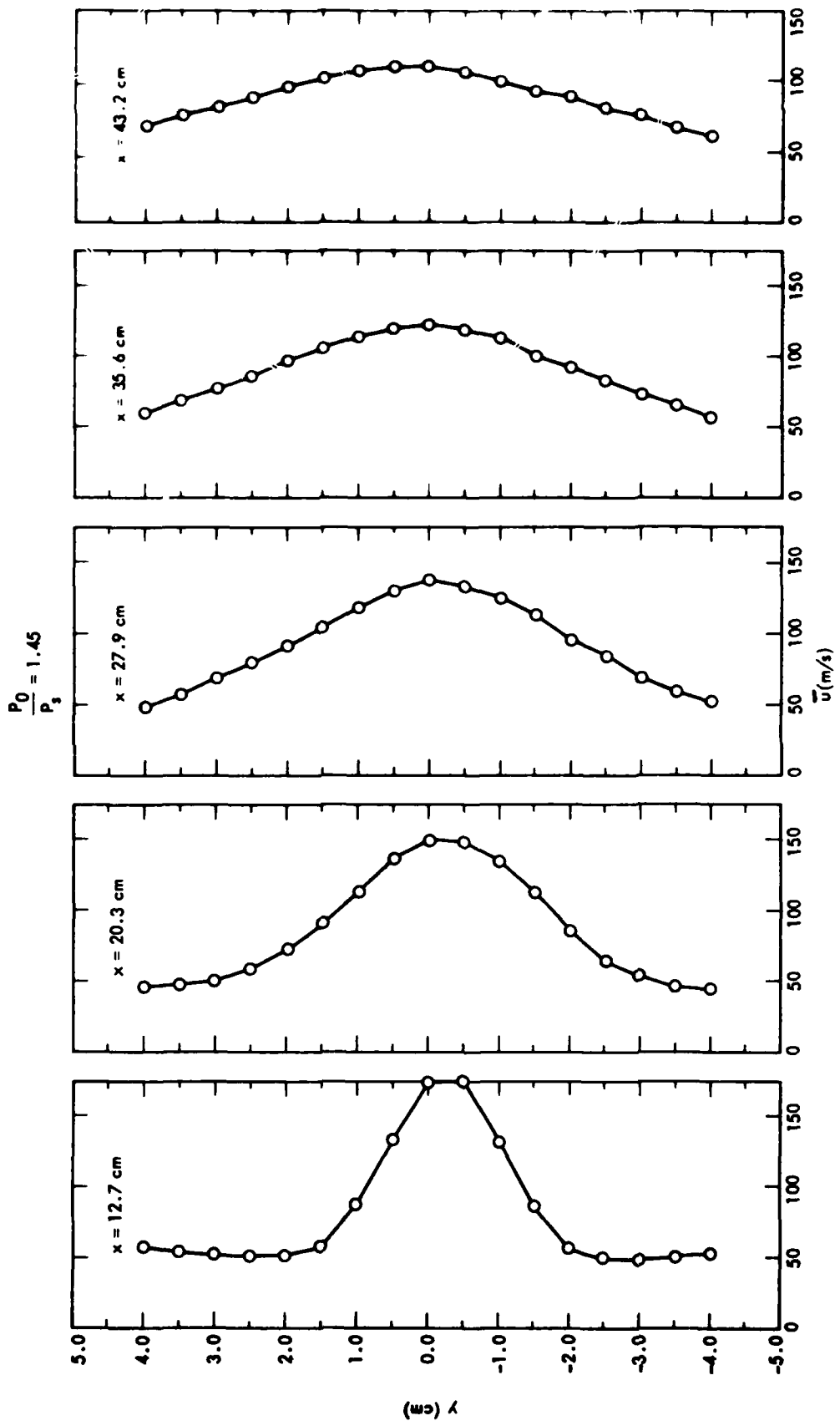


Figure 28. Mean  $\bar{u}$  velocity profiles inside the ejector shroud at  $M_{ex} = 0.75$ .

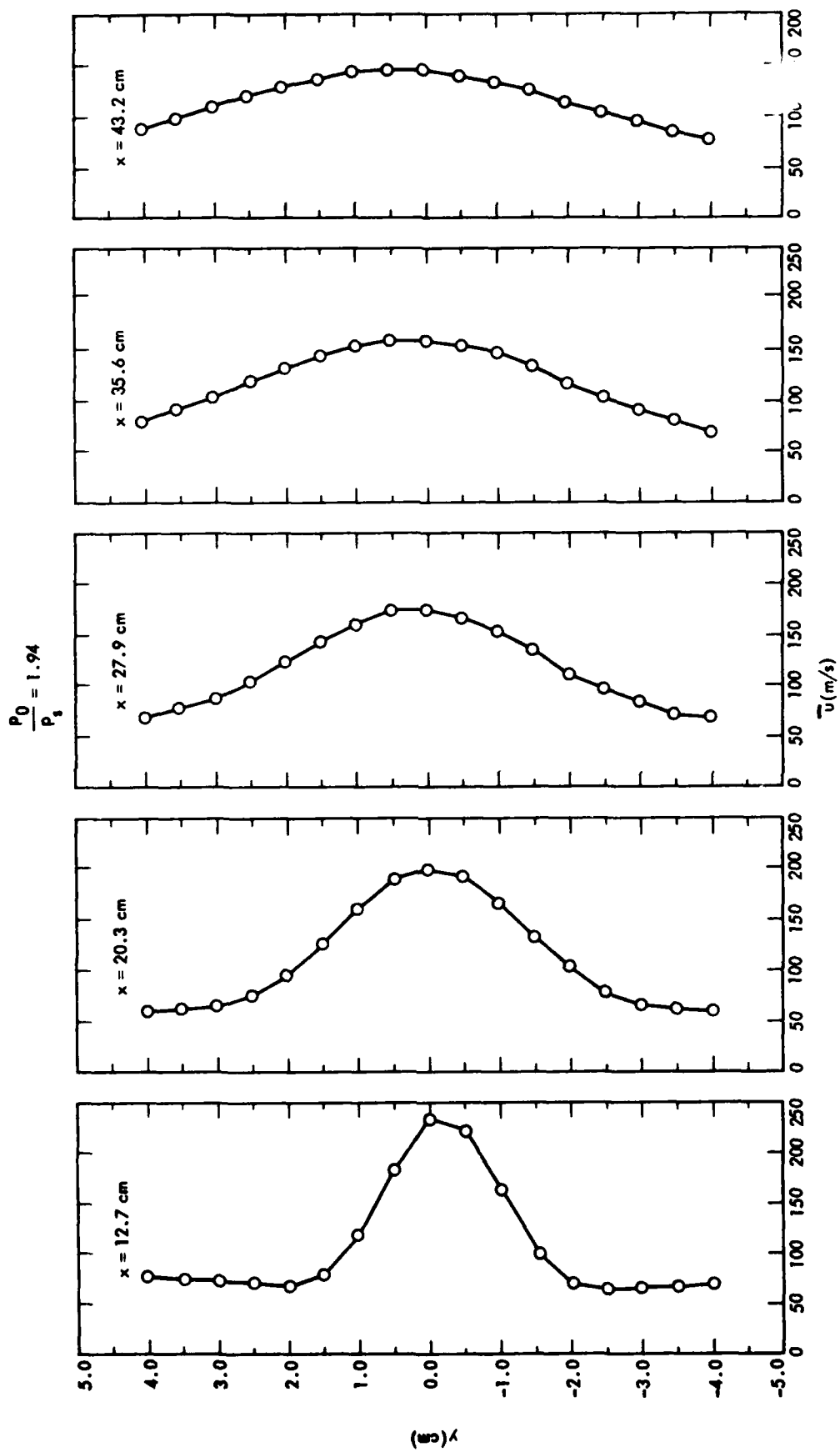


Figure 29. Mean  $\bar{u}$  velocity profiles inside the ejector shroud at  $M_{ex} = 1.0$  (critical conditions).

$$\frac{P_0}{P_s} = 1.19$$

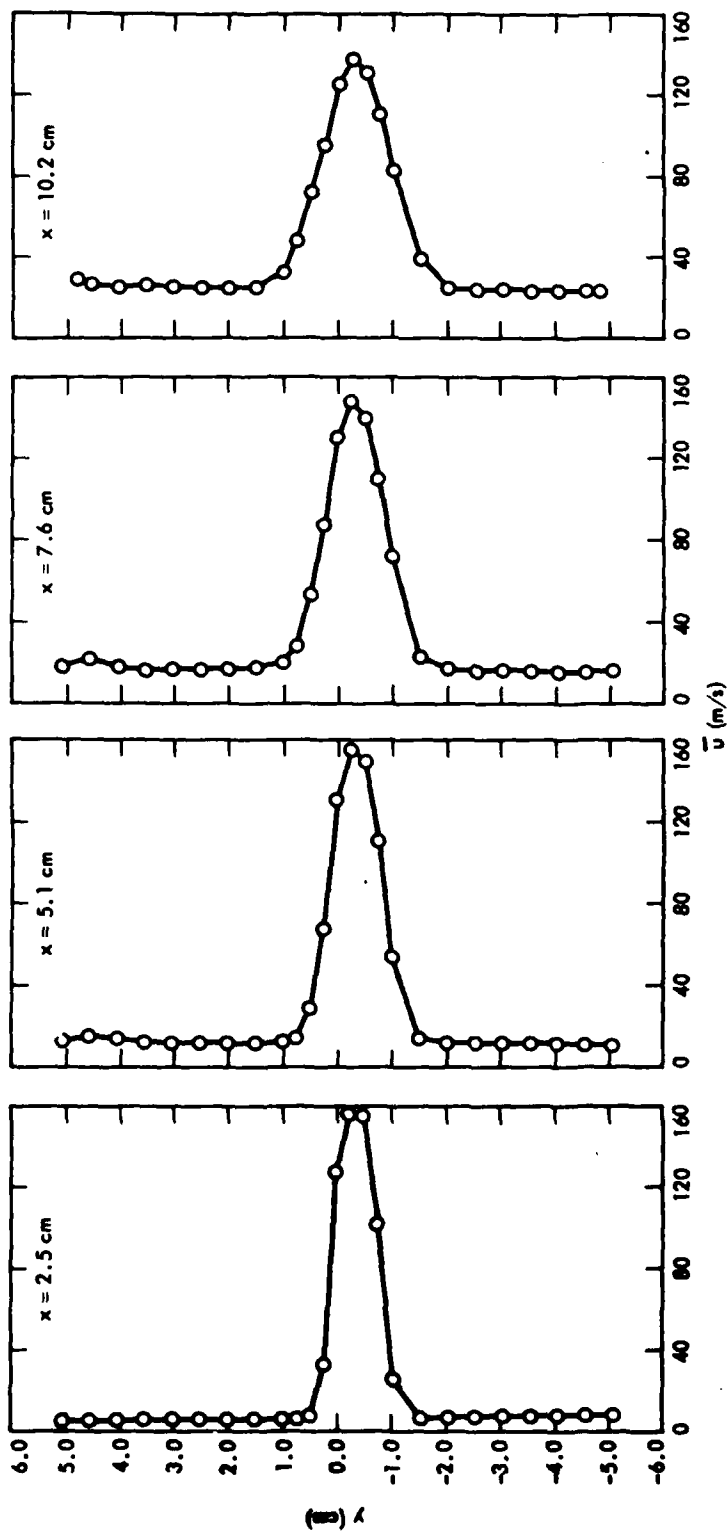


Figure 30. Mean  $\bar{u}$  velocity profiles entrance region at  $M_{ex} = 0.5$ .

$$\frac{P_0}{P_s} = 1.19$$

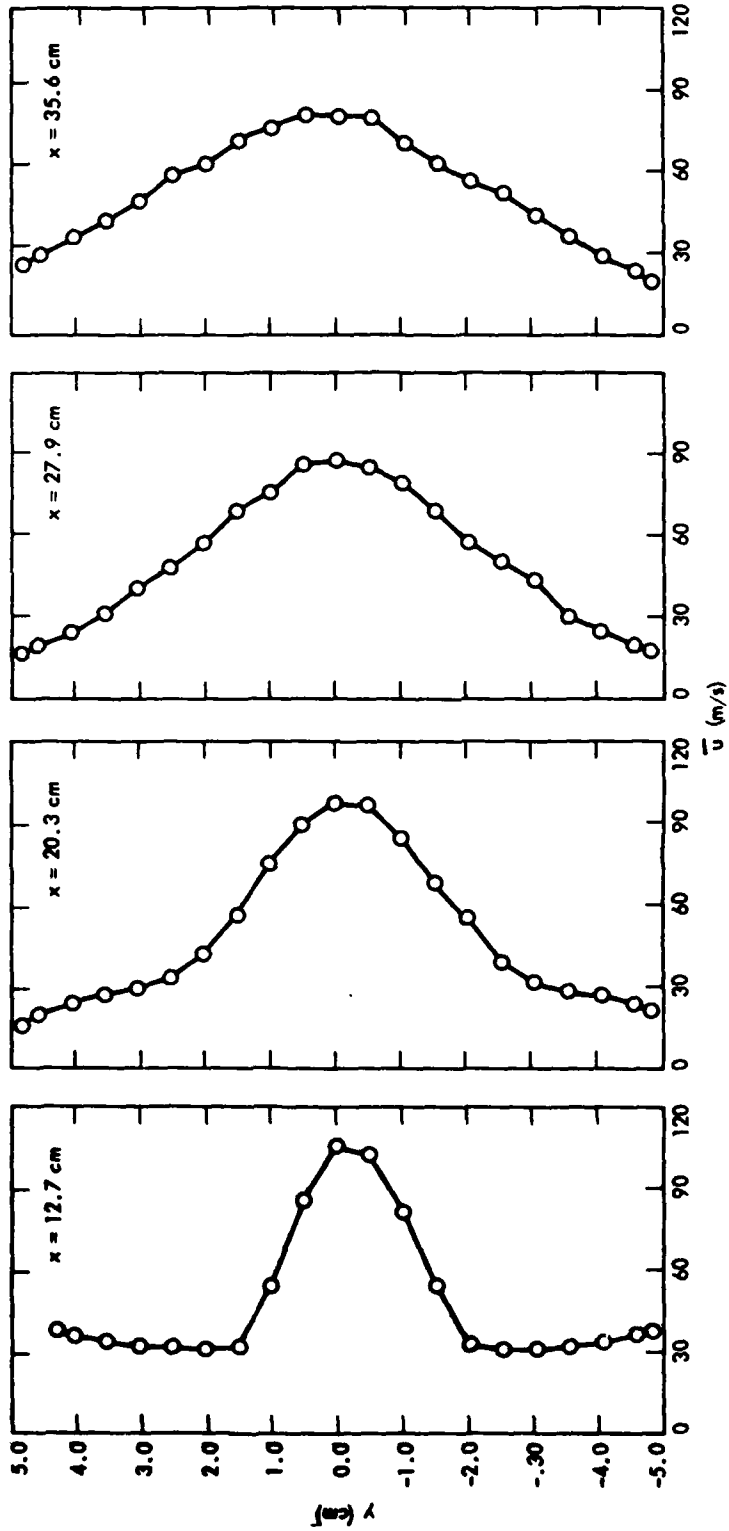


Figure 31. Mean  $\bar{u}$  velocity profiles inside the ejector shroud at  $M_{ex} = 0.5$ . Single component LDV configuration.

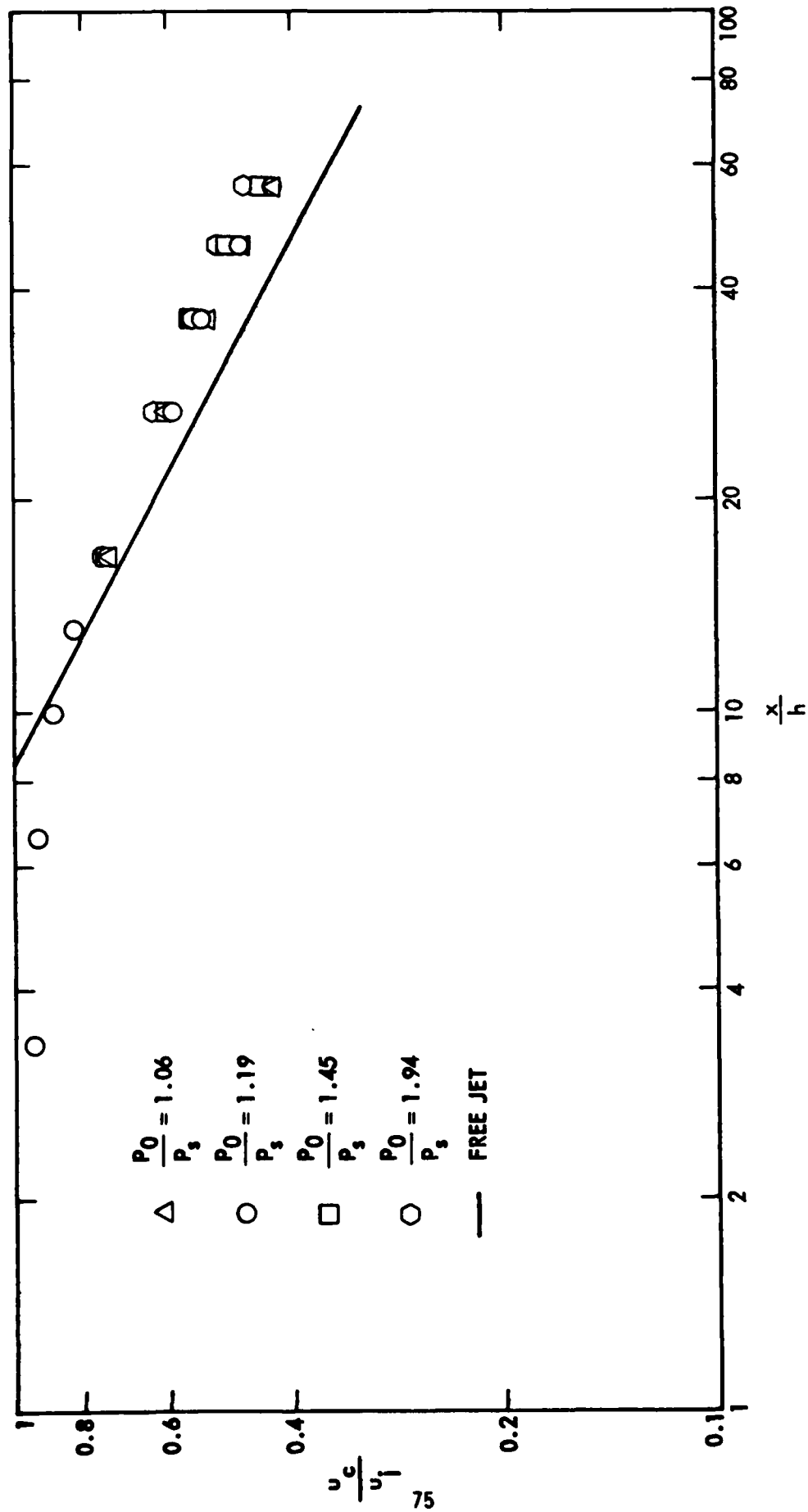


Figure 32. Ejector centerline velocity decay.

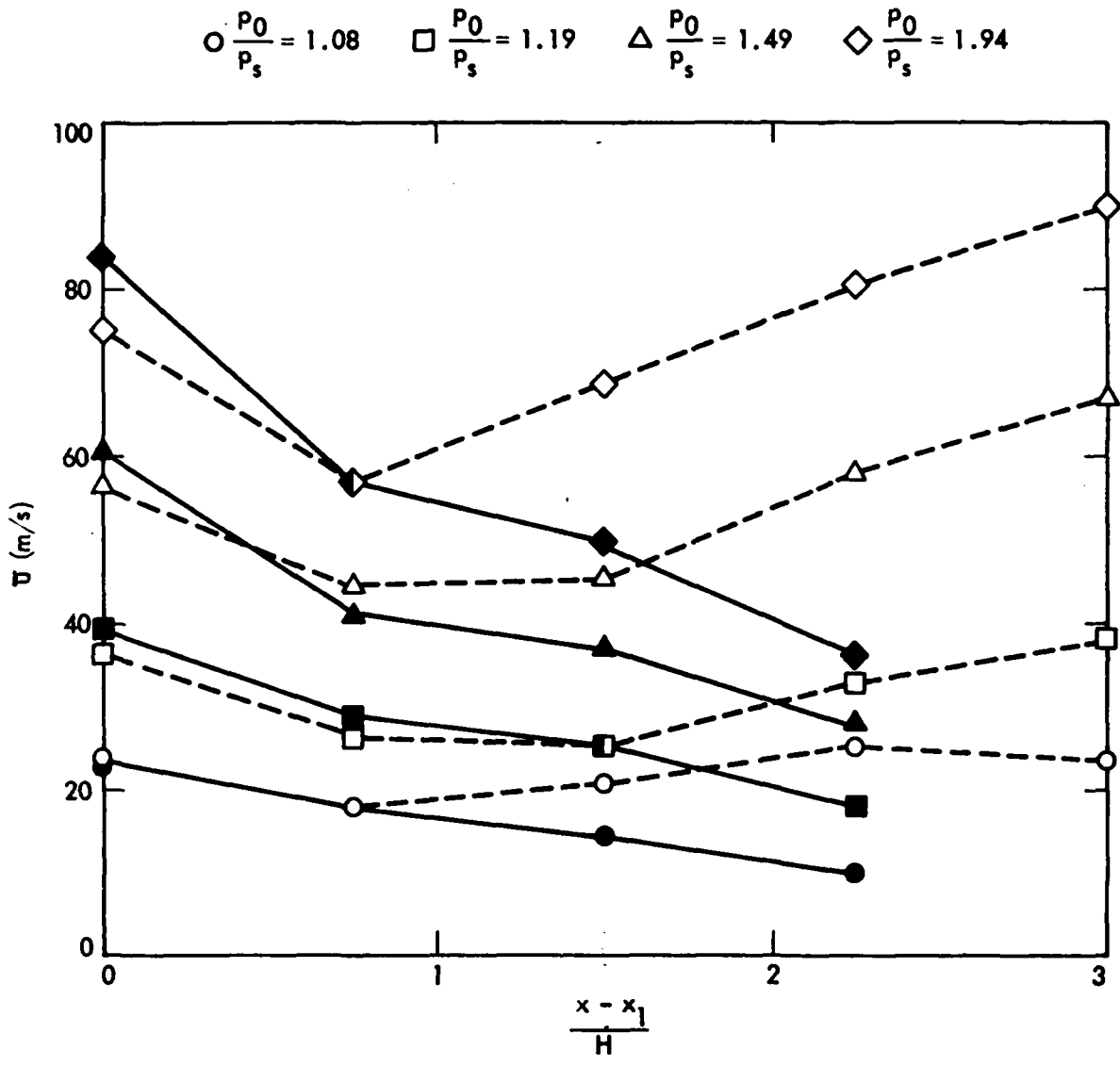


Figure 33. Downstream variation of the velocity at  $y = 4.0$  cm. Open symbols measured velocity. Closed symbols  $\bar{u} = U_j \sqrt{-C_p}$ .  $x_1 = 12.7$  cm (see Figure 16).

$$\frac{P_0}{P_s} = 1.06$$

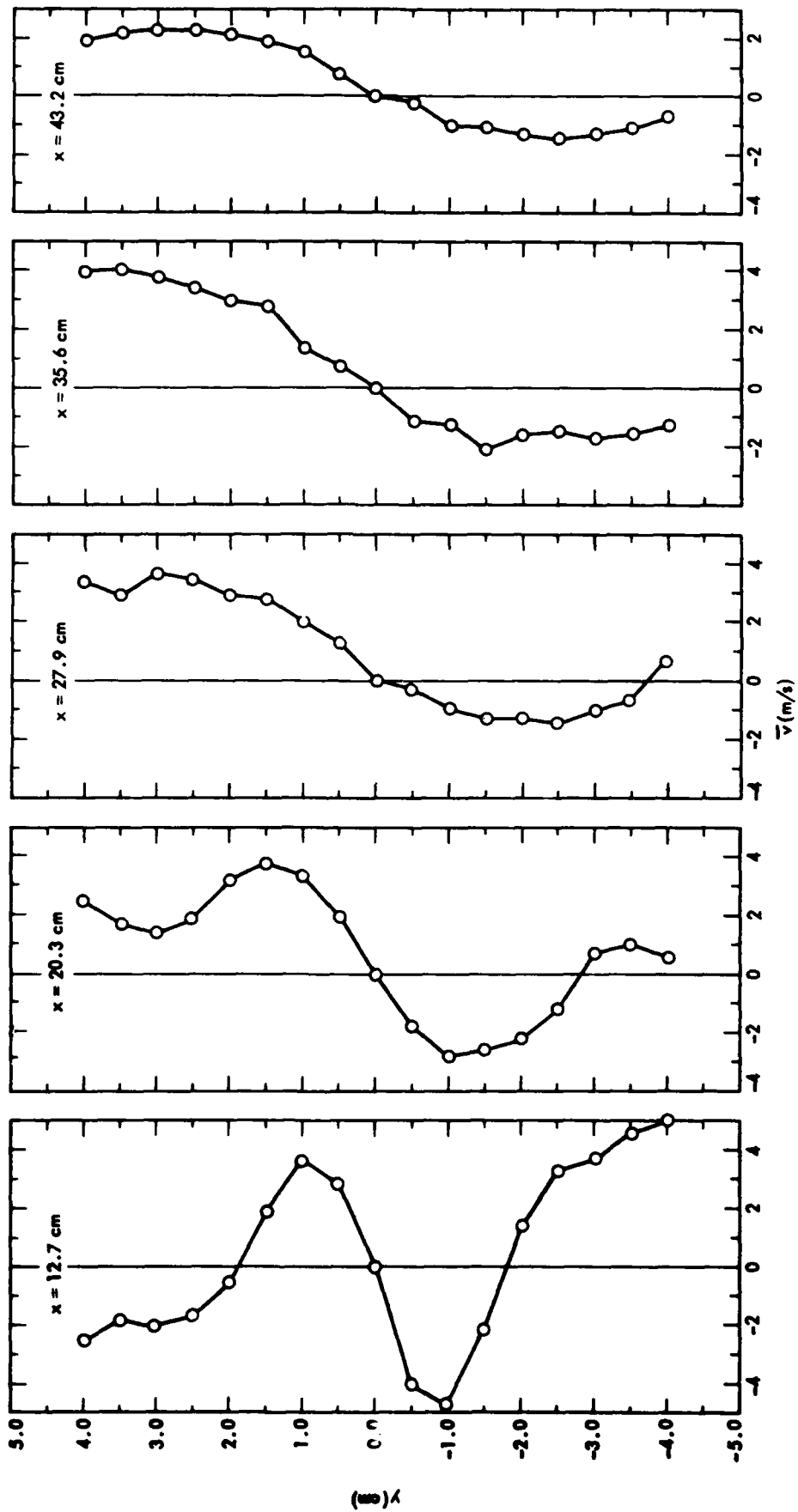


Figure 34. Mean  $\bar{v}$  velocity profiles inside the ejector shroud at  $M_{ex} = 0.3$ .

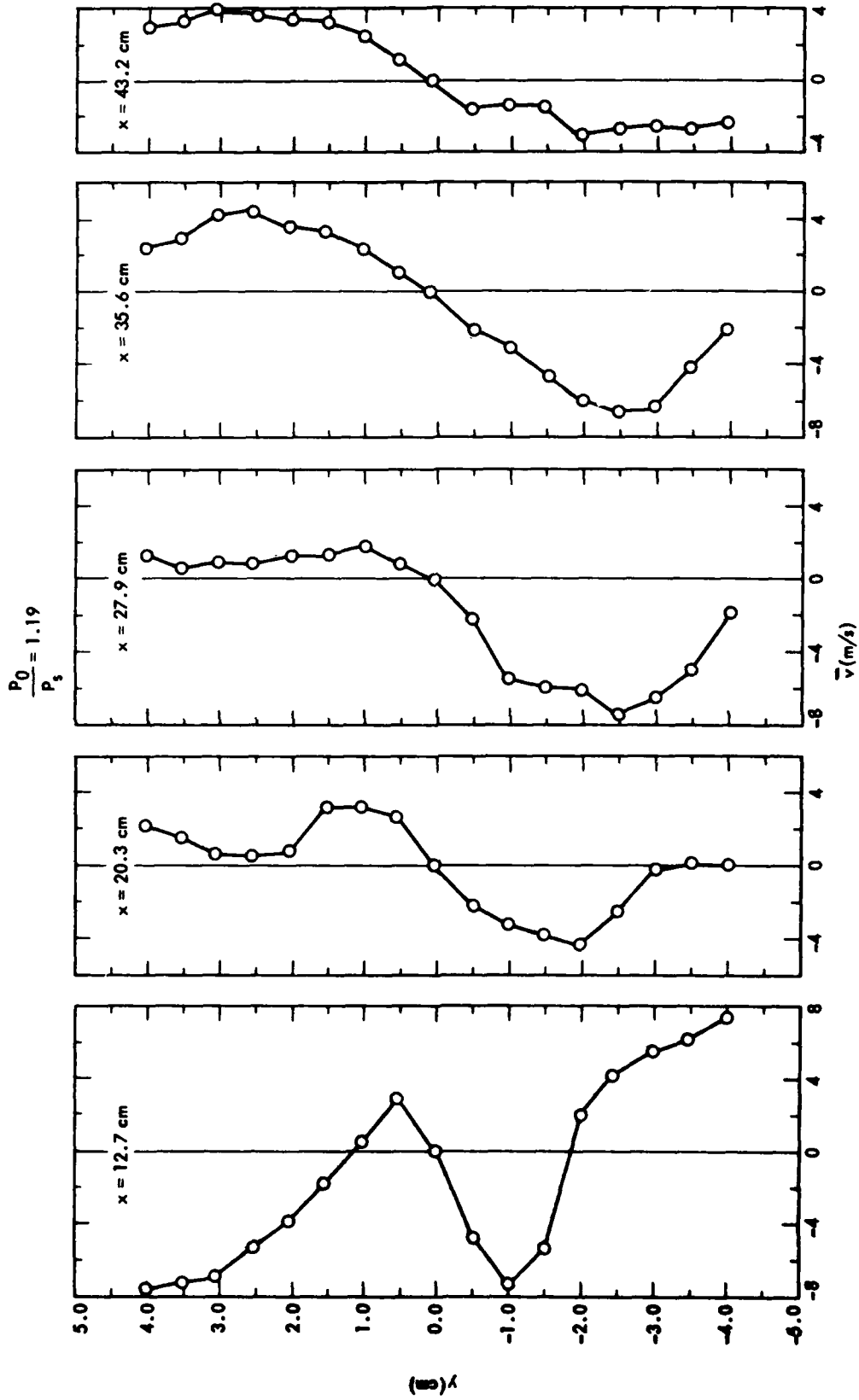


Figure 35. Mean  $\bar{v}$  velocity profiles inside the ejector shroud at  $M_{ex} = 0.5$ .

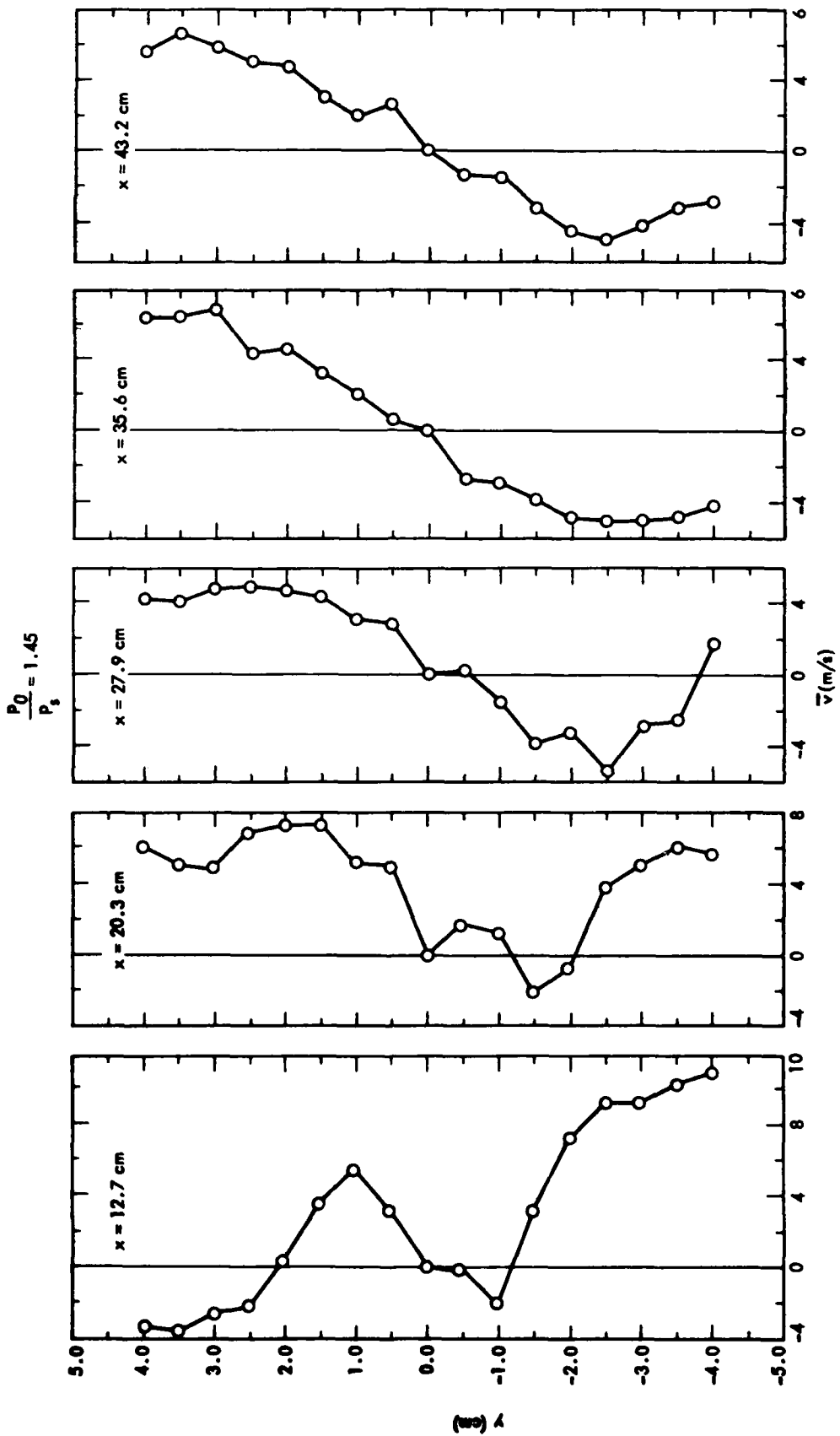


Figure 36. Mean  $\bar{v}$  velocity profiles inside the ejector shroud at  $M_{ex} = 0.75$ .

$$\frac{P_0}{P_s} = 1.94$$

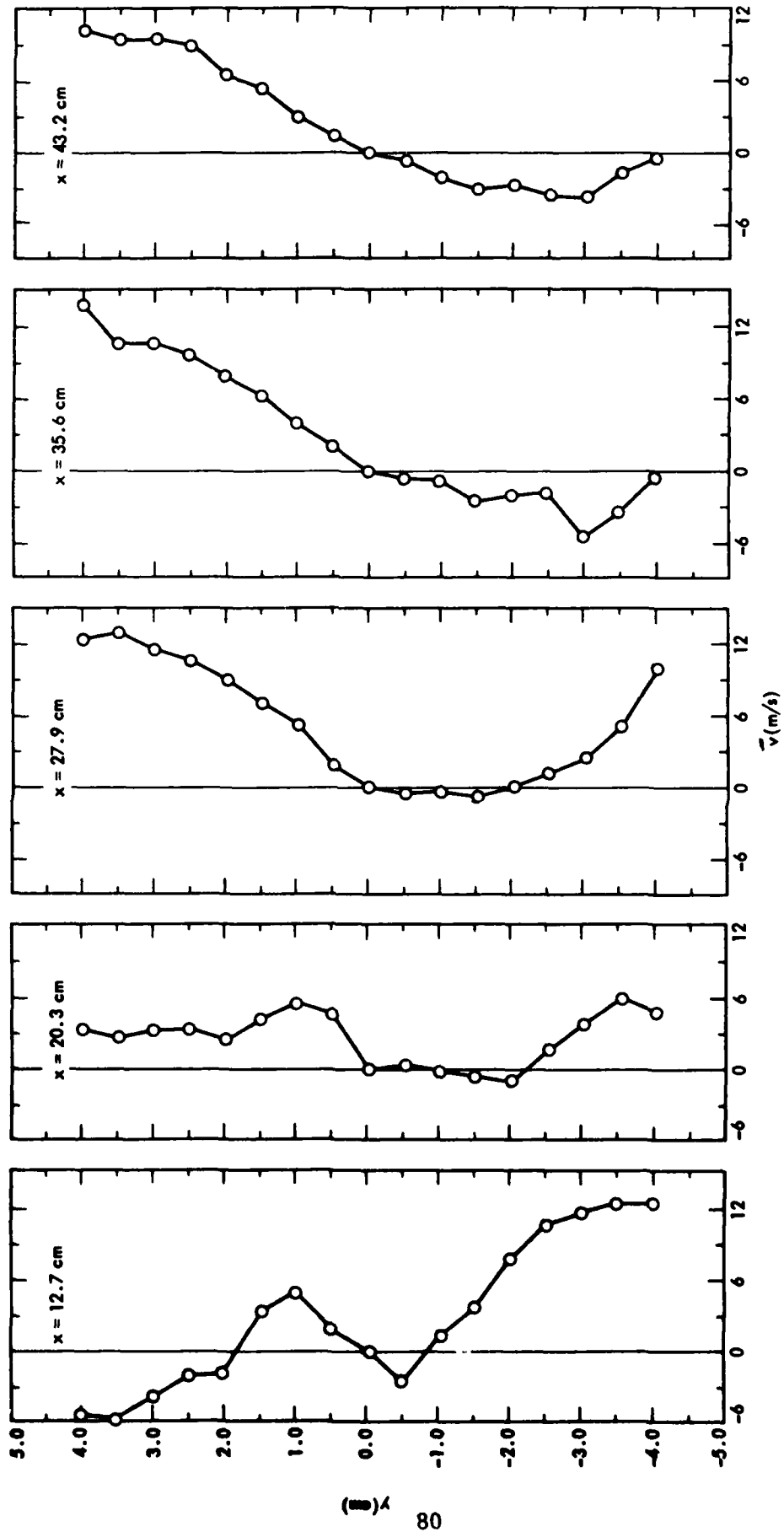


Figure 37. Mean  $\bar{v}$  velocity profiles inside the ejector shroud at  $M_{ex} = 1.0$  (critical conditions).

$$\frac{P_0}{P_3} = 1.19$$

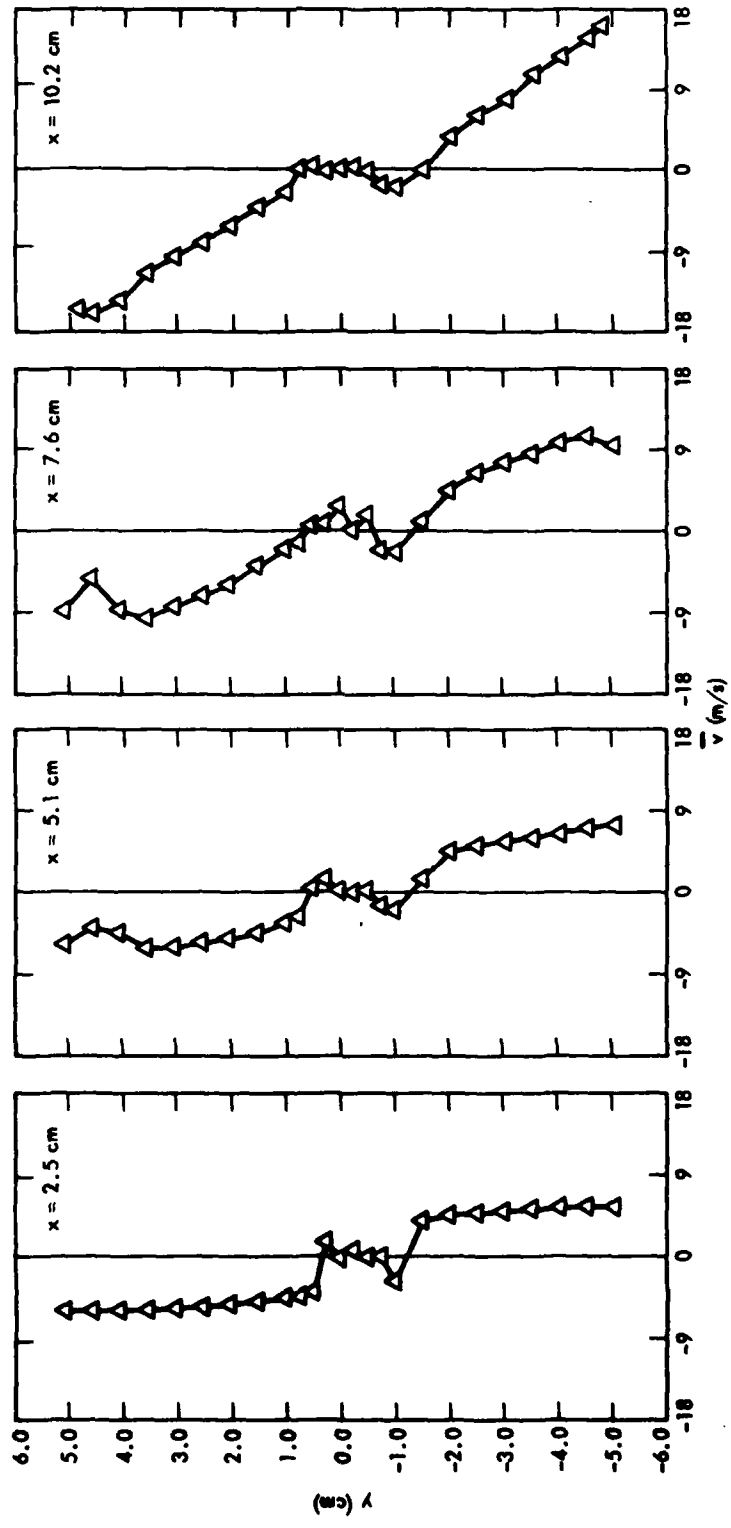


Figure 38. Mean  $\bar{v}$  velocity profiles entrance region at  $M_{ex} = 0.5$ .

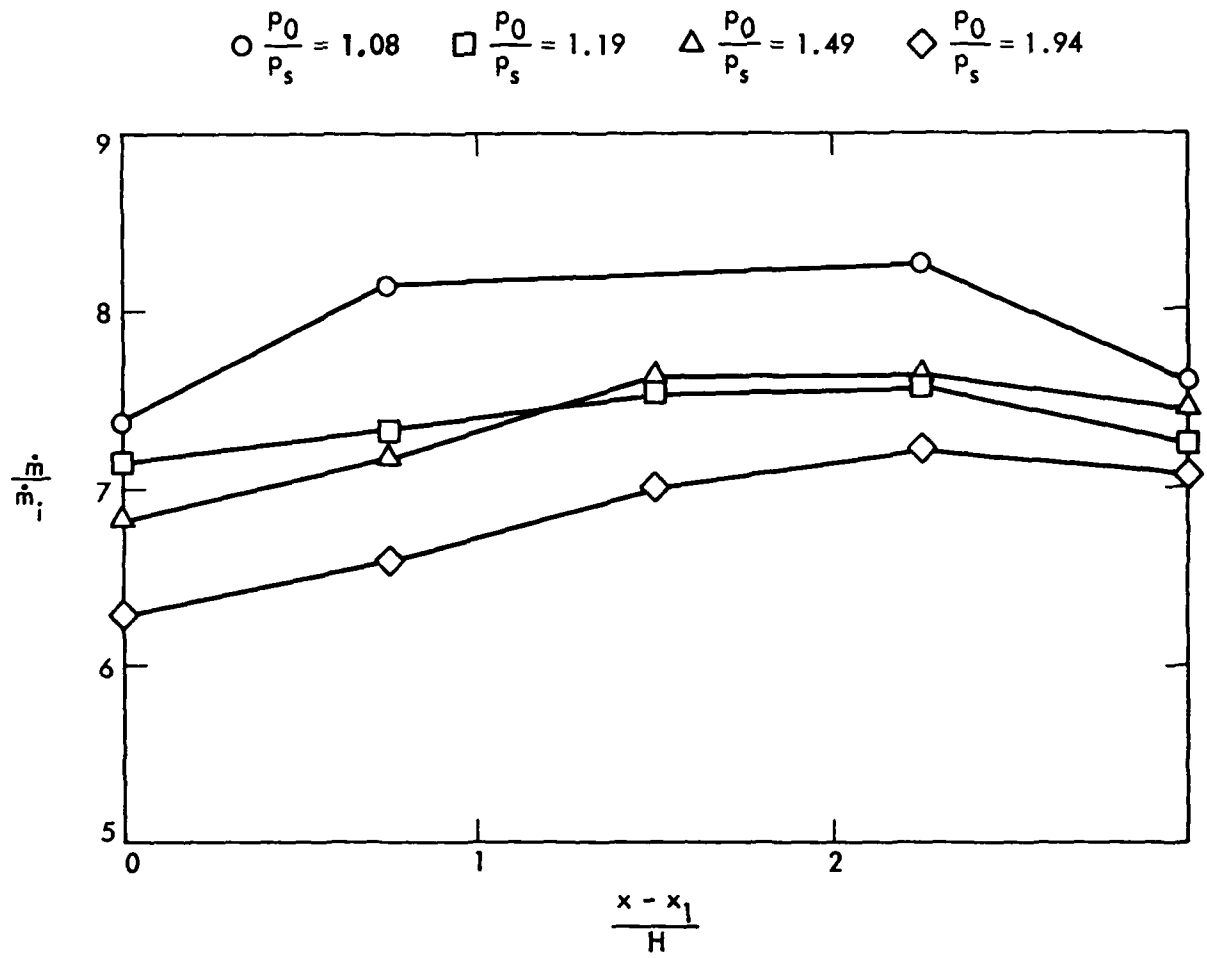


Figure 39. Downstream variation of mass flow ratios.  $x_1 = 12.7$  cm (see Figure 16).

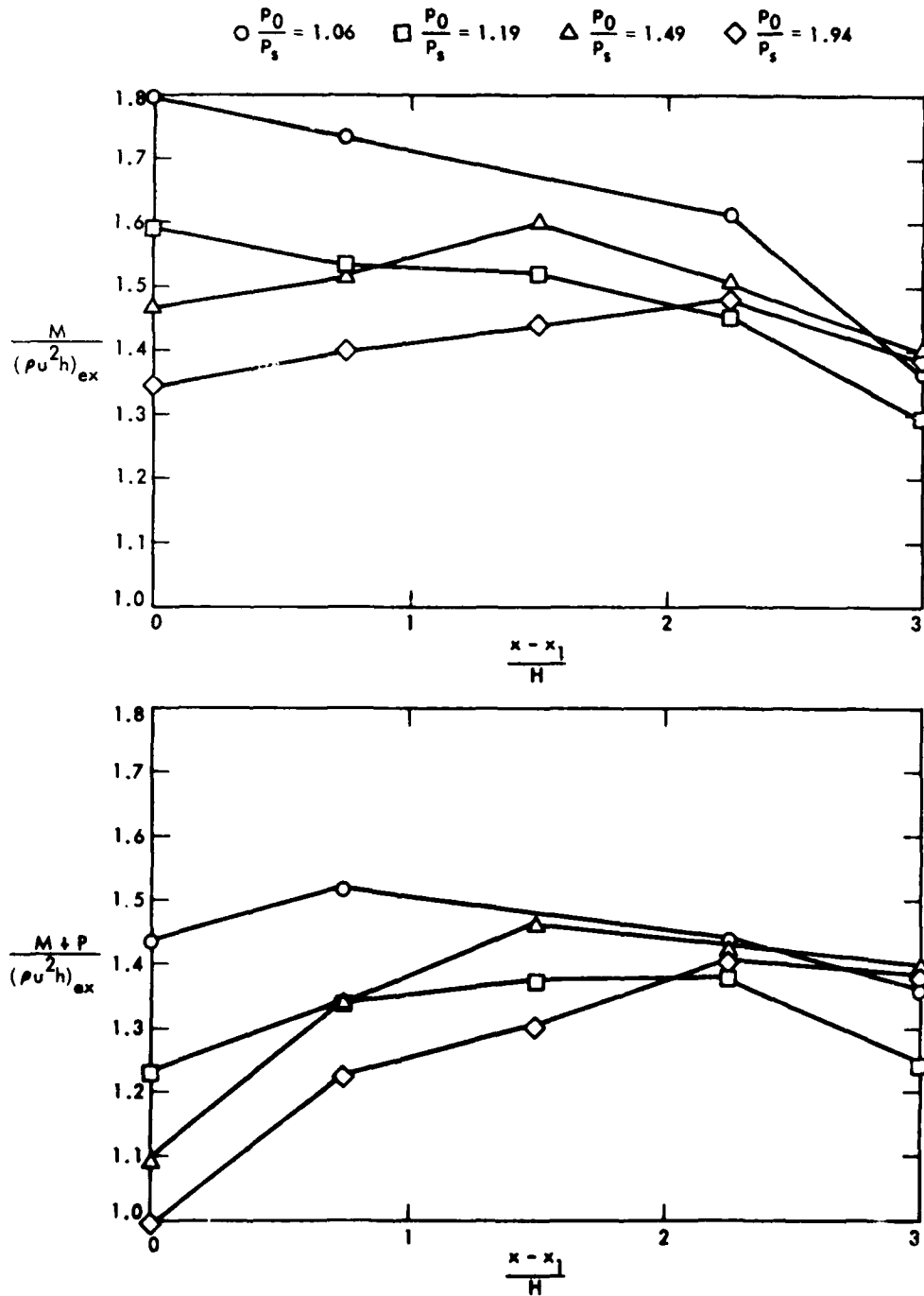


Figure 40. Momentum balance calculation.  $x_1 = 12.7$  cm (see Figure 16).  
 (a) Downstream evolution of the momentum flux.  
 (b) Momentum conservation within the ejector shroud.

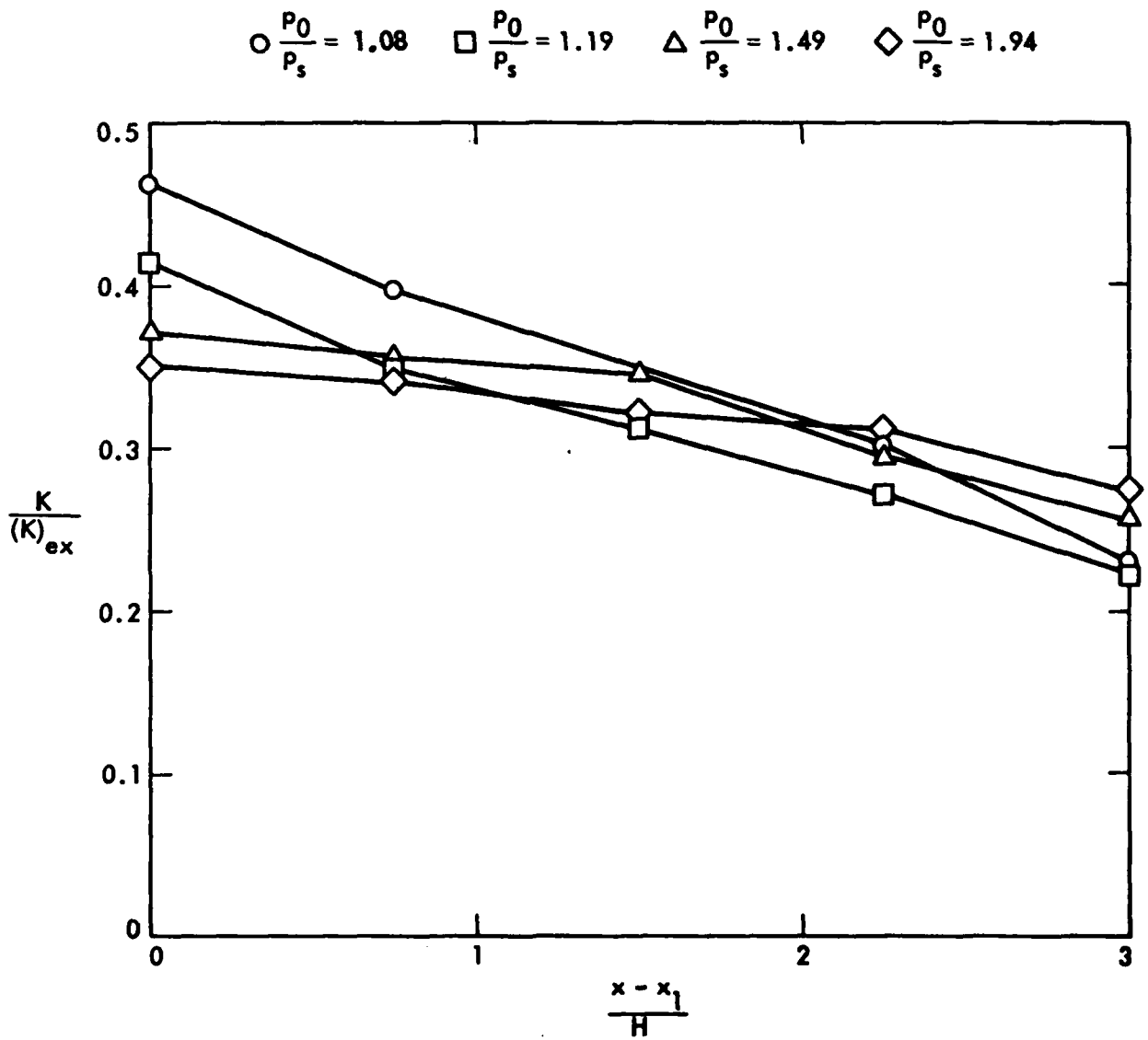


Figure 41. Mean kinetic energy flux evolution within the ejector shroud.  $x_1 = 12.7$  cm (see Figure 16).

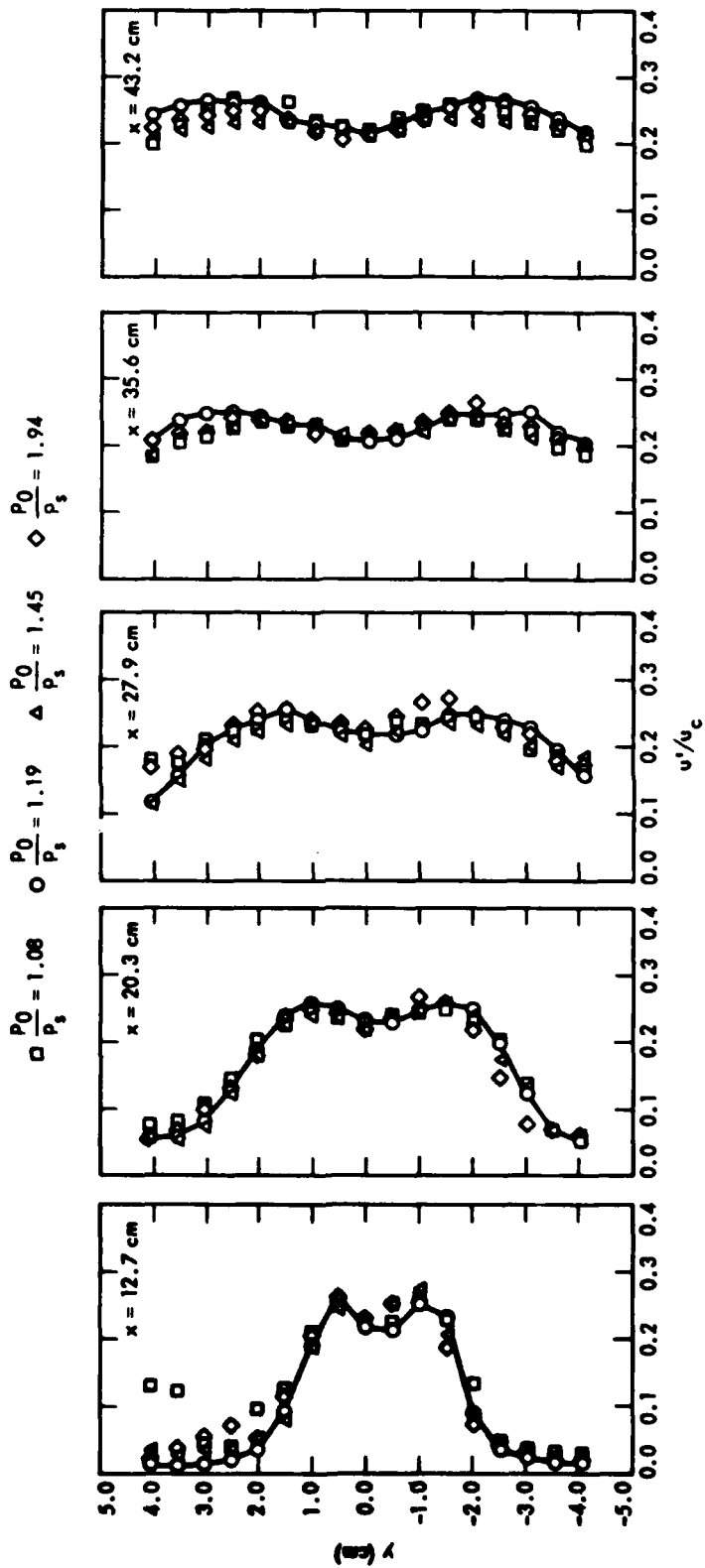


Figure 42. Normalized turbulent intensity profiles inside the ejector shroud,  $u'$  component.

$$\frac{P_0}{P_s} = 1.19$$

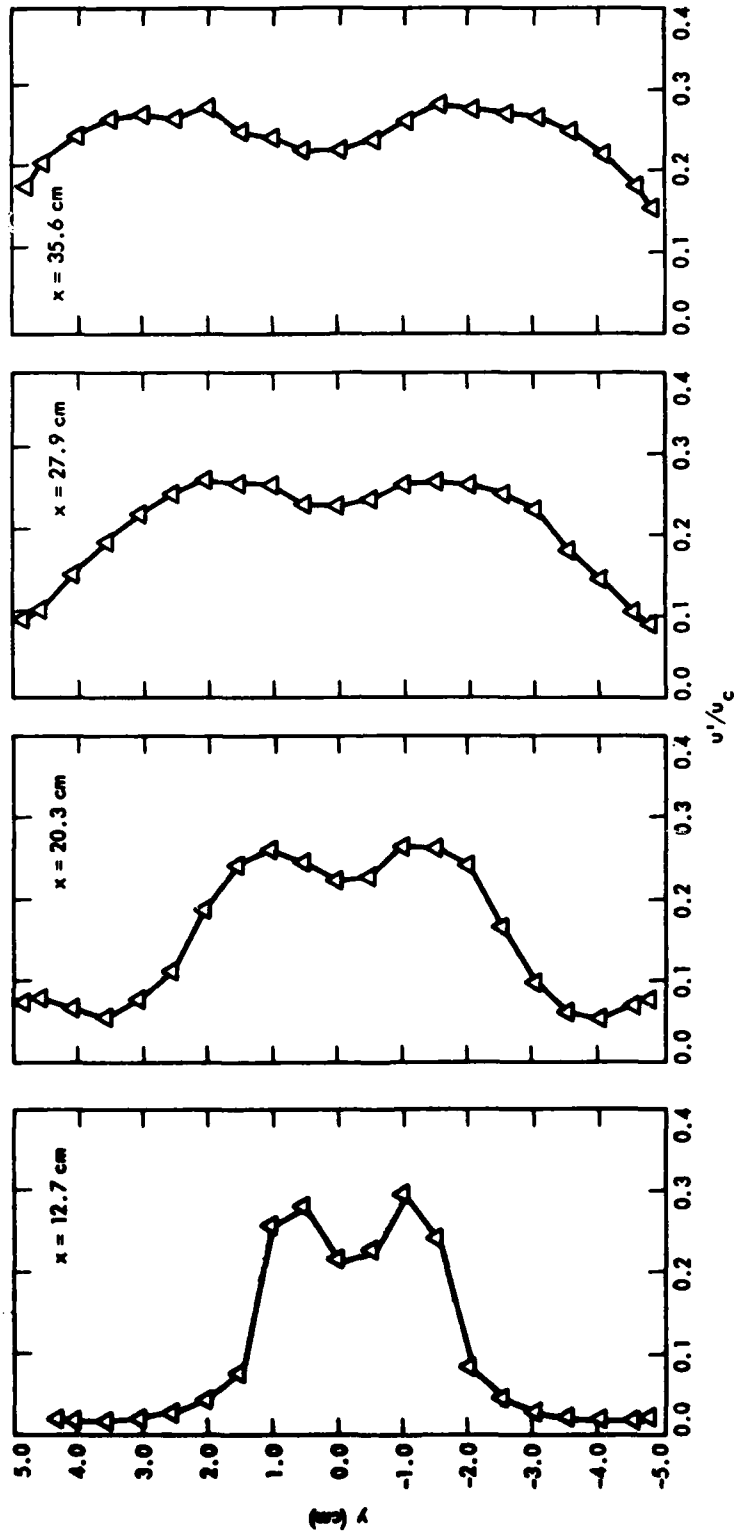


Figure 43. Normalized turbulent intensity profiles inside the ejector shroud. Single component LDV configuration.

$\square \frac{P_0}{P_s} = 1.08$     $\circ \frac{P_0}{P_s} = 1.19$     $\triangle \frac{P_0}{P_s} = 1.45$     $\diamond \frac{P_0}{P_s} = 1.94$

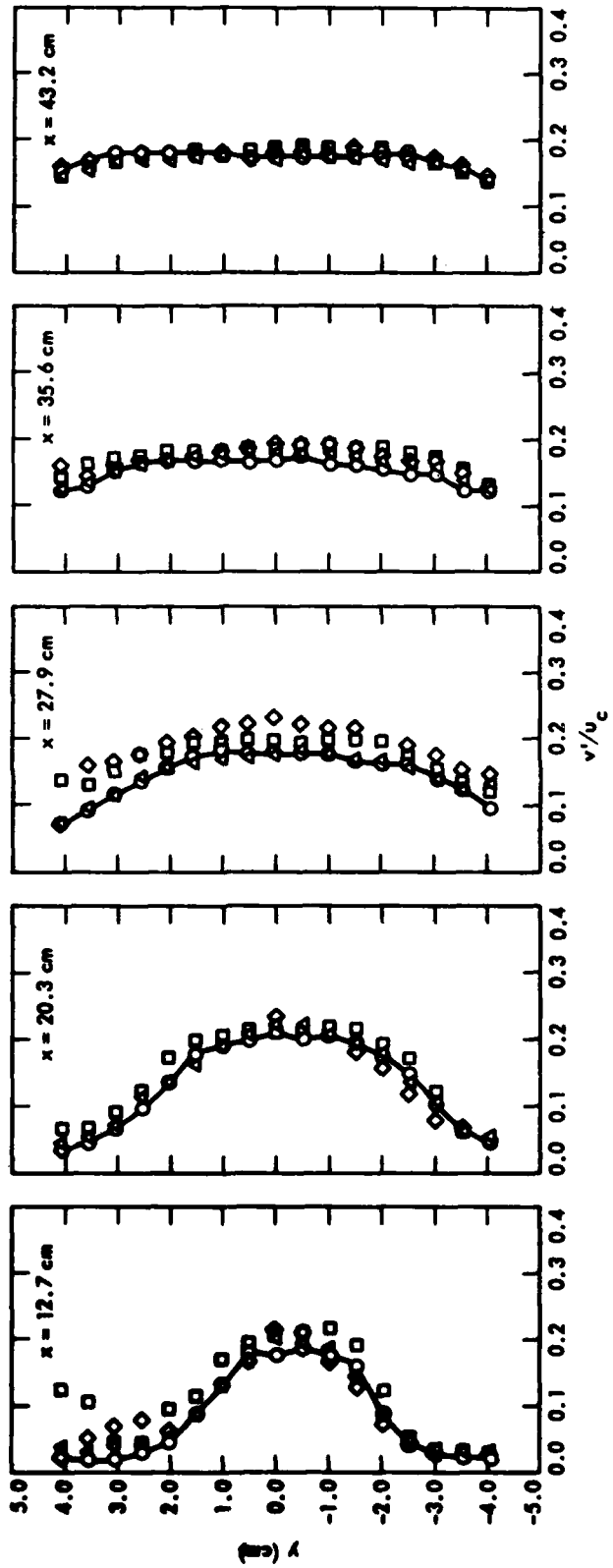


Figure 44. Normalized turbulent intensity profiles inside the ejector shroud,  $v'$  component.

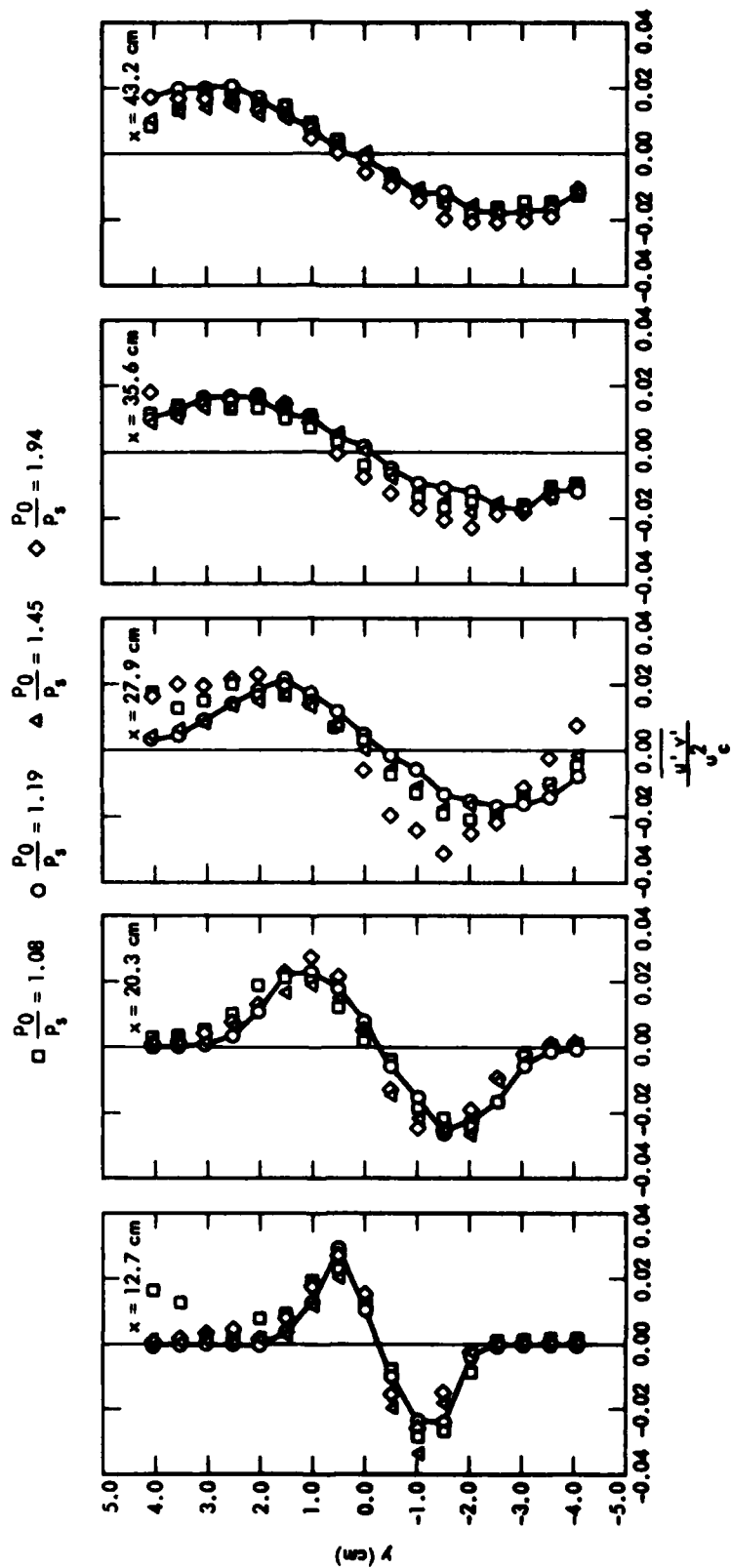


Figure 45. Normalized  $\overline{u'v'}$  velocity correlation inside the ejector shroud.

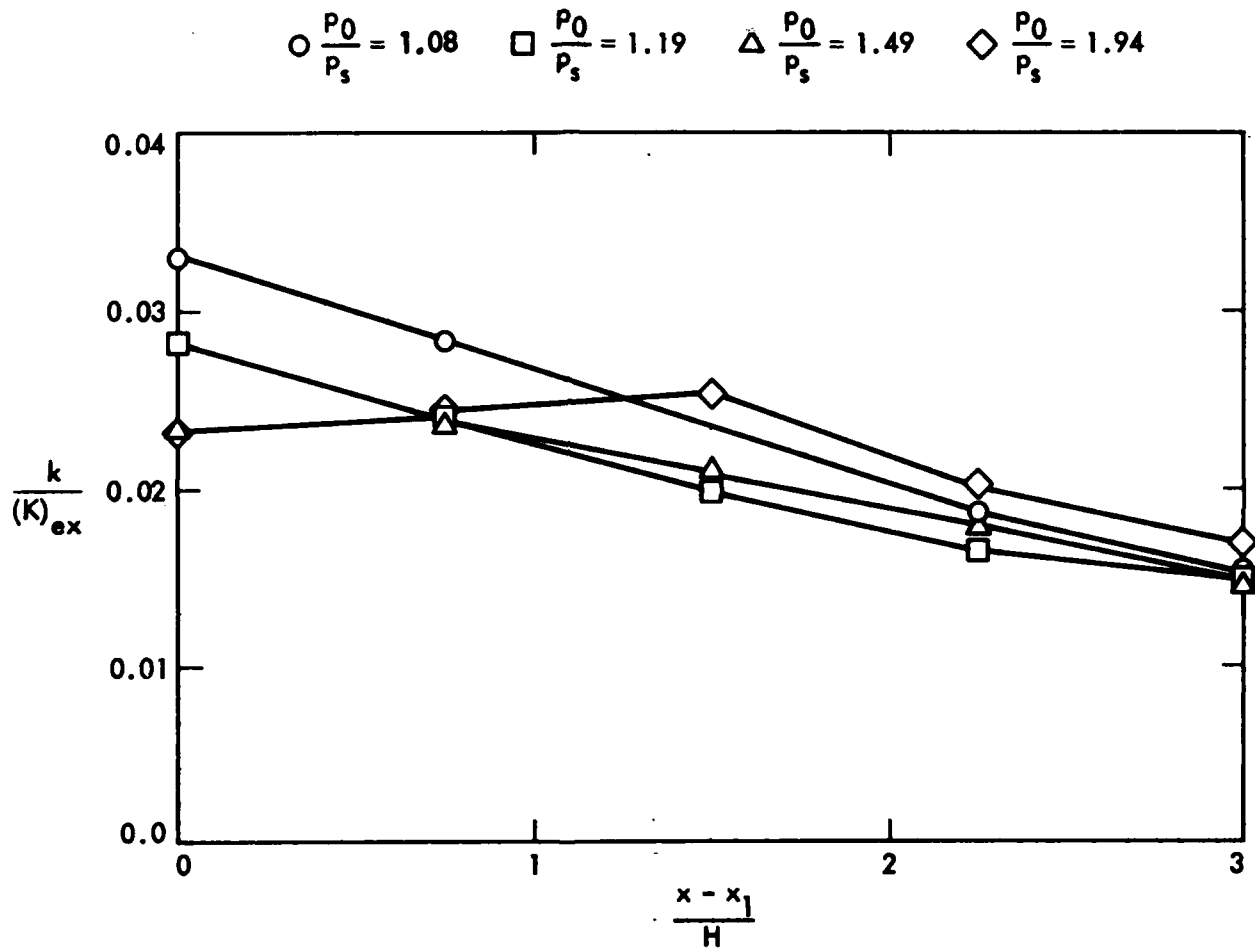


Figure 46. Downstream evolution of the turbulent kinetic energy (two components).  $x_1 = 12.7$  cm (see Figure 16).